Dijet Angular Distributions in $p\bar{p}$ Collisions at $\sqrt{s} = 1.8$ TeV

by

Mary Kathryn Fatyga

Submitted in Partial Fulfillment

of the

Requirements for the Degree

Doctor of Philosophy

Supervised by

Professor Frederick Lobkowicz

Department of Physics and Astronomy

The College

Arts and Sciences

University of Rochester

Rochester, New York

1996

To my mother, for teaching me the value of doing my best
and about the joy of exploring the world.

Curriculum [redacted]

Mary Kathryn Fatyga [redacted]. She attended the University of Illinois in Urbana from 1987 to 1991, and graduated with a Bachelor of Science degree in 1991. She came to the University of Rochester in the Fall of 1991 and began graduate studies in Physics. She received the Master of Arts degree in 1993, and then pursued her research at Fermi National Accelerator Laboratory on the DØ experiment under the direction of Professor Frederick Lobkowicz.

ACKNOWLEDGMENTS

Any analysis done for the DØ experiment is completed with the help of literally hundreds of people who are members of the collaboration. Construction of the DØ detector was completed before I joined the collaboration, and I am grateful for the hard work done by the collaborators before me in order to get the DØ experiment online. My work on this analysis was facilitated by the work of the members of the QCD group, and other members of the collaboration active in the work on the energy scale. I would like to thank all those members of the collaboration that I have had the opportunity to work with as colleagues, and those in particular that I have had the opportunity to call friends.

The Rochester group on DØ is a great resource for any graduate endeavor. I would like to thank my fellow students: Ki Suk, Dylan, Hui, Eunil, and Cathy for their friendship and sympathetic help. I would like to thank the Rochester postdocs of past and present: Dr. Jerry Blazey, Dr. Stefan Gruenendahl, Dr. Jae Yu, and Dr. Marc Paterno for their guidance. I would also like to thank our resident Rochester alumnus, Dr. Bob Hirosky, for easily convincing me to join Rochester, and for being a great mentor and friend. Lastly, I would like to thank the fearless leaders of the Rochester group: Professor Tom Ferbel, and Professor Fred Lobkowicz, my advisor.

This analysis was launched into completion this year due to the persistence of Dr. Nikos Varelas, and the hard work and supervision of Dr. Brad Abbott. Dr. Terry Geld, Dr. Rich Astur, and Kate Frame were all of great assistance at various points during the years of this analysis. My hearty thanks for their assistance.

So many friends have supported me throughout my graduate career, and I would like to thank them all.

My greatest thanks goes to my husband, Dr. Mirek Fatyga. He has been

an enormous resource for me in understanding physics. His support (and gentle prodding) kept me going through the rough years of graduate school. I would not have finished without him.

I thank the staffs at Fermilab and the collaborating institutions for their contributions to the success of this work, and acknowledge support from the Department of Energy and National Science Foundation (U.S.A.), Commissariat à L'Energie Atomique (France), Ministries for Atomic Energy and Science and Technology Policy (Russia), CNPq (Brazil), Departments of Atomic Energy and Science and Education (India), Colciencias (Colombia), CONACyT (Mexico), Ministry of Education and KOSEF (Korea), CONICET and UBACyT (Argentina), and the A.P. Sloan Foundation.

Abstract

We present measurements of dijet angular distributions for events with two or more jets produced in $p\bar{p}$ collisions at the Fermilab Tevatron Collider at $\sqrt{s}$ = 1.8 TeV. The distribution of the scattering angle of a parton in the center-of-mass reflects the dynamics of the interaction of two partons. This distribution was measured for different fixed regions of the dijet invariant mass, in particular: $260 < M_{JJ} < 425$, $475 < M_{JJ} < 635$, $M_{JJ} > 550$, and $M_{JJ} > 635$ GeV/c^2. Because the dijet angular distribution is expected to be relatively insensitive to the parton distribution within a proton, we can measure the properties of parton-parton interactions without being concerned with the inability to calculate quantitative aspects of the substructure of the proton. We find that the next-to-leading-order predictions of perturbative Quantum Chromodynamics (QCD) show good agreement with the observed dijet angular distributions for all four mass ranges.

At dijet invariant masses of greater than $\sim$ 500 GeV/c^2, the dijet angular distribution becomes sensitive to any new contact interactions originating from possible quark compositeness. In order to search for evidence that quarks are not point-like objects, but are rather bound states of more fundamental particles, we compared the predicted angular distribution with that measured in data for the mass range of $M_{JJ} > 550$ GeV/c^2. There was no departure from the expectations of next-to-leading-order perturbative QCD, and we have used that to place a limit on the interaction scale for quark compositeness as $\Lambda_c > 1.8$ TeV.

Contents

List of Tables

List of Figures

Foreword

The DØ experiment is a large collaborative effort, in which more than 450 physicists and students from 48 institutions are currently participating. The University of Rochester group is active in monitoring of liquid-argon purity, in data acquisition and reconstruction efforts, and in analysis of data in the areas of QCD, top-quark physics, and new phenomena. The group is also participating in development and construction projects for a scintillating-fiber tracking chamber to be included in the upgrade of the DØ detector.

I was involved in the monitoring of the liquid-argon purity which consisted of maintenance of the liquid-argon monitoring and data acquisition system, as well as tracking the purity level throughout the 1993-1996 collider run. During the 1993-1996 collider run, I was also an active member of the crew involved in the operation of the data acquisition system. I participated in studies of the trigger efficiencies related to QCD analyses, and I developed an online Level 2 tool used to trigger on the mass of dijet events. My analysis project has involved the measurement of dijet angular distributions.

Chapter 1

Introduction

Quantum Chromodynamics (QCD) is a theory that describes the strong interactions of quarks and gluons, the basic constituents of hadrons and nuclei. Unlike electrons, which are considered to be point-like particles, hadrons are composed of constituents called quarks which are bound together by gluons. The substructure of hadrons was first observed in deep inelastic scattering experiments in the 1970's, in which protons were probed by electrons with large momenta. The composite structure of protons can be described in terms of the parton model, in which the proton is regarded as a composite state of three valence quarks, and a sea of virtual quark-antiquark pairs and gluons. A parton refers to either a quark or a gluon. The parton distribution functions (PDFs) describe the partonic substructure of the proton, and represent the probability of a parton carrying a fraction x of the momentum of the parent proton. The PDFs cannot be calculated from theory, and various parton distribution functions have been extracted from data. Parton-parton interactions with high transverse momentum transfer have been successfully modeled by the theory of QCD.

Protons and antiprotons collide in the Fermilab Tevatron at a center-of-mass

energy of $\sqrt{s} = 1.8$ TeV, with instantaneous luminosities of the order of $10^{30} - 10^{31} cm^{-2} s^{-1}$. At this large center-of-mass energy, occasionally, interactions occur between the parton constituents of these hadrons. Any pair of scattering partons can be viewed in the center-of-mass frame as two partons of the same energy, E. When they scatter, they become transformed into jets of particles of invariant mass $2E$ at some center-of-mass scattering angle θ^*, as shown in Fig. 1.1. A jet is a collimated spray of hadrons, which corresponds to the observable remnant of a scattered parton. The term dijet refers to any pair of jets.

The dijet angular distribution is the distribution of the center-of-mass scattering angle produced by the interaction of two partons. This distribution can be measured for different regions of the dijet invariant mass ($\sqrt{\hat{s}}$). This angular distribution is known to be relatively insensitive to the details of the parton distribution functions, and we can therefore measure certain inherent properties of parton-parton interactions without concern about ambiguities of the parton distribution functions. This is an advantage over other methods of testing the predictions of QCD.

In the theory of QCD, quarks are considered to be point-like particles. Recent measurements of the inclusive cross section for jet production ([1],[2]) have brought to the foreground the question of quark compositeness. 'Quark compositeness' is a shorthand notation for any theory which assumes that quarks are composed of yet smaller point-like particles, sometimes called preons. Quark substructure could be observed as a departure of data from the predictions of QCD. The Fermilab Tevatron provides a large sample of parton-parton interactions with large momentum transfer. At the Tevatron center-of-mass energy, we are able to probe quark compositeness at a scale on the order of 1 TeV. Theories predicting quark compositeness at this scale expect a clear departure from the predictions of QCD at dijet invariant masses of greater than $\sqrt{\hat{s}} \sim 500$ GeV/c^2, and the Fermilab Tevatron is

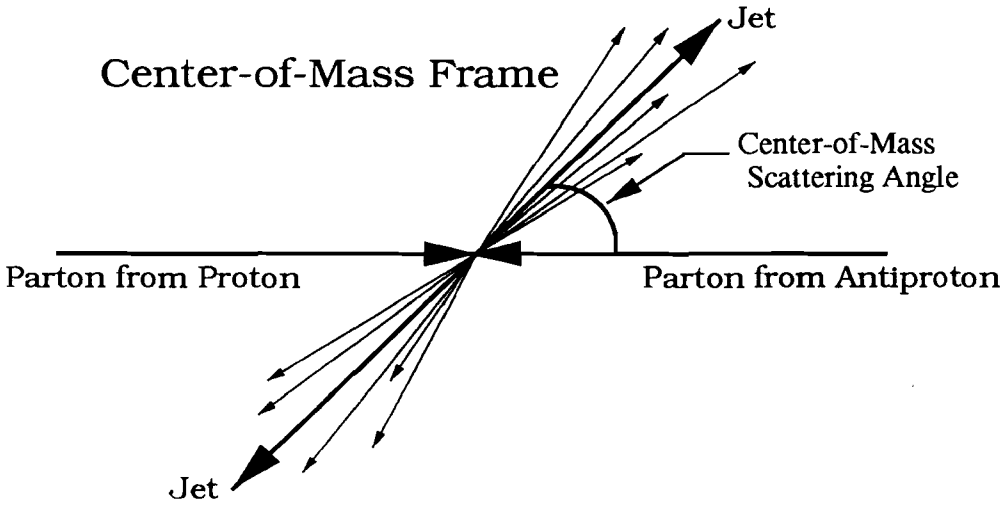

Figure 1.1: At Fermilab, two partons scatter at a center-of-mass scattering angle and create a dijet pair.

an excellent place for probing such mass regions.

The DØ experiment is a collaboration of over 400 scientists from over 40 institutions around the world. The experiment had data runs in 1992-1993, and 1993-1995. This analysis will be based on data from the 1993-1995 collider run. The DØ detector has an excellent calorimeter, with almost 4π angular coverage, and uniform response over a large range of transverse momenta and rapidities. It therefore provides a unique opportunity to study dijet angular distributions.

In this thesis, we study the dijet angular distributions in order to compare the predictions of QCD to the experimental data, and to determine if the data show a departure from QCD that could be attributed to quark compositeness.

Chapter 2

Theory

2.1 The Parton Model

The parton model describes the substructure of a proton as consisting of three valence quarks, and a sea of virtual quark-antiquark pairs and gluons, all bound together in a quantum mechanical state which is a proton. This binding interaction between the three quarks creates an extended volume of energy density. A parton probing the proton with sufficient momentum transfer to resolve the substructure may interact with one of the valence quarks or with the volume of energy density (which would be described as an interaction with a virtual quark, antiquark, or gluon). The substructure of a proton can be visualized as in Fig. 2.1. When a proton collides with an antiproton, three general types of hard interactions can occur: a valence quark from the proton can interact with a valence quark from the antiproton ($q\bar{q}$); an interaction between the volumes of energy density from the proton and the antiproton can produce any one of a variety of interactions between virtual partons ($q\bar{q}$, qq, $\bar{q}\bar{q}$, gq, $g\bar{q}$,gg); or a valence quark from the proton (or the antiproton) can interact with the volume of energy density from the antiproton

(or proton) ($q\bar{q}$, qq, $\bar{q}\bar{q}$, gq, $g\bar{q}$). Most quantitative aspects of the substructure of the proton cannot be calculated directly, but must be measured. A series of parton distribution functions have been extracted from different experiments, and parameterized to describe the substructure of the proton as the probability of encountering a particular constituent (a valence quark, a gluon, or a virtual sea quark) carrying a fraction x of the proton momentum. Shown in Fig. 2.2 is a sketch of PDFs for the valence quarks, gluons, and virtual sea quarks. The parton model and the PDFs describe the initial states that comprise a parton-parton interaction in a proton-antiproton collision. The parton-parton interaction itself is described by the theory of Quantum Chromodynamics.

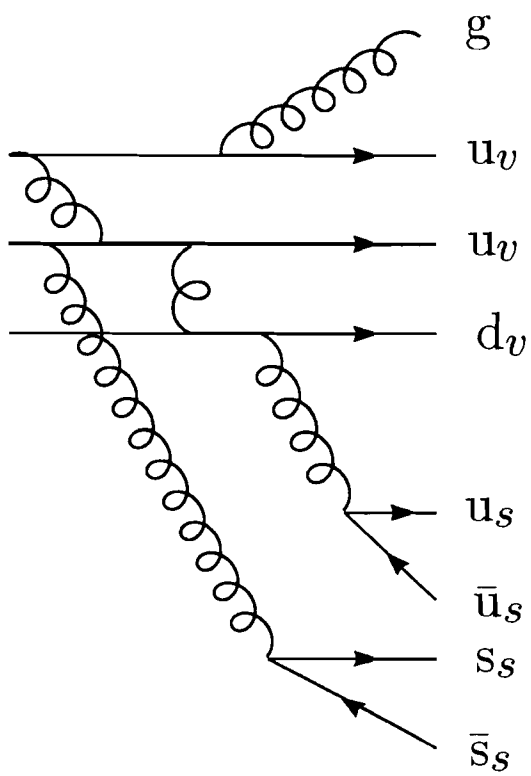

Figure 2.1: The proton is composed of three valence quarks and a sea of virtual gluons and quark-antiquark pairs.

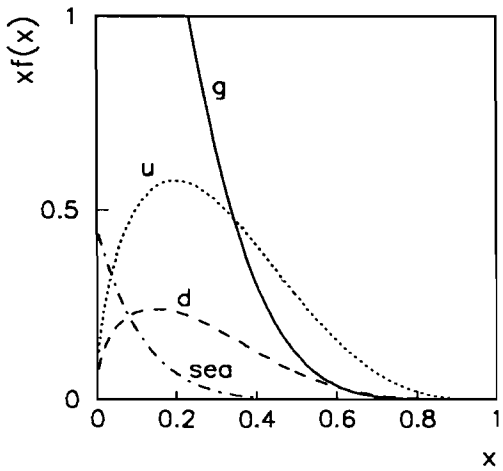

Figure 2.2: Sketch of parton distribution functions for the proton (adapted from [3]).

2.2 Quantum Chromodynamics

The interactions of partons via the strong force are based on the exchange of color, and are mediated by gluons. Color was first postulated to explain an apparent violation of Fermi statistics. The Δ^{++} particle appeared to be composed of three identical fermions, u quarks, in the same quantum mechanical ground state. If so, this would violate the Pauli Principle, and consequently, an additional quantum number, color, was needed in order to distinguish between the ground states of the three u quarks, and to save the quark model of hadrons. It was later determined that color is not just a mathematical construct, but plays a fundamental part in the interactions of partons. Quarks come in three different colors: red, green, and blue (R,G,B). Antiquarks come in three different 'anticolors': cyan, magenta, and yellow, which are effectively antired, antigreen, and antiblue ($\bar{R}$,$\bar{G}$,$\bar{B}$). To enable gluons to exchange the color of two partons, they must come in color-anticolor combinations ($R\bar{G}$, $B\bar{G}$, etc.). Quarks interact through the exchange of a gluon, in a fashion similar to the exchange of photons in Quantum Electrodynamics

(QED). A fundamental difference between QED and QCD is that photons are charge neutral, but gluons have color and can couple to other gluons. This leads to the concepts of asymptotic freedom and confinement. When two partons are very close together in space, the strength of their coupling is very small, and they behave essentially as free particles. This is known as asymptotic freedom. As the distance between two partons grows, the strength of their coupling increases to a point at which it requires less energy to create a quark-antiquark pair out of the vacuum to seal the breach between the two partons than to allow their distance to increase. This leads to confinement. Confinement occurs, because as the distance between any two partons grows, a cloud of virtual gluons and quark-antiquark pairs surrounds the partons and effectively increases the color force between them [4]. The strength of the interaction between two partons is described by the strong coupling constant, α_s.

The fundamental particles of the theory of QCD are the quarks and gluons. The perturbative predictions of the theory that describe the interactions of partons can be calculated using Feynman diagrams [5]. A Feynman diagram representing a quark and an antiquark exchanging a gluon is shown in Fig. 2.3. Feynman di-

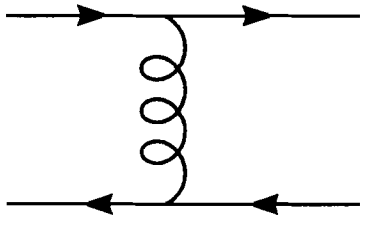

Figure 2.3: A Feynman diagram of a quark and an antiquark exchanging a gluon.

agrams describe parton-parton interactions in terms of a perturbative series in the strong coupling constant, α_s. The order of a given diagram is determined by

the number of vertices, each of which supplies a factor of α_s in the calculation of the cross section. A leading-order (α_s^2) diagram has two vertices. The Feynman diagrams representing a parton-parton interaction at leading-order are shown in Fig. 2.4. A next-to-leading-order (α_s^3) diagram has three vertices. Some of the Feynman diagrams representing a parton-parton interaction at next-to-leading-order are shown in Fig. 2.5. The higher order contributions are due to the fact that any parton has a finite probability for radiating gluons. Scattered partons can radiate any number of gluons, and gluons can split into quark-antiquark pairs, as represented by the Feynman diagram shown in Fig. 2.6. Each of these radiations contributes an additional vertex to a diagram. Due to this radiative property, an infinite series of diagrams must be calculated in order to predict the exact behavior of QCD to all orders. Assuming that the value of α_s is small, the magnitude of each higher-order contribution (α_s^3, α_s^4, etc.) decreases, and one can calculate the predictions of QCD fairly accurately using just the lower-order diagrams. The mathematical difficulty in calculating the predictions of QCD increases dramatically for each additional order. Currently, only the calculations for leading-order (α_s^2) and next-to-leading-order (α_s^3) are available.

Perturbative calculations have been successful for QED because its coupling constant, $\alpha = \frac{1}{137}$, is quite small. Perturbative calculations have been less successful for QCD because its coupling constant is relatively large ($\gtrsim 0.1$), and significant theoretical errors are associated with the exclusion of higher-orders. Fortunately, the coupling between two partons is not a constant, but is a function of the scale of the momentum transfer in the interaction, referred to as a running coupling. As the center-of-mass energy of the interaction increases, the coupling between any two partons decreases and approaches asymptotic freedom. In this region, calculations using perturbative QCD can be made with reasonable accuracy. (It should be recognized that perturbative expansions eventually tend to diverge, and, unless the

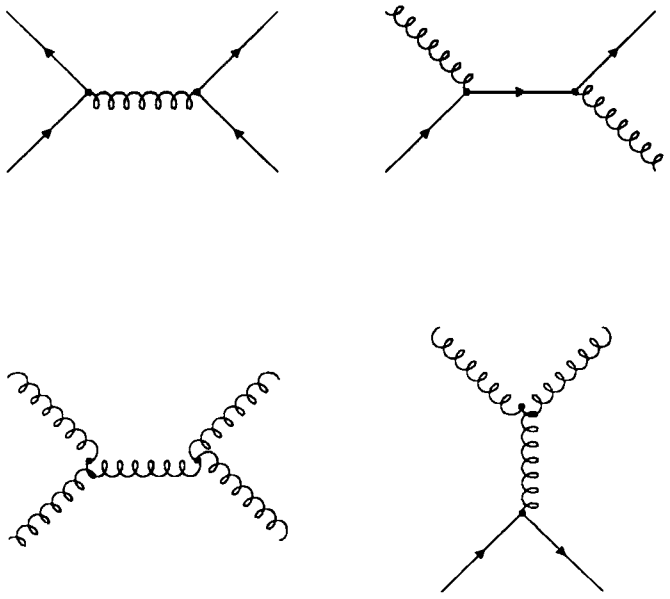

Figure 2.4: Examples of leading-order (α_s^2) Feynman diagrams for jet production.

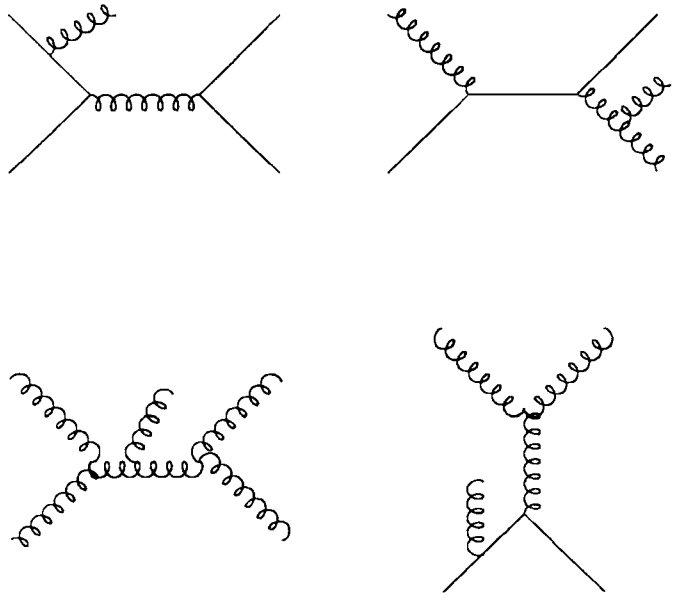

Figure 2.5: Examples of next-to-leading-order (α_s^3) Feynman diagrams for jet production.

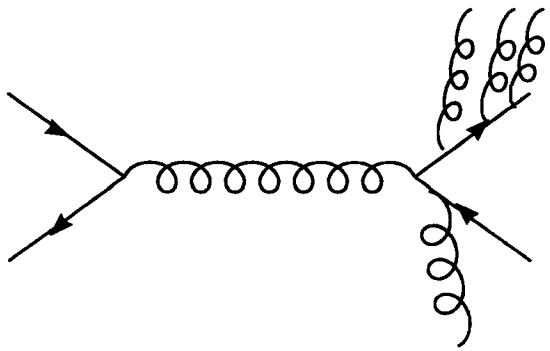

Figure 2.6: An example of a Feynman diagram showing gluon radiation.

coupling is sufficiently small, there is no guarantee of convergence.) The running of α_s does not help in predicting the substructure of the proton, because quarks are bound at energies far below those at which the strong coupling approaches asymptotic freedom. Parton distribution functions can consequently only be determined through experimental means. An additional difficulty in calculating perturbative predictions of QCD is that there are divergences in the theory, primarily due to the fact that the theory treats particles as point-like objects. To avoid this complication, the theory of QCD is renormalized. Renormalization is a mathematical procedure in which the divergences in the theory are made to cancel. This is done by introducing a renormalization scale, μ, which is effectively an energy at which integrals are cutoff in order to avoid divergent regions.

The observables of the theory of QCD are not the quarks and gluons. In fact, neither quarks nor a gluons have been observed experimentally as solitary objects. This is because, according to the theory of QCD, observable objects are colorless, or, more precisely, invariant under rotations in color space. An observed hadron is either an object with each of the three colors (RGB, $\bar{R}\bar{G}\bar{B}$), a baryon, or a color-anticolor pair ($R\bar{R}$, $G\bar{G}$, $B\bar{B}$), a meson. In a proton-antiproton collision,

a parton is emitted from its parent hadron. As the distance between the parton and the remnants of its parent hadron increases, the strong coupling between them increases. Multiple quark-antiquark pairs are produced out of the vacuum to seal the breach between the parton and its parent and to create colorless final state particles. The result is a spray of hadrons formed along the direction of the original scattered parton. This process is known as fragmentation, and the spray of hadrons is the observed remnant of a parton-parton interaction, or what is called a jet. Fragmentation also cannot be calculated from perturbative QCD because once the initial hard interaction occurs, the subsequent interactions caused by fragmentation are at ever lower energy levels, and hence have ever greater couplings. Thus, fragmentation characteristics must be measured and fitted to some phenomenological forms.

In order to overcome the difficulties of calculating cross sections from perturbative QCD, non-perturbative components of the theory are assumed to be separable from the parton-parton subprocess cross section. This is referred to as factorization. For a generic inclusive process of producing C in collisions of A and B, $A + B \rightarrow C + X$, the cross section can be described as follows [6]:

$$\sigma_{A+B\rightarrow C+X} = \sum_{ij} \int dx_1 dx_2 f_i^A(x_1, \mu_F) f_j^B(x_2, \mu_F) \hat{\sigma}_{ij\rightarrow C}(\hat{s}, \mu_F, \mu_R, \alpha_s(\mu_R)) \quad (2.1)$$

$$\hat{s} = x_1 x_2 s \quad (2.2)$$

i and j are indices for any pair of partons contributing to the process. $f_i^A(x, \mu_F)$ is a parton distribution function which represents the probability that a parton of type i carries a fraction x of the momentum of hadron A. $\hat{\sigma}_{ij\rightarrow C}$ is the subprocess cross section for the interaction of partons of types i and j for a center-of-mass energy, s, and factorization and renormalization scales, μ_F and μ_R. μ_F and μ_R

are typically chosen to be equal ($\mu \equiv \mu_F = \mu_R$), and of the order of the energy scale of the parton-parton interaction. The factorization assumption allows one to calculate the cross section for the subprocess in a way that is relatively independent of the uncertainties in the measured parton distribution functions. The final result of any calculation should be, in principle, independent of the choice of the arbitrary renormalization scale, μ. Any dependence on the choice of renormalization scale can be interpreted as a sensitivity of the calculation to higher-order contributions.

2.3 Jet Definition

In order to compare the predictions of perturbative QCD to data, one must be able to relate the kinematic aspects of the original scattered parton to its fragmented remnants, the jet. The aftermath of a parton-parton collision can be examined at three levels. The first level is the parton level, in which the kinematic variables are extracted from the final state quarks and gluons before they fragment. The second level is the particle level, in which the kinematic variables are extracted from the particles that are the result of the fragmentation process. The third level is the calorimeter level, in which the kinematic variables are extracted from the distributions of energy measured in the calorimeter. Of course, data are obtained from the calorimeter, and consequently a method must be devised to compare the kinematic information from the calorimeter to that of the particle or parton level. At the calorimeter level, the energy and position of a jet can be defined as the vector sum of energy clusters within a cone of radius $R_{cone} = \sqrt{\Delta\eta^2 + \Delta\phi^2} = 0.7$. This will be described in detail in Chapter 5. At leading-order, it is simple to extract the energy and position of a single parton. At higher-orders, this becomes increasingly difficult, because additional partons can be radiated in close proximity to the original scattered parton, and not be distinguished at the calorimeter level. Partons

are therefore clustered into a single jet if they are within a distance $R_{sep} \times R_{cone}$ of one another. The value of R_{sep} is set by the experiment, and is usually defined to be between 1.2-1.3, although it is sometimes defined as large as 2.0. Any dependence of the theory on the choice of R_{sep} is considered to be an uncertainty associated with the choice of a particular jet algorithm. At the particle level, partons must be converted into particles by using measured fragmentation functions, and the particles clustered into a cone of radius $R_{cone} = \sqrt{\Delta\eta^2 + \Delta\phi^2} = 0.7$, in a manner similar to that used for the calorimeter.

2.4 Dijet Angular Distributions

The predictions of perturbative QCD have been highly successful in describing the observed distributions for the interactions of partons. In recent years, predictions have improved in accuracy through inclusion of next-to-leading-order corrections. Also, measurements have been extended into regions of greater momentum transfer, providing more sensitive tests of QCD. Dijet angular distributions provide a good method of testing the predictions of perturbative QCD in these regions.

2.4.1 Definition of Variables

The coordinate system of the DØ detector is a right-handed one, in which the $+\hat{z}$ vector is in the direction of the proton beam (pointing South). $+\hat{y}$ points upward and $+\hat{x}$ vector (pointing East) is perpendicular to both the $+\hat{z}$ and $+\hat{y}$ vectors. A spherical coordinate system (r, ϕ, θ) is also used, in which the $\hat{z}$-axis (the axis of the proton beam) is the polar axis. The longitudinal component of a kinematic variable is the component along the direction of the beam axis, and the transverse component of a kinematic variable is the radial component perpendicular to the beam.

The cross section for the dijet angular distribution predicted by leading-order QCD can be written as follows [7]:

$$\frac{d^2\sigma}{dM_{\rm JJ}^2\, d\cos\theta^\star} = \sum_{i,j=q,g} \int_0^1 dx_1\, dx_2\, f_i(x_1,Q^2) f_j(x_2,Q^2) \delta(x_1 x_2 s - M_{JJ}) \frac{d\hat{\sigma}_{ij}}{d\cos\theta^\star} \tag{2.3}$$

The subprocess cross section, $\frac{d\hat{\sigma}_{ij}}{d\cos\theta^\star}$, is given by the following.

$$\frac{d\hat{\sigma}_{ij}}{d\cos\theta^\star} = \sum_{k,l} \frac{1}{32\pi M_{JJ}^2} \overline{\sum} |M(ij \to kl)|^2 \frac{1}{1+\delta_{kl}} \tag{2.4}$$

The factor $\frac{1}{1+\delta_{kl}}$ is introduced to account for the double counting of processes for which the final state partons are identical. The matrix elements are averaged and summed over initial and final state spins and colors.

The angular distribution in $\theta^\star$ is that of the dijet axis calculated relative to $\hat{z}$ in the final state parton-parton rest frame. The shapes of the dijet angular distributions predicted by perturbative QCD will be compared to distributions observed in several regions of the dijet invariant mass, which is defined as:

$$M_{JJ}^2 = 2E_{T1}E_{T2}(\cosh(\eta_1 - \eta_2) - \cos(\phi_1 - \phi_2)) \tag{2.5}$$

This formula assumes that the masses of the individual jets are negligible. E_T is the transverse component of the energy (E) of the jet, that is $E_T = E\sin\theta$. Pseudorapidity η is defined as $\eta = -ln(\tan(\frac{\theta}{2}))$. Pseudorapidity is an approximation of rapidity $y = \frac{1}{2}ln(\frac{E+p_z}{E-p_z})$ for particles whose masses are much smaller than their transverse momentum, that is $m \ll p_T \approx E_T \approx \sqrt{E^2 - p_z^2}$ (p_z is the z component of the momentum). Rapidity is used as a variable because the difference in rapidities is invariant under a Lorentz boost along the $\hat{z}$ axis. Subscript 1 refers to the jet in the event with the largest transverse energy, which will be referred to

as the leading jet. (E_{T1} is the transverse energy of the leading jet, and η_1 is the pseudorapidity of the leading jet, etc.) Subscript 2 refers to the jet in the event with the second largest transverse energy, which will be referred to as the second leading jet. The center-of-mass scattering angle θ^* is related to the center-of-mass pseudorapidity $\eta^* = -ln(\tan\frac{\theta^*}{2})$. The pseudorapidity of the parton-parton center-of-mass can be written as the difference in pseudorapidities of the two leading jets in the laboratory frame ($\bar{p}p$ rest frame):

$$\eta^* = \frac{1}{2}(\eta_1 - \eta_2) \tag{2.6}$$

This can be visualized as in Fig. 2.7, in which two jets scattered back to back at some η^* are boosted in the lab frame to some η_1 and η_2. Another useful variable is the pseudorapidity boost:

$$\eta_{\text{boost}} = \frac{1}{2}(\eta_1 + \eta_2) \tag{2.7}$$

which is the offset in pseudorapidity that translates a pseudorapidity in the lab frame to that in the parton-parton center-of-mass: $\eta_i^* = \eta_i - \eta_{\text{boost}}$.

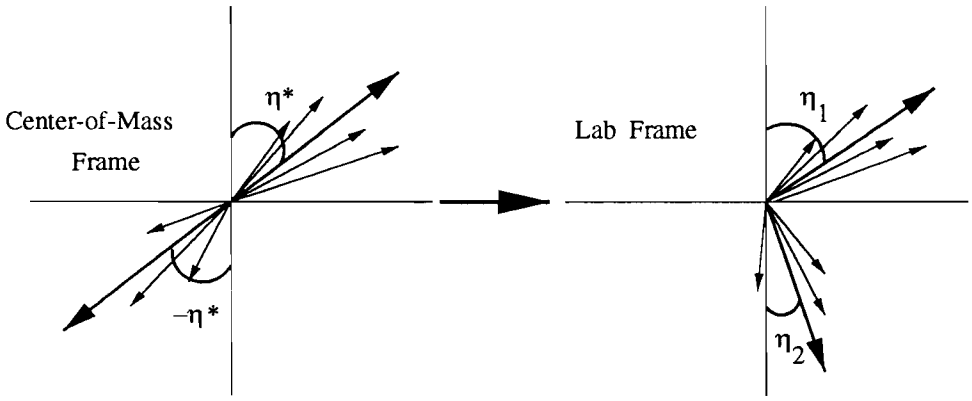

Figure 2.7: Two jets back to back in the center-of-mass frame at some η^* are boosted into the lab frame to some η_1 and η_2.

It is useful to introduce the variable χ, where

$$\chi = \frac{1+\cos\theta^\star}{1-\cos\theta^\star} = e^{|\eta_1-\eta_2|} = e^{2|\eta^\star|} \tag{2.8}$$

Parameterizing the angular distribution as a function of the variable χ facilitates a comparison with theory. For a leading-order parton-parton interaction, as shown in Fig. 2.8, the Mandelstam variables are defined as: $\hat{s} = (p_1 + p_2)^2$, $\hat{t} = (p_1 - p_3)^2$, $\hat{u} = (p_2 - p_3)^2$. $\hat{t}$ and $\hat{u}$ can be written in terms of $\hat{s}$ and $\theta^\star$ as $\hat{t} = -\frac{\hat{s}}{2}(1-\cos\theta^\star)$, and $\hat{u} = -\frac{\hat{s}}{2}(1+\cos\theta^\star)$. χ is consequently equal to $\frac{\hat{u}}{\hat{t}}$. The latter appears in leading-order for each subprocess of the cross section. An example of a subprocess cross section (for $k \neq l$) is shown in the following:

$$\begin{aligned}
\frac{d\hat{\sigma}^{u\bar{d}}}{d\cos\theta^\star} &= \frac{\pi\alpha_s^2}{2M_{jj}^2}\frac{4}{9}\left(\frac{4+(1+\cos\theta^\star)^2}{(1-\cos\theta^\star)^2} + \frac{4+(1-\cos\theta^\star)^2}{(1+\cos\theta^\star)^2}\right) \\
&= \frac{\pi\alpha_s^2}{2M_{jj}^2}\frac{4}{9}\left(\frac{\hat{s}^2+\hat{u}^2}{\hat{t}^2} + \frac{\hat{s}^2+\hat{t}^2}{\hat{u}^2}\right) \\
&\approx \frac{\pi\alpha_s^2}{2M_{jj}^2}\frac{4}{9}\left(2 + 2\chi^2 + \chi + \frac{1}{\chi} + \frac{2}{\chi^2}\right)
\end{aligned} \tag{2.9}$$

for $\hat{s} + \hat{u} + \hat{t} \approx 0$ (ignoring the parton mass).

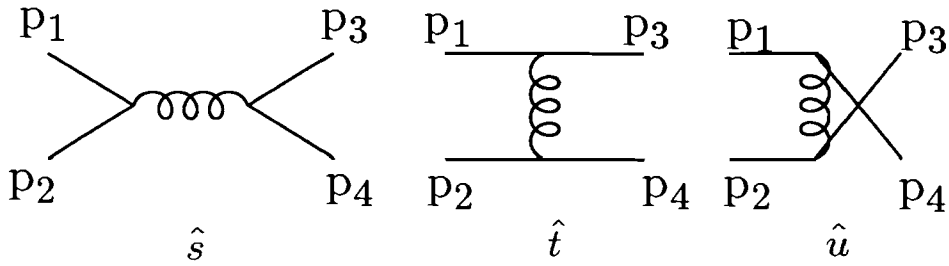

Figure 2.8: The Feynman diagrams that represent the exchanges described by the Mandelstam variables.

2.4.2 Theoretical Motivations

The dijet angular distributions will be measured inclusively. This means that the data sample will contain events with two or more jets. A measurement of two partons scattering into two partons describes QCD processes only at leading-order. When the angular distributions are measured using information from only the two leading jets, the effects of any additional jets can be considered as arising from higher-order effects. The need to keep the measurement inclusive and to consider only the leading two jets is important for experimental, if for no other, reasons. For example, the definition of a jet can be ambiguous because of the presence of radiated partons in close proximity to the original scattered parton. The calorimetry often cannot distinguish the soft partons needed to take proper account of such higher-order contributions. This is primarily because of inefficiencies in detecting partons with small transverse energies.

The different subprocesses ($qg \rightarrow qg$, $q\bar{q} \rightarrow q\bar{q}$, $gg \rightarrow gg$) that contribute to dijet production have similar angular distributions. Shown in Fig. 2.9 are the quark-antiquark and quark-gluon angular distributions normalized to gluon-gluon angular distributions. This is because the angular distributions of all contributing subprocesses tend to be dominated by the exchange of a gluon in the t-channel. The dijet angular distribution is therefore relatively insensitive to the choice of parton distribution functions. Shown in Fig. 2.10 is a comparison of the CTEQ3M and the CTEQ2MS parton distribution functions [8]. The CTEQ2MS PDFs have a higher gluon distribution at small x, and hence a lower gluon distribution at large x than the CTEQ3M PDFs. This insensitivity to a choice of PDFs allows us to examine the properties of the subprocess cross section without limitations from the theoretical error due to uncertainties in the PDFs.

As mentioned above, for small center-of-mass scattering angles, the leading-

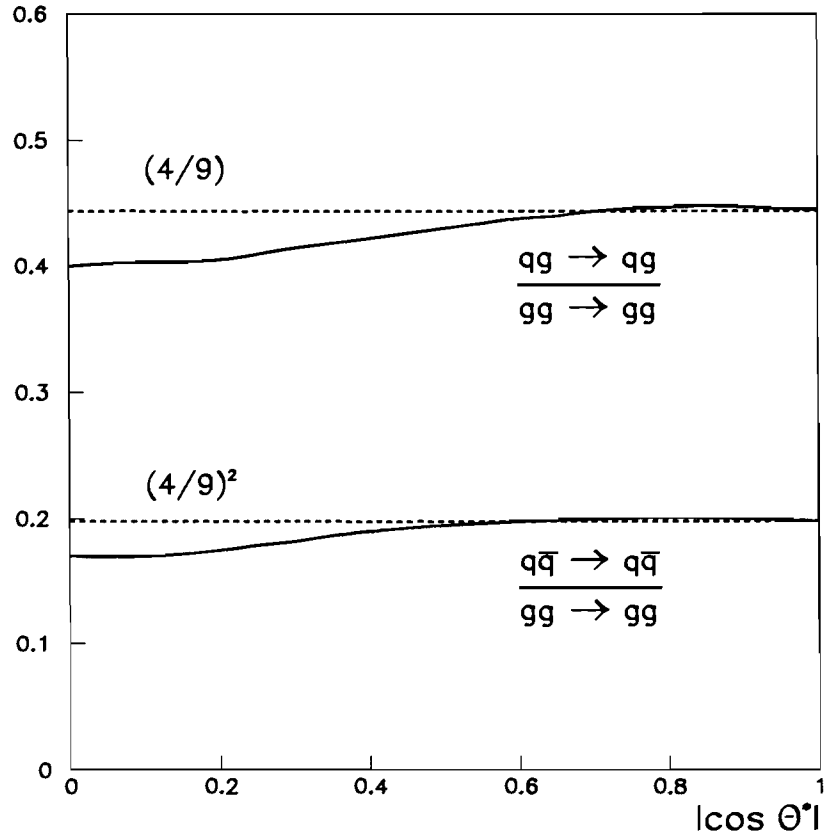

Figure 2.9: Different subprocesses that contribute to jet production produce similar dijet angular distributions. Shown are the quark-antiquark and quark-gluon angular distributions normalized to gluon-gluon angular distributions (adapted from [7]).

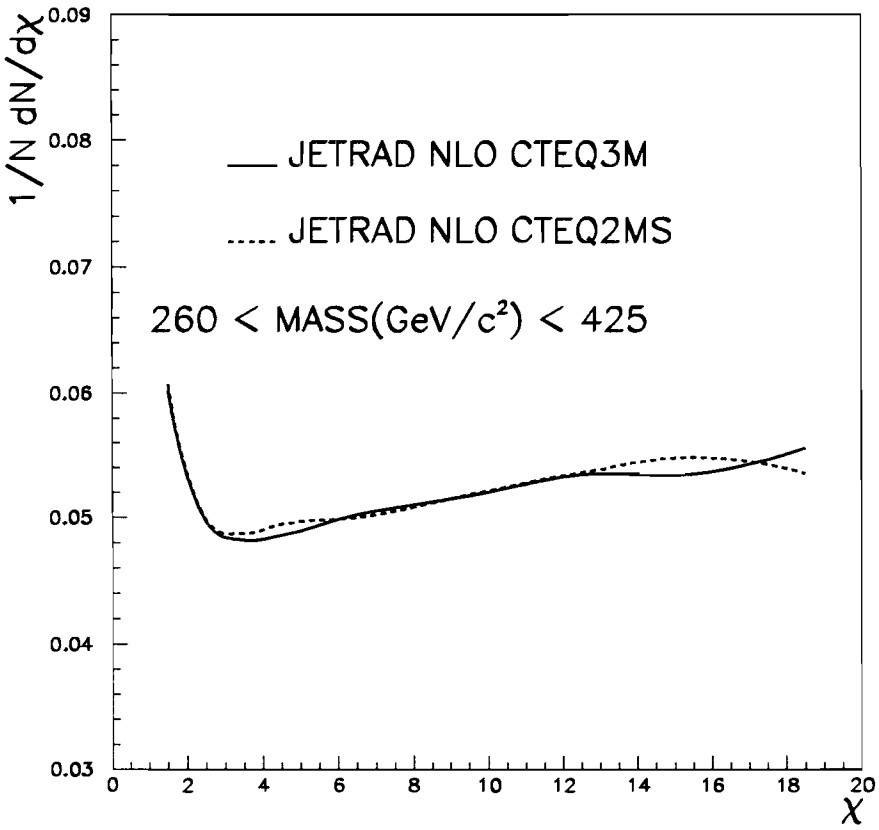

Figure 2.10: The shape of the dijet angular distribution is insensitive to the choice of the parton distribution functions. Shown is a comparison of the CTEQ3M and the CTEQ2MS parton distribution functions for the dijet angular distribution generated at next-to-leading-order with the JETRAD Monte Carlo [9]. The small oscillations are due to statistical uncertainty.

order processes in $\theta^\star$ are dominated by the exchange of a gluon in the t-channel. This exchange of a spin 1 vector boson is analogous to the exchange of a photon in electromagnetism. Thus, for small angles, the dijet angular distribution to first order is proportional to the form from Rutherford scattering:

$$\frac{d\hat{\sigma}_{ij}}{d\cos\theta^\star} \sim \frac{1}{\sin^4(\frac{\theta^\star}{2})} \tag{2.10}$$

As a function of the variable χ, the Rutherford cross section is a constant.

$$\frac{d\hat{\sigma}_{ij}}{d\chi} = \frac{d\hat{\sigma}_{ij}}{d\cos\theta^\star}\frac{d\cos\theta^\star}{d\chi} \tag{2.11}$$

$$\cos\theta^\star = \frac{(\chi-1)}{(\chi+1)} \tag{2.12}$$

$$\frac{d\hat{\sigma}_{ij}}{d\cos\theta^\star} \sim \frac{1}{\sin^4(\frac{\theta^\star}{2})} = \frac{4}{(1-\cos\theta^\star)^2} = (\chi+1)^2 \tag{2.13}$$

$$\frac{d\cos\theta^\star}{d\chi} = \frac{1}{(\chi+1)} - \frac{(\chi-1)}{(\chi+1)^2} \tag{2.14}$$

$$\frac{d\hat{\sigma}_{ij}}{d\chi} \sim (\chi+1)^2\left(\frac{1}{(\chi+1)} - \frac{(\chi-1)}{(\chi+1)^2}\right) = 2 \tag{2.15}$$

The leading-order predictions of QCD are compared in Fig. 2.11 to the Rutherford distribution. As expected, the dijet angular distribution is rather flat for large values of χ (which correspond to small center-of-mass scattering angles). At low values of χ, the distribution begins to rise. This is due to the contributions of s-channel gluon exchange, which is important for large center-of-mass scattering angles.

The distributions measured in this analysis are not absolute cross sections, but

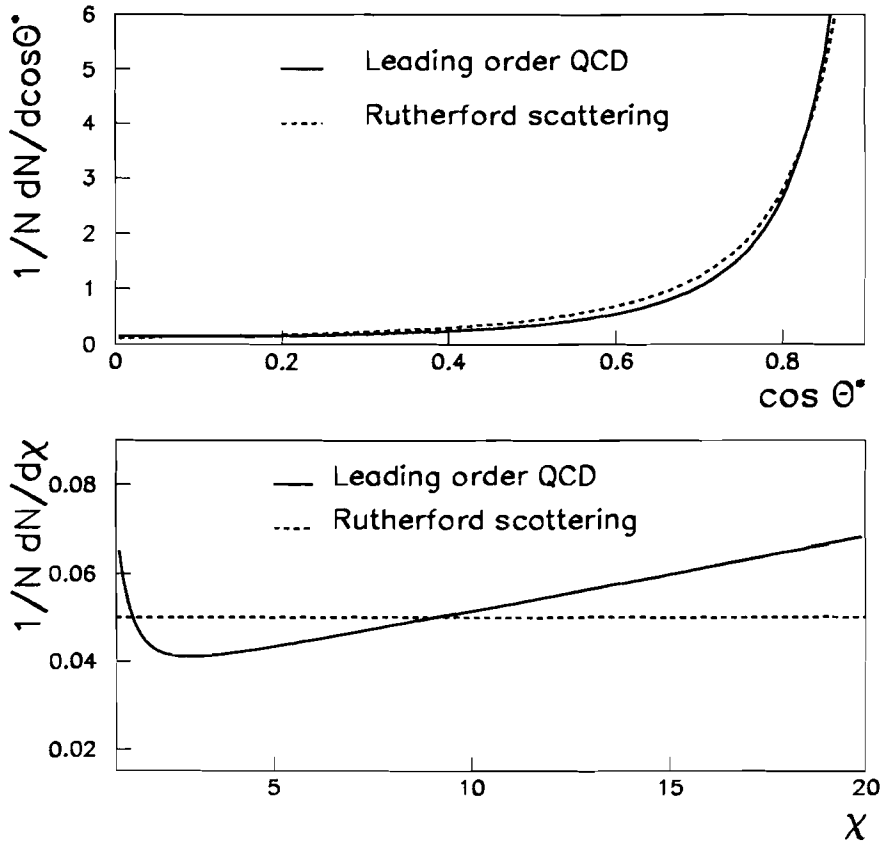

Figure 2.11: A comparison of the angular distribution predicted by leading-order QCD to that of Rutherford scattering. The distribution in $\cos\theta^*$ is normalized in a limited range, $0.0 < \cos\theta^* < 0.9$, in order to avoid the pole at 1.0.

rather normalized distributions:

$$\frac{1}{N}\frac{dN}{dM_{JJ}\,d\chi\,d\eta_{\rm boost}} \tag{2.16}$$

The distributions will be integrated over regions in invariant mass and $\eta_{\rm boost}$ to get a final distribution of $\frac{1}{N}\frac{dN}{d\chi}$ that can be compared to theory. Thus, we compare the shape of the predicted distribution to the data, and ignore the absolute cross section. Unlike the absolute cross section, the shape of the dijet angular distribution is not sensitive to most systematic errors stemming from detector effects.

2.4.3 Theoretical Predictions

Various Monte Carlo computer programs are available for generating the distributions predicted by perturbative QCD. The theoretical predictions used in this analysis are calculated at the parton level with the JETRAD Monte Carlo Event Generator [9]. Unlike analytical calculations, generating the theoretical predictions using Monte Carlo methods for integrating over phase space variables causes an error which is dependent on the number of generated events. Since the predicted angular distributions are generated in this manner they will not appear smooth unless enough events were generated to make this statistical error negligible. Due to the limitations of available computing power, we were unable to generate enough events to remove the statistical errors in all of the next-to-leading-order distributions.

The theoretical predictions can be changed through various input parameters in the JETRAD program. The uncertainty due to the choice of jet algorithm for comparing predictions at the parton level to the jet distributions is minimized by choosing an R_{sep} of 1.2-1.3 [10]. Recall that two partons are clustered into a single jet if they are within a distance $R_{sep} \times R_{cone}$ of one another. This analysis uses

$R_{sep} = 1.2$. The difference between using 1.2 and 1.3 was found to be negligible. The uncertainty due to the choice of parton distribution functions is negligible due to the intrinsic properties of the dijet angular distribution. The parton distribution functions used in this analysis were the CTEQ3M and CTEQ2MS functions [8]. The choice of the renormalization scale has a small effect at leading-order, as shown in Fig. 2.12, but becomes significant at next-to-leading-order. The renormalization scales chosen for this analysis are the E_T of the leading jet, and, for comparison, the $\frac{E_T}{2}$ of the leading jet. As shown in Fig. 2.13, there is a dependence of the normalized shape of the angular distribution on the order of a few percent. The angular distribution is most affected by the dependence of the coupling constant $\alpha_s(\mu)$ on the renormalization scale. At leading-order, the shape of the dijet angular distribution is dominated by the kinematics associated with the exchange of a gluon. At next-to-leading-order, the scattered partons are allowed to radiate gluons, and this radiation brings in an additional dependence of the distribution on the coupling constant, and hence the choice of renormalization scale. This dependence of the theoretical predictions of the dijet angular distributions on the choice of renormalization scale can be interpreted as the theoretical uncertainty associated with higher-order terms.

2.4.4 Compositeness

There is speculation that quarks may not be point-like objects but rather bound states of more fundamental particles. Although there are many theories of quark compositeness, no single model appears to be more promising than any other. The interactions of quark constituents, or preons, are characterized by an energy scale Λ_c which defines the energies below which the strength of the interaction between preons becomes strong enough to bind them into states observed as quarks. Λ_c also

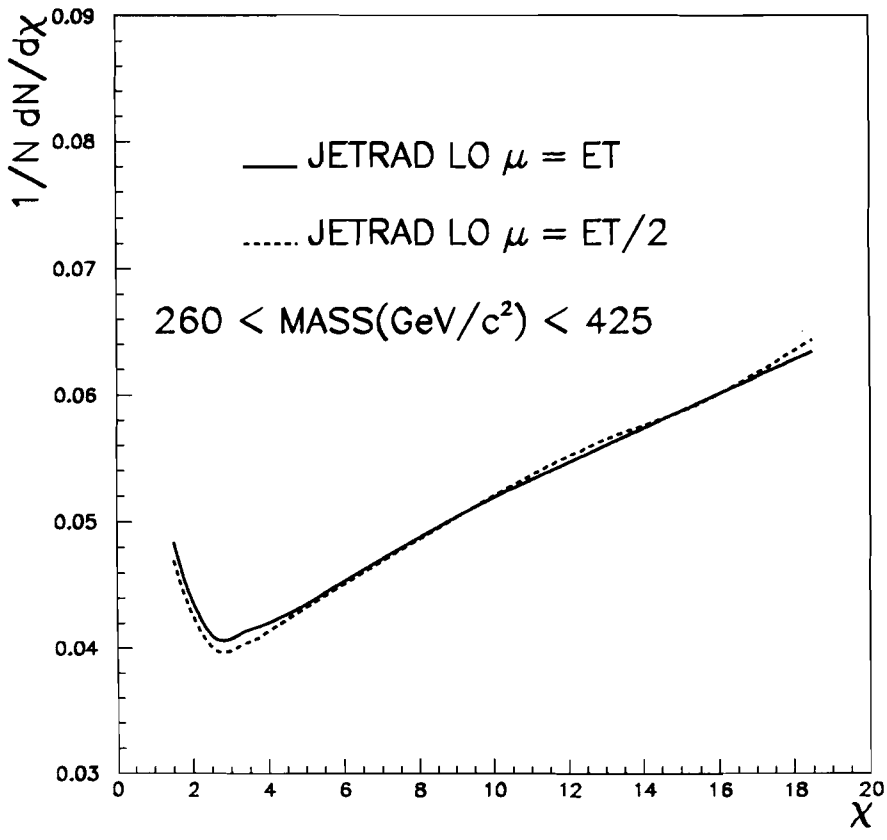

Figure 2.12: At leading-order, the shape of the dijet angular distribution is insensitive to the choice of the renormalization scale. Shown is a comparison for $\mu = E_T$ of the leading jet and $\mu = \frac{E_T}{2}$ of the leading jet for the dijet angular distribution generated at leading-order with JETRAD. Small oscillations are due to statistical uncertainty.

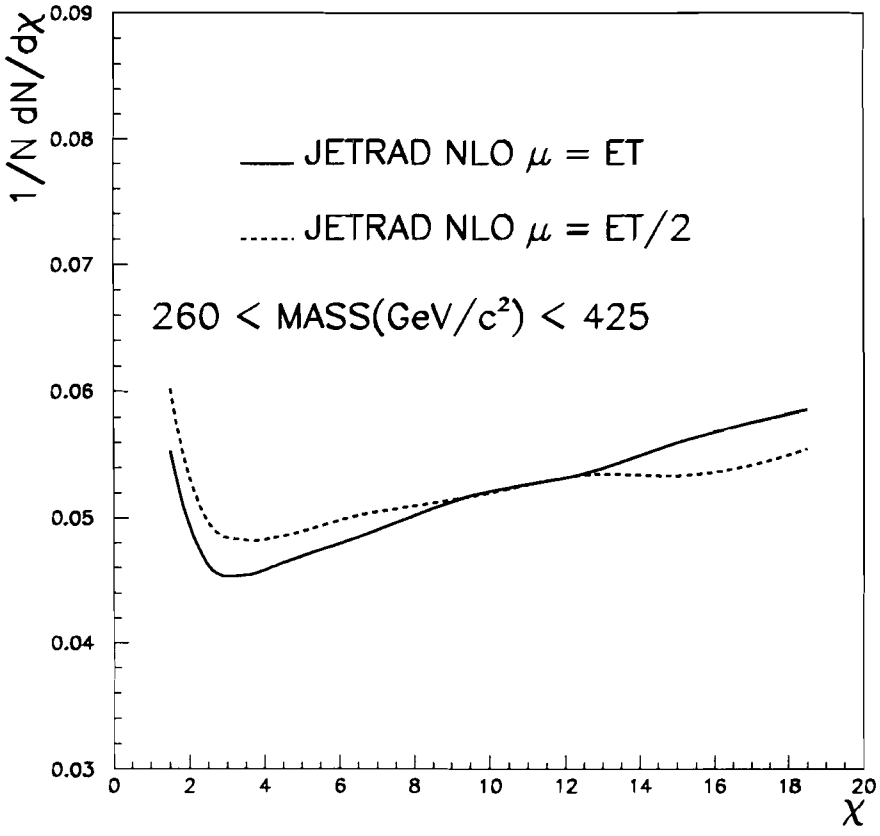

Figure 2.13: At next-to-leading-order, the shape of the dijet angular distribution is sensitive to the choice of the renormalization scale. Shown is a comparison of the $\mu = E_T$ of the leading jet and $\mu = \frac{E_T}{2}$ of the leading jet for the dijet angular distribution generated at next-to-leading-order with JETRAD. Small oscillations are due to statistical uncertainty.

determines the scale at which parton-parton interactions become sensitive to any interactions between the new constituents. In order to search for evidence of quark compositeness, one must search for deviations from the predicted behavior of the parton-parton interactions of QCD. Any such discrepancies could be found by comparing the dijet angular distributions predicted by QCD to data in regions which would be sensitive to quark compositeness. At dijet invariant masses of greater than $\sim$ 500 GeV/c^2, the dijet angular distribution is sensitive to the interactions of preons for $\Lambda_c \approx 1.0$ TeV.

The theory of quark compositeness which we compare to the data describes a four-fermion contact interaction that assumes all quarks to be composite. The interactions between preons are taken to be flavor diagonal. Interactions of quark constituents do not cause changes in flavor, and there are no interactions among quark generations. For example, two up quarks may interact to form two up quarks; a charm quark and a strange quark may interact to form a charm quark and a strange quark; but there are no terms such as an up quark and a charm quark interacting to form an up quark and a charm quark. These flavor-diagonal contact interactions can be described by the following term in the Lagrangian [11].

$$L_{qq} = (\frac{g^2}{2\Lambda^2})(\eta_{LL}\bar{q}_L\gamma_\mu q_L\bar{q}_L\gamma^\mu q_L + \eta_{RR}\bar{q}_R\gamma_\mu q_R\bar{q}_R\gamma^\mu q_R + \eta_{LR}\bar{q}_L\gamma_\mu q_L\bar{q}_R\gamma^\mu q_R) \quad (2.17)$$

Where η_{LL}, η_{RR}, and η_{LR} can be -1 or $+1$, but for the theory which was compared to the data in this analysis, η_{LL}, η_{RR}, and η_{LR} were equal to $+1$, which corresponds to a destructive interference term. g is the effective strong coupling constant. These contributions lead to an additional isotropic term in the angular distribution, which would produce an increase in the number of events at small values of χ (large θ^*).

The predictions of next-to-leading-order QCD with an added term for quark compositeness are not yet available. The leading-order predictions of QCD with an

added contact term for quark compositeness were generated using the Papageno Partonic Monte Carlo Program [12]. Next-to-leading-order predictions with an added term for quark compositeness were estimated by dividing the leading-order angular distribution with an added contact term of Λ_c by the leading-order angular distribution without a contact term, and then multiplying the next-to-leading-order angular distributions generated with JETRAD by this correction factor. The contributions of quark compositeness are shown in Fig. 2.14.

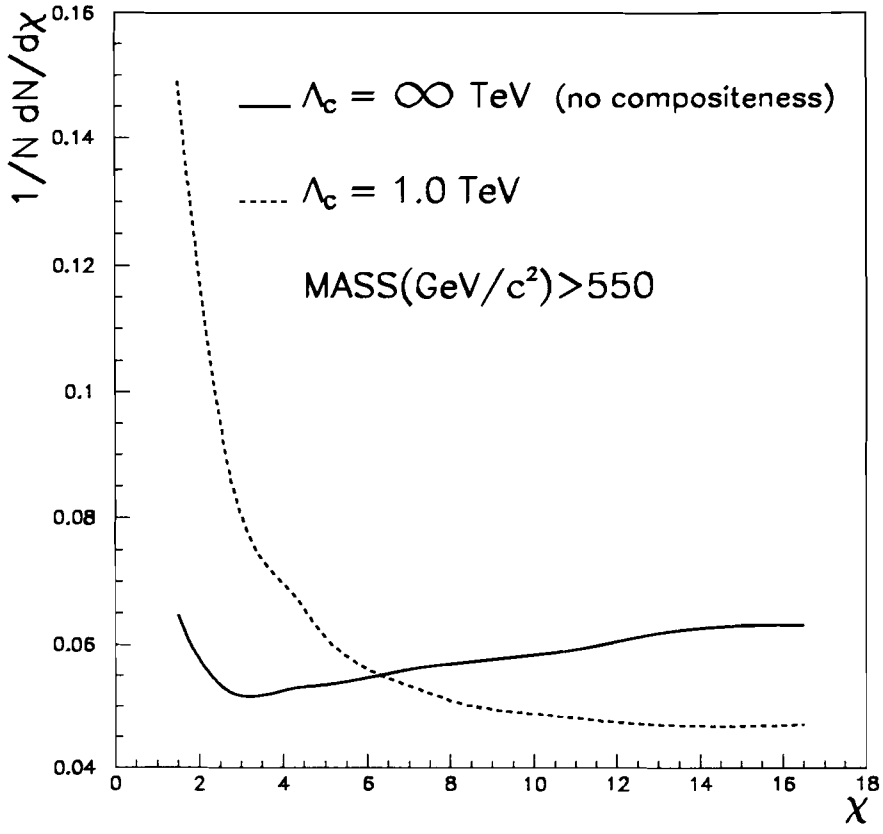

Figure 2.14: The effect of a contact term for quark compositeness on the shape of the angular distribution is shown for masses greater than 550 GeV/c^2.

Chapter 3

The DØ Detector

The DØ Detector, shown in Fig. 3.1, has been designed to study proton-antiproton collisions at the Tevatron at a center-of-mass energy of $\sqrt{s} = 1.8$ TeV. The detector is comprised of three main systems: the central detector, the calorimeter, and the muon systems. These systems were designed to identify and measure electrons, photons, jets, muons, and missing transverse energy - which can signify a neutrino. This chapter will give a brief overview of the components of the detector. A more complete description of the detector is available in [13].

3.1 The Central Detector

The central detector, shown in Fig. 3.2, is comprised of three separate systems: the vertex drift chamber, the transition radiation detector, and the central and forward drift chambers. Since the DØ detector does not have a central magnetic field, the primary purpose of the central detector is the identification of charged particles, mainly electrons, and the reduction of backgrounds produced by particles which can mimic desired signatures. The vertex drift chamber is located just outside of

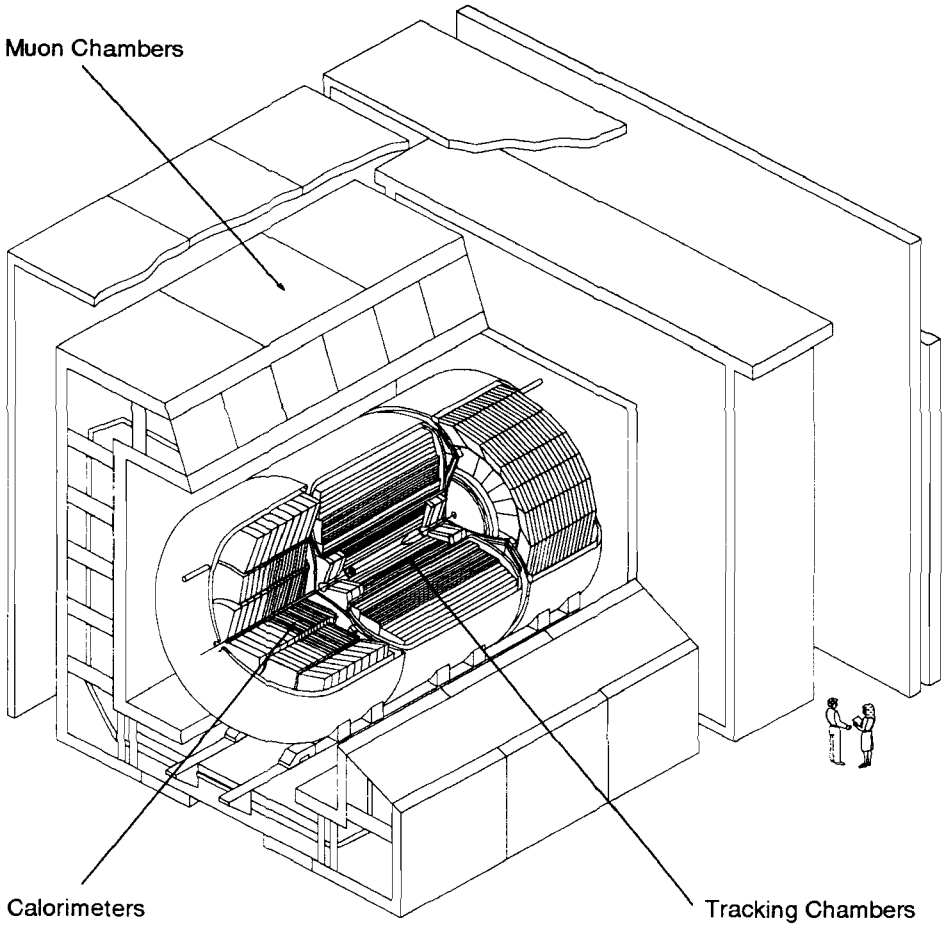

Figure 3.1: The DØ detector is comprised of the central tracking, the calorimeter, and the muon systems.

the Tevatron beam pipe and contains three concentric layers of drift chambers. It is used to determine the longitudinal position of the interaction vertex. Next, the transition radiation detector is located outside of the vertex chamber. Its primary function is to distinguish between electrons and charged pions - which can conspire to produce fake electron signals. It utilizes the fact that highly relativistic charged particles will radiate X-rays when passing through the boundary between two media with different dielectric constants. The energy of the radiated X-rays is dependent on the mass of the charged particle, and this energy can be used to distinguish between an electron and a pion. Finally, the central drift chamber is located outside of the transition radiation detector. It contains four concentric rings of cells and provides tracking coverage for particles scattered at large angles. The forward drift chambers are located perpendicular to the central drift chamber, and to the sides of the interaction region. They provide tracking coverage down to $\theta \approx 5°$.

3.2 The Calorimeter

The detector of primary importance to this analysis is the calorimeter. The dominant function of the calorimeter is to measure the energy of incident particles - charged and neutral. The DØ calorimeter is a 'sampling' calorimeter, which consists of alternating layers of a dense absorber and an active readout medium. The absorber layers in the DØ calorimeter are made of depleted uranium (Ur). Incident particles interact in the absorber, and produce showers of secondary particles. The active layers of the DØ calorimeter are built as ionization chambers with liquid Argon (LAr) as the active medium. When charged particles pass through the LAr, they ionize the liquid along their path. The summed charge collected in the active medium is a measure of the energy of the incident particle, and is proportional

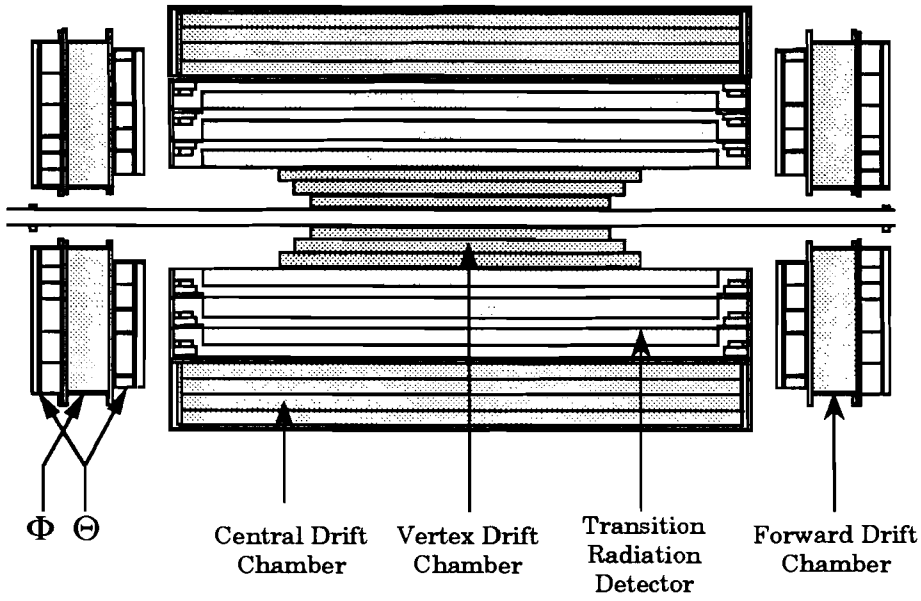

Figure 3.2: The central detector is comprised of the vertex drift chamber, the transition radiation detector, and the central and forward drift chambers.

to the absolute energy of the incident particle. This proportionality is determined from experimental calibration.

The DØ calorimeter, shown in Fig. 3.3, was built in three units: the central calorimeter (CC), and two end-cap calorimeters (EC's). Each calorimeter was built with three main layers. The first layer, the electromagnetic layer, was optimized to measure particles which interact electromagnetically - primarily electrons, photons, and the electromagnetic components of jets. The other two layers are the fine hadronic and the coarse hadronic layers. These two layers were optimized to measure the hadronic components of jets. The coarse hadronic layer uses copper as an absorber, and is used to measure any remaining energy in a shower while containing the energy of the shower within the calorimeter. In the electromagnetic and fine hadronic sections of the calorimeter, depleted uranium was chosen as the absorber in order to increase the uniformity of the response to electromagnetic and

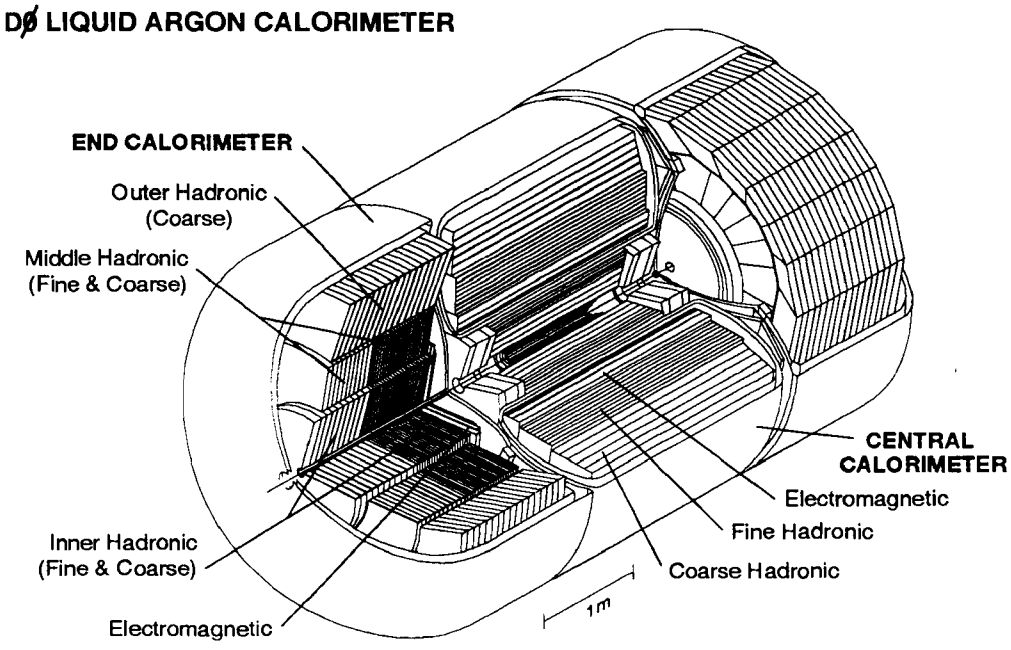

Figure 3.3: The DØ calorimeter is comprised of the central and end cap calorimeters.

hadronic particles. A properly chosen combination of LAr and Ur approximately equalizes the response of the calorimeter to electromagnetic and hadronic showers ($e/\pi \approx 1.0$) and allows for a compact calorimeter with very good resolution and uniformity. The CC covers a pseudorapidity range of $|\eta| < 1.2$. The EC fully covers a pseudorapidity range of $1.4 < |\eta| < 4.1$, and provides reduced coverage for $4.1 < |\eta| < 4.5$. Thus, the DØ calorimeter is able to measure electrons, photons, and jets to large pseudorapidities. Due to its hermiticity, the calorimeter is also able to measure well an imbalance in transverse energy, thus providing a signature of a neutrino.

The active readout layers of the DØ calorimeter are finely segmented in the transverse (η, ϕ) direction. Each segment is separately read out, essentially acting as an independent ionization chamber. These segments are further arranged into 'pseudo-projective' towers, as shown in Fig. 3.4. Each tower is comprised of layers

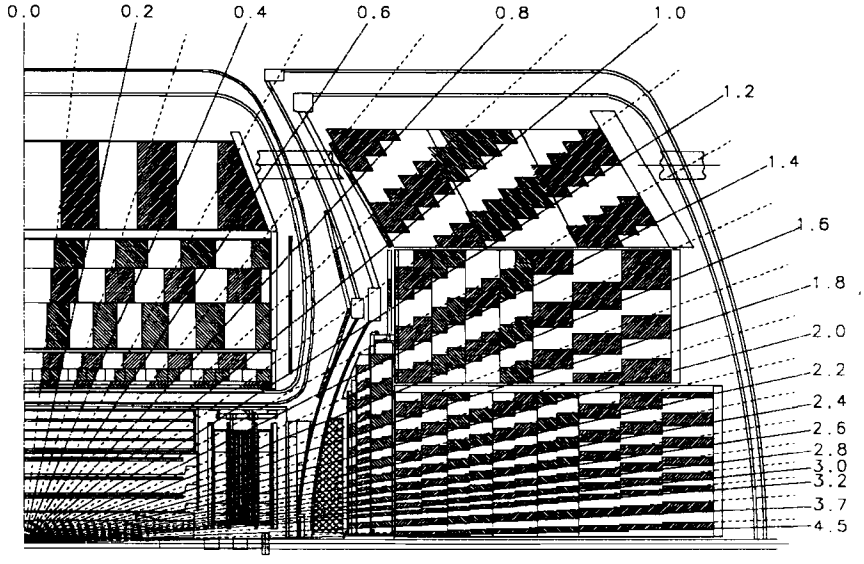

Figure 3.4: The DØ calorimeter is finely segmented in η, ϕ and these segments are arranged into pseudo-projective towers.

of cells whose centers lie along rays projected from the center of the detector (the nominal vertex). They are pseudo-projective because the boundaries of each cell do not project towards the vertex, but are aligned perpendicularly to the absorber plates. The size of a tower in $\Delta\eta \times \Delta\phi$ space is 0.1×0.1. A readout board is composed of a copper pad sandwiched between plates of G10, and covered with a resistive epoxy coating. A unit cell is shown in Fig. 3.5. The absorber plates are kept at ground, and the readout boards are kept at a voltage of approximately $+2kV$. Charged particles traverse the LAr gap, ionizing the liquid. The liberated electrons then drift to the positive potential of the readout board, and are measured as a pulse on the board. This pulse is then amplified and converted to digital counts.

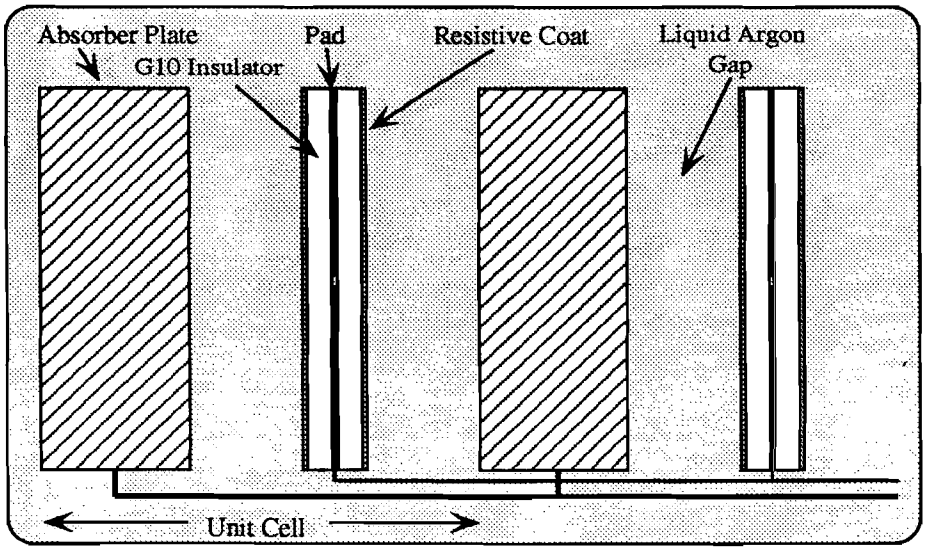

Figure 3.5: A DØ calorimeter unit readout cell.

The Fermilab Main Ring runs through the coarse hadronic section of the calorimeter. This is not a concern for measuring the energy of jets, since relatively little of the jet energy is deposited in the coarse hadronic layer. The main effect is that interactions of beam halo with the beam pipe cause depositions of energy in the calorimeter not related to $p\bar{p}$ interactions. To avoid this problem, events occurring during main ring activity are ignored.

Due to the necessity of having three cryostats, there is a region in pseudorapidity which is not fully covered by the calorimeter ($0.8 < |\eta| < 1.4$), the inter-cryostat region (ICR) (refer to Fig. 3.4). This region is instrumented with two detectors in order to detect particles which escape into the cryostat gap. The first is the inter-cryostat detector (ICD). The ICD is composed of two scintillation counter arrays. Each array consists of a set of scintillator tiles which are of the same size in $\Delta\eta \times \Delta\phi$ space as the calorimeter cells ($\Delta\eta \times \Delta\phi = 0.1 \times 0.1$). The other detector

is the massless gap detector, which is a set of LAr cells ($\Delta\eta \times \Delta\phi = 0.1 \times 0.1$) mounted on the inside wall of the CC and EC cryostats.

3.3 The Muon Detector

The muon detector is used to detect the trajectories of muons, and to measure their momenta. The muon detector is comprised of three layers of proportional drift tube chambers and a system of iron toroidal magnets. The muon system is located outside of the calorimeter, which, for the most part, shields the system from particles other than muons. The first layer of muon chambers is located within the toroidal magnets, and the final two layers are located outside the toroidal magnets. The momentum of a muon is measured by the bend angle of the muon track in the magnetic field, as determined from track hits in the muon chambers.

Chapter 4

Data Selection

Proton-antiproton interactions occur in the Fermilab Tevatron with a frequency of approximately 10^5 interactions per second. The DØ data acquisition system is capable of recording approximately three interactions per second. The DØ experiment uses a system of selection criteria, a trigger system, in order to select those events which are of interest. Interactions of interest are primarily those with large transverse momenta, signifying a hard, inelastic collision. This chapter discusses the DØ trigger system, the on-line trigger requirements placed on the data selected for this analysis, and the efficiencies of the trigger requirements.

4.1 The DØ Trigger System

The interactions of interest to this analysis are parton-parton interactions which produce jets. In order to select, or 'trigger' on, jet events, DØ uses information from the calorimeter. The signature of a hard interaction producing a jet is a cluster of energy deposited in the calorimeter with a large transverse component, or large E_T. The DØ trigger system works in three tiers: Level 0, Level 1, and

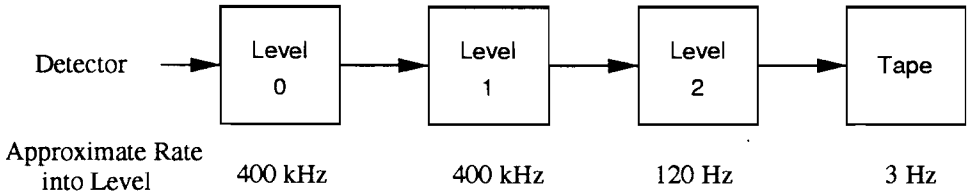

Figure 4.1: The DØ trigger system works in three tiers: Level 0, Level 1, and Level 2.

Level 2, as shown in Figure 4.1. This section will describe the components of the DØ trigger system relevant to the calorimeter and the detection of jets. The overall DØ data acquisition system is described in detail in [13], and [14].

4.1.1 Level 0

Level 0 was designed to trigger when an inelastic collision occurs. Level 0 is comprised of a set of hodoscopes of scintillation counters. These hodoscopes are mounted on each of the end-cap cryostats, and have partial coverage in a pseudorapidity range of $1.9 < |\eta| < 4.3$, and nearly full coverage in the pseudorapidity range of $2.3 < |\eta| < 3.9$. This rapidity coverage gives Level 0 an efficiency of $\geq 99\%$ in triggering on inelastic collisions. Level 0 can also be used to determine the vertex of the interaction by using the timing differences in the triggering of the two Level 0 detectors. When Level 0 triggers on an inelastic collision, it activates Level 1.

The Tevatron does not specifically collide individual protons with individual antiprotons, but bunches of protons circling counterclockwise encounter bunches of antiprotons circling clockwise. These two bunches are collimated at the interaction point in order to facilitate collisions. Because of this, the number of interactions is not restricted to one. Level 0 is used to discriminate against multiple interactions through measuring the rms deviation of the time difference in the triggering of the two Level 0 detectors.

4.1.2 Level 1

In the Tevatron, proton-antiproton beam crossings occur in 3.5 μs intervals. In order to reject, within this time interval, events which are of no interest, Level 1 is comprised of a fast hardware trigger system. For jet triggers, it places a requirement on the magnitude of the transverse component of energy deposited in fixed clusters of calorimeter cells. The E_T is calculated based on the vertex found by Level 0. These clusters are of one of two forms. The first is a trigger tower, which is a cluster of four calorimeter cells defining a radial tower in η, ϕ space of $\Delta\eta \times \Delta\phi = 0.2 \times 0.2$. The second form is a large tile, which is a cluster of calorimeter cells forming a radial tower in η, ϕ space of $\Delta\eta \times \Delta\phi = 0.8 \times 1.6$.

The Level 1 trigger system is a set of logically connected requirements placed by the experimenter. In the case of the calorimeter, it is a set of requirements on the number of trigger clusters (large tiles, or trigger towers) which contain a deposit of E_T above a threshold. For an inclusive (1 or more jets) jet data sample, the Level 1 trigger required one large tile above a desired threshold. The threshold was chosen so that the trigger is efficient for jets in a particular E_T range. When an event fulfills the Level 1 requirements, the trigger framework sends the Level 1 and detector information to be processed in Level 2. The trigger information sent to Level 2 is the η and ϕ coordinates of all clusters which fulfilled a Level 1 threshold requirement. For trigger towers, this is the center of the trigger tower location. For large tiles, this coordinate is the η, ϕ position of the E_T weighted center of the large tile. For jet triggers, a redundant requirement is placed in the Level 1 trigger solely for use in Level 2, which includes an additional lower threshold requirement. All large tiles which pass this threshold requirement are used as 'seeds' or starting η, ϕ coordinates for the Level 2 jet algorithm.

4.1.3 Level 2

Level 2 is a software filter in which events are sent to one of 50 Vax Workstations running in parallel. Each Vax Workstation executes a set of software tools used to place physics selection requirements on the incoming events from Level 1. The parallel processing in Level 2 allows for an average of 200 ms of processing time for each event. For jet triggers, the software tool utilized is a rudimentary jet algorithm which finds and calculates the E_T of the jets in an event. The algorithm uses each of the seeds in the list from Level 1 as the center of a jet and sums all the E_T within a $R = \sqrt{\Delta\eta^2 + \Delta\phi^2} = 0.7$ cone. Level 2 places a requirement on the number of jets with an E_T above a given threshold. When an event fulfills the requirements placed in Level 2, it is recorded on tape.

4.2 Trigger Requirements

The data of interest to this analysis are the events with two or more jets with dijet invariant masses of greater than approximately 250 GeV/c^2. In order to increase the efficiency of selecting events with two or more jets, the triggers used in this analysis are the set of triggers which require one jet with an E_T above a given threshold. In order to select events with dijet invariant masses of greater than 250 GeV/c^2, the triggers used were three of the triggers with the highest E_T thresholds, as summarized in Table 4.1.

Table 4.1: Level 1 and Level 2 requirements placed on data sample.

Trigger	Level 1	Level 2
JET 30	1 tile $>$ 15 GeV	1 jet with E_T $>$ 30 GeV
JET 85	1 tile $>$ 35 GeV	1 jet with E_T $>$ 85 GeV
JET MAX	1 tile $>$ 35 GeV	1 jet with E_T $>$ 115 GeV

4.3 Trigger Efficiencies

There are essentially two pathways through which information is collected from the calorimeter: a complete readout of all components of the calorimeter, which is the event information stored on tape; and a subset of this information, which is used by the trigger system. The DØ trigger system is unable to use the full information available from the calorimeter because of the need to reject events in a very short time interval. The rudimentary jet information used by the trigger system causes some inefficiencies in selecting events with jets in certain E_T and η ranges. Three primary components of the calorimeter trigger cause inefficiencies in selecting jet events: the fixed locations of the calorimeter tiles, reduced instrumentation of the gap between the cryostats, and the reduced integration time of the calorimeter readout.

- **Inefficiency due to the fixed tile locations:** In order to quickly identify an object in the calorimeter as a jet, the towers of the calorimeter are clustered into large tiles at fixed, pre-determined locations. The efficiency of the Level 1 trigger as a function of E_T is related to the probability of a jet depositing the required amount of E_T within a single tile to fulfill the trigger requirements. If a jet, which is about the size of a Level 1 large tile, is not centered within one tile, but overlaps with an adjacent tile, its deposited energy will be split between the two tiles. Such a jet will have a reduced probability of fulfilling the Level 1 requirements. The only jet energy 'seen' by Level 2 is that which is within a 0.7 radius of the E_T weighted center of the large tile which triggered in Level 1. The rudimentary jet algorithm used in Level 2 does not optimize the location of the center of a jet, and may not envelop the majority of the jet's energy within the cone. This will reduce the probability of a jet fulfilling the Level 2 requirements.

- **Inefficiency due to the inter-cryostat region:** The efficiency of the Level

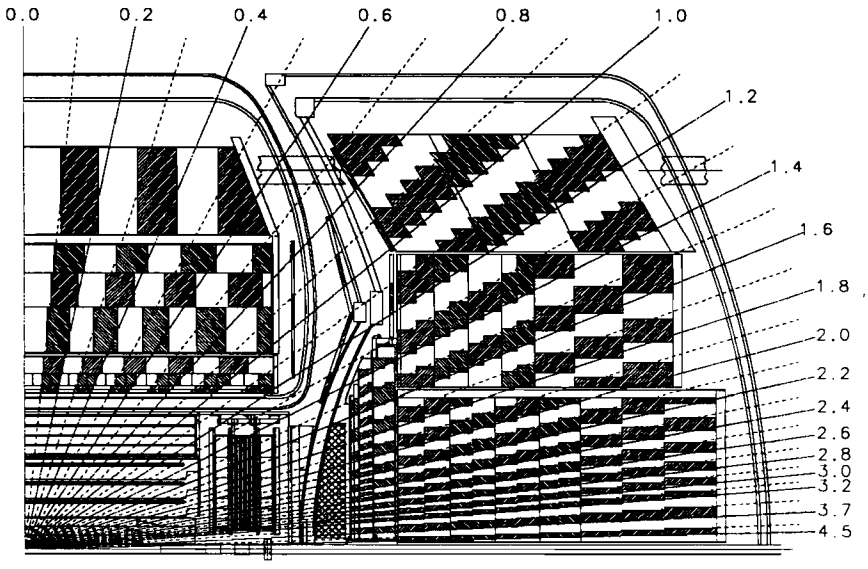

Figure 4.2: The DØ calorimeter is comprised of three cryostats. In an η region of $0.6 \leq |\eta| < 1.6$, a jet of a radius of 0.7 may deposit a significant amount of energy into the gap between the cryostats, and reduce its probability of fulfilling the Level 1 trigger requirements.

1 trigger as a function of η is related to the fact that Level 1 does not include the information from the inter-cryostat detectors. The inter-cryostat region extends from a $|\eta|$ of 0.6 to 1.6. As shown in Figure 4.2, in this region, a jet with a radius of 0.7 centered about a given η will deposit a significant amount of energy within the gap between the cryostats. Since the information of the deposition of this energy is not used in Level 1, the probability of a jet depositing the required amount of E_T within a single large tile is reduced. Level 2 does include the information from the inner cryostat detectors, so the η dependence of the jet trigger in Level 2 is greatly reduced.

- **Inefficiency due to reduced integration time:** In order to meet the

time restrictions of Level 1, the trigger readout of the energy deposited in the calorimeter is not fully integrated. Deposited energy is read as a function of time as a pulse with a large tail. The calorimeter information stored on tape has an integration time which encompasses the pulse and the majority of the tail. The calorimeter trigger information uses a reduced integration time which does not encompass the full tail. This increases the inefficiency by degrading the resolution of the calorimeter trigger.

A study was done in order to determine the E_T and η dependence of the efficiencies of the jet triggers used in this analysis. The trigger efficiencies were measured as a function of E_T in three η regions defined by the central and endcap cryostats, and the inter-cryostat region. These η regions were defined as $|\eta| < 0.6$, $0.6 \leq |\eta| < 1.6$, and $|\eta| \geq 1.6$. Since the emphasis of this analysis is to measure the dijet angular distributions in high mass regions, minimizing the final off-line E_T requirement on the data sample was not necessary. It was of far greater importance to ensure that the trigger was 100% efficient in the mass, E_T, and η regions used to measure the dijet angular distributions. For the final off-line data sample, a requirement was placed on the jet with the largest E_T in the event(the leading jet) to have an E_T greater than a threshold determined for each of the three triggers, as summarized in Table 4.2.

Table 4.2: The final E_T threshold requirements placed on the leading jet in an event.

Trigger	Off-line E_T Limit on Leading Jet(GeV)
JET 30	55.0
JET 85	120.0
JET MAX	175.0

Chapter 5

Jet Reconstruction and Corrections

The DØ data acquisition system records events as a series of data banks which hold the information collected from the various components of the DØ detector. In order to do an analysis, this detector information must be converted into physical quantities. The DØ experiment uses an off-line software package which reconstructs the properties of the physical jets, electrons, photons, and muons from the detector information. Jet reconstruction identifies a cluster of energy deposited in the calorimeter as a jet and measures its E_T and position in η, ϕ space. This chapter discusses the reconstruction of jets and the determination of corrections for the jet energy scale and the jet energy and position resolutions.

5.1 The DØ Jet Cone Algorithm

The DØ experiment uses a cone algorithm for measuring jets [15]. Simplistically, the cone algorithm forms a jet from the sum of the E_T deposited in all cells within

a cone of radius $R = \sqrt{\Delta\eta^2 + \Delta\phi^2} = 0.7$. This is similar to the algorithm used in Level 2, but to increase the accuracy of the measurement of the jet E_T and position, the DØ jet reconstruction algorithm follows a series of iterative steps: preclustering, jet clustering, and jet splitting and merging.

• **Preclustering:** First, the transverse component of the energy deposited in each calorimeter cell is summed into radial towers of $\Delta\eta \times \Delta\phi = 0.1 \times 0.1$. The E_T is calculated based on the vertex of the interaction. The towers which have an $E_T > 1.0$ GeV are then ordered in descending E_T. This is a list of seeds, or starting η, ϕ positions, for preclusters. Preclusters are formed using the following iterative process. Using the η,ϕ position of the highest E_T seed as the center axis, a precluster is formed from the sum of the E_T of all towers which have an $E_T > 1$ GeV within a cone of radius $R = \sqrt{\Delta\eta^2 + \Delta\phi^2} = 0.3$. The η,ϕ centroid of the precluster is then calculated from the E_T weighted η, ϕ positions of each tower included in the precluster. All towers included within this precluster are then removed from the list of starting seeds. The remaining preclusters are formed in a similar manner, using the position of the highest E_T seed from the seed list as the center axis of each precluster. This process continues until all towers in the seed list are used. Preclustering lowers the number of seed towers used as the starting points for jets. This reduces the computing time needed for the jet reconstruction algorithm.

• **Jet clustering:** The next step is the clustering of towers into jet cones. The list of preclusters is ordered in descending E_T, to be used as seeds for the jet cones. Beginning with η,ϕ position of the highest E_T precluster as the center axis, the E_T of all towers within a cone of radius $R = \sqrt{\Delta\eta^2 + \Delta\phi^2} = 0.7$ is summed. The E_T weighted centroid of the jet is calculated using the following formulae, where i

runs from one to the number of towers in the jet.

$$E_{T\,jet} = \sum_i E_{T\,i} \quad \eta_{jet} = \frac{\sum_i E_{T\,i} \times \eta_i}{\sum_i E_{T\,i}} \quad \phi_{jet} = \frac{\sum_i E_{T\,i} \times \phi_i}{\sum_i E_{T\,i}} \tag{5.1}$$

If the calculated jet centroid is not within a radius $R = \sqrt{\Delta\eta^2 + \Delta\phi^2} = 0.001$ of the center axis, the η and ϕ of the calculated jet position are used as the center axis, and the clustering of towers into a jet cone of radius 0.7 is repeated. This continues until the calculated jet centroid is within a radius of 0.001 of the center axis, and the location of the centroid of the jet has converged. To avoid the possibility of a jet center oscillating between two centers, the maximum number of iterations is 50. The formulae used to determine the η,ϕ position of the jet (Eq. 5.1) are 'Snowmass' angles, which are used to better agree with theory [16]. For historical reasons, once the center of the jet is found, the η,ϕ position of the jet is converted back to the original DØ angles definition described by the following formulae, where i runs from one to the number of towers in the jet.

$$\phi_{jet} = tan^{-1}\left(\frac{\sum_i E_{X\,i}}{\sum_i E_{Y\,i}}\right) \tag{5.2}$$

$$\eta_{jet} = -1.0 \times ln\left(\frac{1.0}{tan(\theta/2)}\right) \quad \theta = tan^{-1}\left(\frac{\sqrt{\sum_i E_{X\,i}^2 + \sum_i E_{Y\,i}^2}}{\sum_i E_{Z\,i}}\right) \tag{5.3}$$

If the E_T of the jet is less than 8.0 GeV, then the jet is ignored. The next jet cluster is formed using the position of the next highest E_T precluster seed as the center axis, provided that the seed is not within a radius $R = \sqrt{\Delta\eta^2 + \Delta\phi^2} = 0.35$ of the center of a previously found jet. This iterative algorithm is continued until all of the precluster seeds in the list have been used.

• **Jet splitting and merging:** Jets determined by the cone algorithm can overlap due to irregular jet shape or because of a small separation between the

jets. An additional step is added to the DØ jet algorithm to deal with overlapping jets. As each jet is determined, the algorithm checks to see if any of the towers included in the jet are included in any previously determined jets. If this is so, the jet is then either split or merged with the overlapped jet using the following algorithm. For a jet which overlaps with only one other jet, the total E_T that is shared between the two jets is summed. If the fraction of this shared E_T divided by the E_T of the jet with the lower E_T is greater than or equal to 0.5, the two jets are merged. This means that the E_T of all the towers within the two jets is summed to make a new jet. The E_T weighted η,ϕ position of the final merged jet is calculated using the original DØ angles definition described above. If the shared E_T fraction is less than 0.5, then the jets are split. Each tower from the list of towers within either jet, is assigned to the jet which has the closest center position. The η,ϕ positions of the two split jets is determined by the DØ angles definition, as with merged jets. If the jet overlaps with more than one jet, it is split or merged as described above with the jet with which it shares the most E_T. The E_T shared between the jet and the jet not split and merged is not included in the overlapped jet. Splitting and merging occurs after the requirement is placed that the jet must have an E_T greater than 8.0 GeV. Jets which have been split are not required to have an E_T greater than 8.0 GeV.

5.2 The Jet Energy Correction

Energy measured by the calorimeter as ionized charge is proportional to the true energy of an incident particle. If the calorimeter were ideal, the conversion of measured charge into energy (in units of GeV) would be accomplished with a simple calibration constant which would be independent of the type and the energy of the incident particle. In the DØ calorimeter there is some non-linearity in the

response, which is to say that the calibration constant varies with particle energy and with particle type. Initial calibration constants were obtained by measuring the charge deposited by electrons and by pions of known energies in a test calorimeter ([17], [18]). The energy obtained by using this calibration is referred to as uncorrected E_T. Since the e/π ratio of the response of the calorimeter is not exactly one, slightly different calibration constants were determined for electromagnetic particles (electrons and photons), and for hadronic particles (mostly charged pions). These measurements also determined that the response of the DØ calorimeter to pions of incident energies lower than approximately 10 GeV is significantly non-linear.

Furthermore, jets are complicated objects which contain large numbers of particles of different types with a broad energy spectrum, and this presents difficulties in determining the jet's true energy. In order to measure the true energy of a jet, one must sum the measured energies of all its constituent particles within a cone of radius $R = \sqrt{\Delta\eta^2 + \Delta\phi^2} = 0.7$. These particles are primarily neutral and charged mesons. Most neutral mesons within a jet decay into photons before hitting the calorimeter and are measured as electromagnetic particles. The energy calibration for electromagnetic objects, such as photons and electrons, was fully determined by using the known masses of the Z, J/ψ, and π^0 resonances ([19], [20]). Any objects identified as electromagnetic within a jet were corrected by the electromagnetic calibration. Due to the complex structure of the jet, not all of the photons are identified as electromagnetic objects, and are hence not properly corrected. Additionally, a significant portion of the energy in a jet due to hadronic particles is carried by pions with energies below 10 GeV. Therefore, the non-linearities of the response of the calorimeter must be accounted for in the measurement of jet energy. Additional uncertainty in the jet energy measurement is introduced by the large size of a jet in η,ϕ space. Since particles comprising the jet are distributed

over a large area in the calorimeter, some energy may be lost in regions of the calorimeter which are poorly instrumented. Since the calorimeter is composed of three independent cryostats, systematic differences in their calibration constants must be measured. The measured jet energy is contaminated by uranium noise from the decay of nuclei, and pileup of events due to high luminosities. There is also contamination due to energy deposits from beam remnants and spectator interactions (the underlying event). The jet energy correction [21] was determined in order to correct for all of these effects.

The jet energy correction takes the form of the following equation.

$$E_{jet} = \frac{(E_{measured} - O)}{((1 - S) \times R_{had})} \tag{5.4}$$

O is the offset due to noise, pileup, and the underlying event. S is the correction factor for loss of energy due to particles within the jet cone which shower beyond the cone boundaries. This term is negligible for the cone size of radius $R = \sqrt{\Delta\eta^2 + \Delta\phi^2} = 0.7$ used for this analysis, for all but the most forward η's. R_{had} is the response of the calorimeter to the components of a jet not identified as electromagnetic objects.

• **The offset:** The offset, O, was determined as the sum of two components: the underlying event, and the noise. The distribution of energy deposited in the calorimeter due to the underlying event was assumed to be similar to that of the soft interactions of minimum bias events. Minimum bias events are produced by non-diffractive inelastic collisions. The offset due to the underlying event was measured by studying the average E_T density as a function of detector η for minimum bias events. Detector η is defined as the η determined from the nominal vertex at $z = 0$, as opposed to the physics η which is determined from the interaction vertex. It was assumed that the underlying event is twice as large for events

with two interactions as for events with a single interaction. Events with a single interaction were separated from those with multiple interactions by using a multiple interaction tool, which, among other things, looked at the RMS deviation of the time differences measured in Level 0, and the magnitude of the energy deposits measured in the end cap calorimeters. Since the tool cannot determine the exact number of interactions, a low luminosity minimum bias sample was used to ensure that the number of interactions in a multiple interaction event was two. The underlying event was measured as the difference between the E_T density for events with two interactions and that for events with a single interaction. The average number of interactions as a function of luminosity was determined, and this was used in order to obtain the dependence of the underlying event on luminosity. The noise component of the offset was measured as the difference between the E_T density of single interactions and the measured underlying event for a single interaction. The total offset correction, O, is on the order of 2 GeV for a jet cone with a radius $R = \sqrt{\Delta\eta^2 + \Delta\phi^2} = 0.7$.

• **The response:** The dominant factor in the energy correction is the response of the calorimeter, R_{had}. Since the initial momentum of the beam is in the longitudinal (along the z axis) direction, transverse momentum (in the x,y plane) must balance due to conservation of momentum. For high energy jets the magnitude of the transverse momentum is approximately the same as the transverse energy ($P_T \approx E_T$), so the E_T must sum vectorally to zero. An imbalance would be measured as missing E_T ($\not\!\!E_T$). For an event with two objects, say a photon and a jet, the E_T's of these two objects must balance. Photons are relatively simple objects, which are well collimated in η, ϕ space, and their energies are entirely measured within the electromagnetic portion of the calorimeter. Thus, the measured energy of a photon is well known. Any imbalance in the E_T in a photon-jet event can be interpreted as an error in the measurement of the energy of the jet. Photon-jet

events can therefore be used to determine the final calibration of the response of the calorimeter to a jet. Studying the balance of the E_T of a photon with the E_T of a jet can be complicated by the fact that jets can radiate particles outside of the jet cone, which would cause an imbalance between the jet and the photon due to physics rather than the response of the calorimeter. The impact of this uncertainty is minimized by studying the ratio of the component of the $\not\!\!E_T$ projected into the direction of the photon over the E_T of the photon, the $\not\!\!E_T$ projection fraction, or MPF. Mathematically, the MPF is

$$-1.0 \times \frac{\vec{\not\!\!E}_T \bullet \hat{n}_\gamma}{E_{T\gamma}} \tag{5.5}$$

The MPF will contain the information of any other radiated particles which balance the photon, as well as containing the information of any E_T imbalance between the jet and the photon. The MPF is the opposite of the mismeasured jet energy. The response of the calorimeter to the jet is described by the following formula.

$$R_{had} = 1 + \frac{\vec{\not\!\!E}_T \bullet \hat{n}_\gamma}{E_{T\gamma}} \tag{5.6}$$

In order to fully calibrate the response of the calorimeter to jets with a wide range of energies, R_{had} was measured in the following manner. First the response was measured in the central cryostat (CC) as a function of $E' = E_{T\gamma} cosh(\eta_{jet})$. The jet was required to be within the CC, $|\eta| < 0.7$. The statistical sample of photon-jet data within the CC only allowed the response to be measured up to energies of approximately 150 GeV. In order to extend the measurement of the response to energies greater than 150 GeV, the response was measured in the end cap cryostat (EC), again as a function of E'. The jet was required to be within the EC, $1.8 < |\eta| < 2.5$. In order to account for the systematic differences in response

between the CC and EC, the ratio of the response in the CC to the response in the EC was measured for those energies for which they overlapped ($90 < E' < 180$ GeV). This ratio, called the cryostat factor, was used to normalize the response as a function E' measured in the EC to that measured in the CC. This provided a complete calibration of jet energies in the CC from approximately 10 GeV to 500 GeV, as shown in Fig. 5.1. The response as a function E' measured in the CC was then normalized using the inverse of the cryostat factor, in order to obtain a complete calibration of jet energies in the EC. In the inter-cryostat region, the calibration of jet energies was normalized by the linear extrapolation as a function of η of the response difference between the CC and the EC.

In order to convert the jet energy correction measured as a function of E' into a correction as a function of the measured uncorrected E_T of a jet, the average uncorrected jet energy was measured as a function of E', as shown in Fig. 5.2. The complete jet energy correction factor is shown as a function of uncorrected E_T in Fig. 5.3. The correction varies from approximately 0.95 for jets with an uncorrected E_T of 10 GeV to approximately 1.17 for jets with uncorrected E_T above 100 GeV.

5.3 The Jet Energy and Position Resolutions

5.3.1 Jet Energy Resolution

The jet energy correction described in the previous section is a correction based on the average response of the calorimeter to jets. In reality, the response of the calorimeter to a sample of jets of a particular energy and position in η is not a single number, but has a distribution, which is approximately gaussian, about the mean response. This distribution of the response of the calorimeter is called the jet energy resolution and is due to many factors.

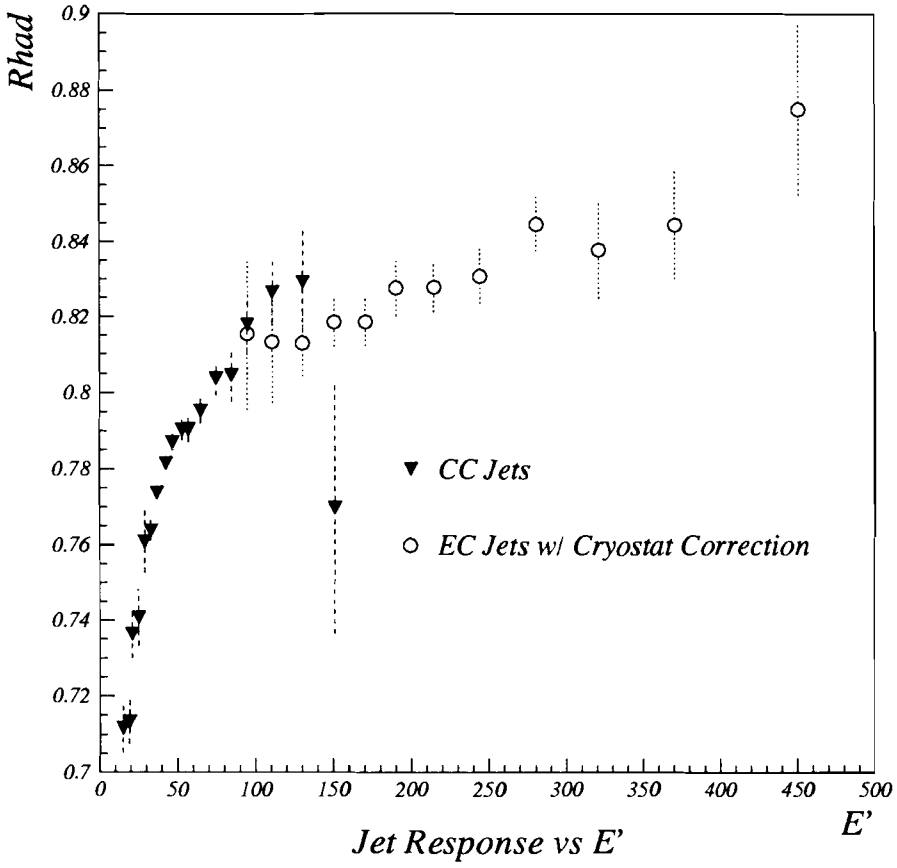

Figure 5.1: The response of the calorimeter to jets in the CC and EC cryostats is shown versus E'. The solid triangles are the response measured in the CC and the open circles are the response measured in the EC.

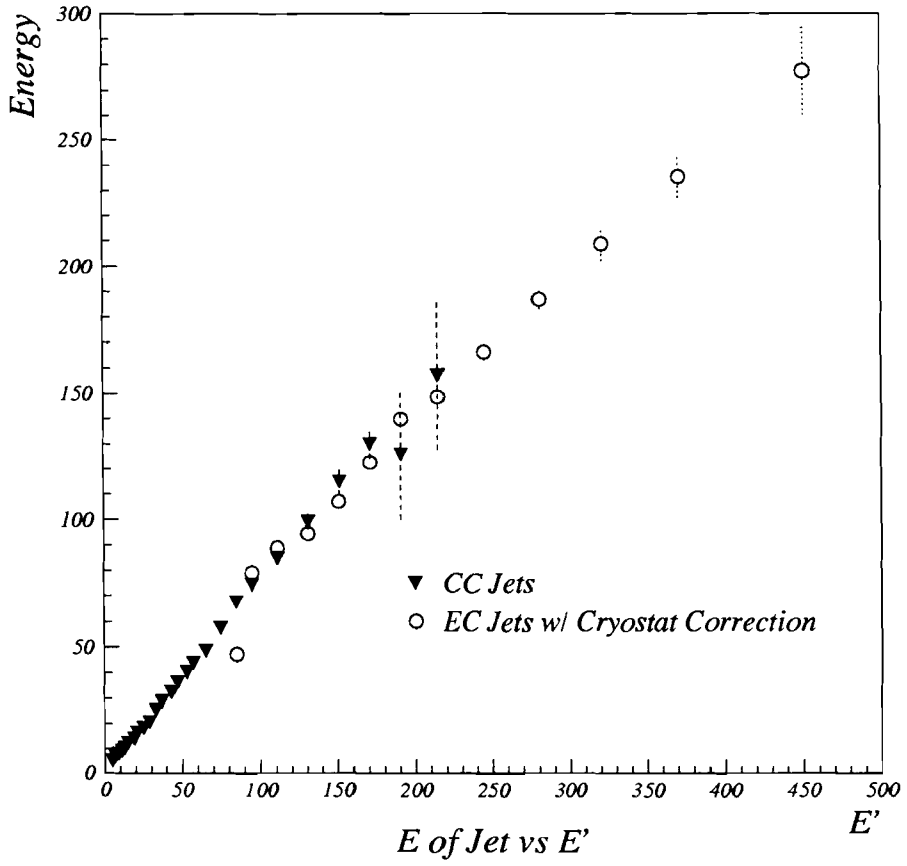

Figure 5.2: The average uncorrected jet energy is shown as a function of E', measured in the CC and EC cryostats. The solid triangles are the response measured in the CC and the open circles are the response measured in the EC.

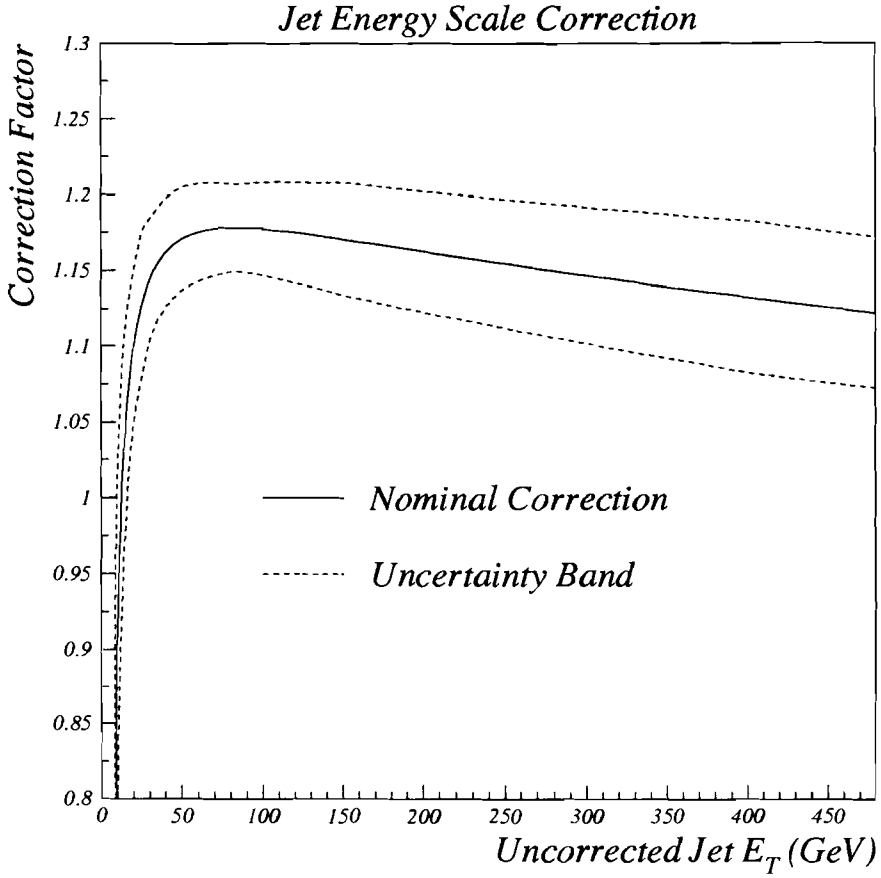

Figure 5.3: The jet energy correction factor is shown versus the uncorrected jet E_T for jets in the CC cryostat ($|\eta| < 0.5$). The dotted lines indicate the error on the correction.

The DØ calorimeter is a sampling calorimeter, and therefore has an intrinsic energy resolution, even for a sample of mono-energetic particles. Define $\frac{\sigma(E)}{E}$ as the resolution. The resolution of a 'perfect' sampling calorimeter is then:

$$\frac{\sigma(E)}{E} = \frac{\sigma_o}{\sqrt{E}} \tag{5.7}$$

σ_o is conceptually related to the calibration constant of the calorimeter. The amount of charge detected in the calorimeter is proportional to the number of particles, N_P, created when the incident particle showers in the calorimeter. N_P is then related to the energy of the incident particle, E, by some calibration constant, κ.

$$N_P = \kappa \times E \tag{5.8}$$

For a poisson distribution, the width of the distribution of N_P for a sample of measured incident particles with the same energy, E, is given by the following relation.

$$\frac{\sigma(N_P)}{N_P} = \frac{\sqrt{N_P}}{N_P} \tag{5.9}$$

Using the relationship between N_P and the energy, E, the intrinsic energy resolution of a sampling calorimeter is then described by the following relation.

$$\frac{\sigma(E)}{E} = \frac{\sqrt{\kappa}}{\sqrt{E}} \tag{5.10}$$

As previously described, jets are composed of many particles of different types and different energies. A sample of jets of the same energy will have a distribution of the fraction of the energy of the jet carried by electromagnetic particles, as well as a distribution of the fraction of the energy of the jet carried by hadronic particles with energies less than 10 GeV. If the calorimeter were perfectly linear as a

function of energy, and had the same response to hadronic and to electromagnetic particles, the energy resolution for a jet would still be described by $\frac{\sigma_E}{E} = \frac{\sigma_o}{\sqrt{E}}$. But, the calorimeter is non-linear for hadrons with energies less than 10 GeV, and its response to electromagnetic particles is different from its response to hadronic particles. All of this contributes to the width of the energy resolution.

The total energy resolution of a jet measured in the DØ calorimeter, is of the following form.

$$\frac{\sigma(E)}{E} = \sqrt{\frac{N^2}{E^2} + \frac{S^2}{E} + C^2} \tag{5.11}$$

The noise term, N, describes the contribution to the energy resolution from the distributions of instrumental noise, uranium noise, and other detector effects. The sampling term, S, is primarily the intrinsic resolution of the DØ calorimeter. The 'constant' term, C, is the contribution of fluctuations which are weakly dependent on the energy of the jet, such as the non-linearities of the response.

The jet energy resolution was measured by studying the asymmetry of the response of the calorimeter to dijet events [22]. The E_T of the two jets in a dijet event must balance. This balance is measured by using the jet asymmetry, which is described by the following formula.

$$A = \frac{E_{T1} - E_{T2}}{E_{T1} + E_{T2}} \tag{5.12}$$

E_{T1} is randomly chosen from one of the two leading jets, and E_{T2} is the other. The variance of the asymmetry can be described by the following relation.

$$\sigma_A^2 = \left|\frac{\partial A}{\partial E_{T1}}\right|^2 \sigma_{E_{T1}}^2 + \left|\frac{\partial A}{\partial E_{T2}}\right|^2 \sigma_{E_{T2}}^2 \tag{5.13}$$

If one assumes that $E_T \equiv E_{T1} = E_{T2}$ and $\sigma_{E_T} \equiv \sigma_{E_{T1}} = \sigma_{E_{T2}}$, then the jet energy

resolution as a function of E_T can be described in terms of σ_A.

$$\left(\frac{\sigma_{E_T}}{E_T}\right) = \sqrt{2}\,\sigma_A \tag{5.14}$$

Using this relationship the jet energy resolution as a function of E_T was measured by studying the asymmetry of dijet events in regions of the jet pseudorapidity, η. The jet energy resolution was parameterized using the following formula.

$$\frac{\sigma(E_T)}{E_T} = \sqrt{\frac{N^2}{E_T^2} + \frac{S^2}{E_T} + C^2} \tag{5.15}$$

The resulting parameters are summarized in Table 5.1.

Table 5.1: The jet energy resolution measured in six regions of η is parameterized as a function, $\frac{\sigma(E_T)}{E_T} = \sqrt{\frac{N^2}{E_T^2} + \frac{S^2}{E_T} + C^2}$. The dominant term in this function is the term associated with the sampling parameter, S. The noise and constant term are primarily for improving the fit of the curve to the data.

η Region	N	S	C
$\lvert\eta\rvert \leq 0.4$	4.185	0.655	0.0
$0.4 < \lvert\eta\rvert \leq 0.8$	4.998	0.678	0.0
$0.8 < \lvert\eta\rvert \leq 1.2$	1.799	0.964	0.0
$1.2 < \lvert\eta\rvert \leq 1.6$	0.003	0.949	0.0293
$1.6 < \lvert\eta\rvert \leq 2.0$	3.402	0.659	0.0
$2.0 < \lvert\eta\rvert \leq 3.0$	4.664	0.433	0.0

5.3.2 Jet Position Resolution

The jet position in pseudorapidity, η, also has a distribution for a sample of jets which are created from partons of a particular energy and position. This distribution is due to both physics and detector effects. A jet is defined in this analysis as the sum of all the particles within a cone of radius $R = \sqrt{\Delta\eta^2 + \Delta\phi^2} = 0.7$.

The position of a jet is determined based on the distribution of energy within the jet cone. Fluctuations in the fragmentation of a jet, when combined with the non-linearities and spatial non-uniformities of the calorimeter response, cause the measured pseudorapidity of a sample of jets to fluctuate around its true value. The jet position resolution is also due to the actual size of the calorimeter cells.

The jet position resolution was measured as a function of the energy of the jet and the position of the jet in η, by comparing Herwig Monte Carlo samples [23], [24]. The variance of the pseudorapidity distribution as a function of energy and detector η , $\sigma_\eta(E, \eta_d)$, was determined by measuring the variance of the distribution of the difference of the η of a jet formed from the Monte Carlo particle information, and the reconstructed η of a jet formed from the Monte Carlo calorimeter information. The variance was measured to be quite small, and was approximated as $\sigma_\eta = 0.06$.

Chapter 6

Analysis

Measuring a dijet angular distribution is essentially a counting experiment in which we count the number of events which occur within each of a series of regions defined by the mass and χ of a dijet pair. The goal of this counting experiment is to compare the measured dijet angular distributions to the distributions predicted by perturbative QCD. For this comparison to have meaning, any inefficiencies or backgrounds which may erroneously alter the measured distributions must be removed or taken into account. This chapter describes the analysis which was done to extract a measurement in which we have confidence from the collected data sample. The main attributes of this analysis are the following:

- **Event Selection:** A series of requirements are placed on the collected data sample in order to remove spurious events. Cosmic rays, accelerator effects, and instrumental noise can create false energy deposits within the calorimeter. These false energy deposits can be reconstructed as fake energy within a jet. Event selection requirements are placed to avoid events containing these spurious jets. Inefficiencies in the event selection requirements are taken into account through an applied correction.

• **Acceptance Limits on Mass, χ, and η_{boost}:** Limits are placed on the kinematic variables of mass, χ, and η_{boost} in order to exclude regions which either have large backgrounds or uncertain efficiencies. These are, in part, inefficiencies due to trigger requirements and jet reconstruction, as well as the physical limits of the detector.

• **Systematic Errors:** As a final step in the analysis, remaining systematic errors are studied in order to understand the accuracy of the measurement. These errors are primarily due to detector effects and the jet energy scale correction.

6.1 Event Selection

The data sample used to measure the dijet angular distributions was an inclusive dijet sample, which is a sample of events with two or more jets. This section discusses the off-line selection requirements placed on the jet and overall event quality of the data sample in order to remove or reduce the number of false events [25]. Corrections applied to the data sample, in order to account for selection requirement inefficiencies and in order to correct for biases in the event reconstruction, are also discussed.

6.1.1 Requirements for Jet Quality

Jet quality requirements were placed on the EM fraction, the CH fraction, and the hotcell fraction of a jet in order to remove events with fake or contaminated jets. Only the information from the two jets with the highest E_T in an event was used to determine the mass and χ bin in which the event belongs. Therefore, events were removed from the sample unless both of the leading two jets fulfilled the jet quality requirements. There were no quality requirements placed on any other jets

in an event.

• **EM fraction:** The fraction of the energy of a jet deposited in the electromagnetic layers of the calorimeter, the EM fraction, can be used to eliminate electromagnetic objects, such as electrons and photons, from the jet sample. The EM fraction was required to be greater than 0.05 and less than 0.95 in the central and end cap calorimeters. In the inter-cryostat region, the electromagnetic layers of the calorimeter are reduced or missing, so the EM fraction was only required to be less than 0.95.

• **CH fraction:** As mentioned in Chapter 3, the main ring of the Fermilab Collider runs through the coarse hadronic section of the calorimeter. In order to remove events which were contaminated by main ring activity, the fraction of the energy of a jet deposited in the coarse hadronic layers of the calorimeter was required to be less than 0.4.

• **Hotcell fraction:** Occasionally, a calorimeter tower can include an extremely noisy cell, a 'hotcell'. A hotcell can contaminate a jet with false energy. Hotcell contamination was removed from the data sample by requiring that the ratio of the energy deposited in the calorimeter cell of the highest energy within a jet over the energy deposited in the next highest cell within a jet be less than 10.

The efficiencies of the jet quality requirements have been measured [26], and are approximately 97% to 92%. A correction was applied to each event in order to correct for jet quality requirement inefficiencies.

6.1.2 Requirements for Event Quality

Event quality requirements were also placed on the missing E_T fraction and the vertex of the interaction in order to remove events biased by detector defects.

• **Missing E_T fraction:** In a dijet event, transverse momentum must balance

due to conservation of momentum. For high energy jets the magnitude of the transverse momentum is approximately the same as the transverse energy ($P_T \approx E_T$), so the E_T must sum vectorally to zero. Therefore, a requirement placed on the imbalance in the E_T of a dijet event, the missing E_T, is another method of removing those events which have been contaminated by false energy deposits. The fraction of the missing E_T in an event over the E_T of the leading jet was required to be less than 0.7.

• **Interaction vertex:** The calorimeter was built to project from a vertex of 0, but the interaction vertex has a gaussian distribution centered about 0 with a $\sigma \approx$ 30cm. A vertex offset can cause an increase in detector effects which are due to the fixed positions of the calorimeter towers. In order to reduce these vertex-dependent detector effects, the vertex of the event was required to be within 50 cm of the nominal vertex.

6.1.3 Corrections for Event Reconstruction

The data were corrected for biases in the event reconstruction. In particular, corrections were applied in order to replace jet energy lost in an event due to an algorithm used to remove hot cells from the calorimeter, and to correct events with incorrectly reconstructed vertices.

• **'Hot cell killer' correction:** During the data acquisition run, there was a requirement placed on-line which removed, from the total energy of a jet, the energy deposited in cells which were labelled as noise by the 'hot cell killer' algorithm. Although this 'hot cell killer' was effective in other physics analyses, it was found that in the jet data sample, sometimes, energy was removed which belonged within the jet. A correction was made to replace in a jet the energy from a cell labelled as noise if it was within a radius $R = 0.7$ of the jet's center and was less than 50%

of the jet's total energy. This correction reduced the average missing E_T in these events.

• **Vertex correction:** For those events in which multiple vertices were found, occasionally an incorrect vertex was used which would cause an error in the calculation of the E_T and the η,ϕ positions of the jets in the event. For this analysis, the chosen vertex of the event was the vertex which had a minimum H_T, where H_T is the scalar sum of the E_T of the jets in the event. Using this method, a new vertex was chosen in approximately 10% of the events.

6.2 Acceptance: Limits on Mass, χ, and η_{boost}

Acceptance can be defined as the number of events which are counted in a particular region of mass and χ divided by the number of events which belong in that region. In order to take an accurate measurement of a dijet angular distribution, the acceptance must be very close to 100%. Inefficiencies which can not be taken into account by a correction can cause the acceptance in a mass and χ region to be less than 100%. These inefficient regions are avoided through restrictions placed on the mass, χ, and η_{boost}. Recall that the goal of this analysis is to measure the distribution of the dijet center-of-mass scattering angle as a function of the variable χ in regions of the dijet invariant mass. Four mass bins were chosen in order to maximize the number of events, while trying attain a maximum χ range of around 20 and retaining nearly 100% acceptance. The mass, χ, and η_{boost} limits are described in Table 6.1. This section discusses how the mass, χ, and η_{boost} limits were determined.

Table 6.1: Limits were placed on the mass, χ, and $\eta_{\rm boost}$ in order to have 100% acceptance in the regions in which the dijet angular distributions were measured.

Min E_{T1} (GeV)	Mass (GeV/c^2)	χ_{max}	$\lvert\eta^{\star}_{max}\rvert$	$\lvert\eta_{\rm boostmax}\rvert$
55	$260 < M_{JJ} < 425$	20	1.5	1.5
120	$475 < M_{JJ} < 635$	13	1.3	1.5
120	$M_{JJ} > 550$	18	1.45	1.5
175	$M_{JJ} > 635$	11	1.2	1.5

6.2.1 Limits on Mass and χ

For each jet trigger, the E_T of the leading jet in an event was required to be above a minimum value to exclude regions in which the trigger was inefficient. Using the restrictions on E_T, the corresponding limits in mass and χ were calculated in order to restrict the measurement to those regions in which there was 100% acceptance. For each jet trigger, a mass region was chosen which would maximize the use of the statistical sample given by the jet trigger while also maximizing the range in χ. The limits on mass and χ were calculated using the kinematic relationship between mass, χ, and E_T, which is visualized in Figure 6.1. The maximum χ with 100% acceptance in a given mass range was determined from the E_T requirement placed on the leading jet using the following formula.

$$M_{JJ}^2 = 2E_{T1}^2(\cosh(\ln(\chi)) + 1) \tag{6.1}$$

In this formula, the E_T's of the two jets are assumed to be identical and equal to the E_T of the leading jet in order to fully exclude regions of χ in which acceptance was not 100%.

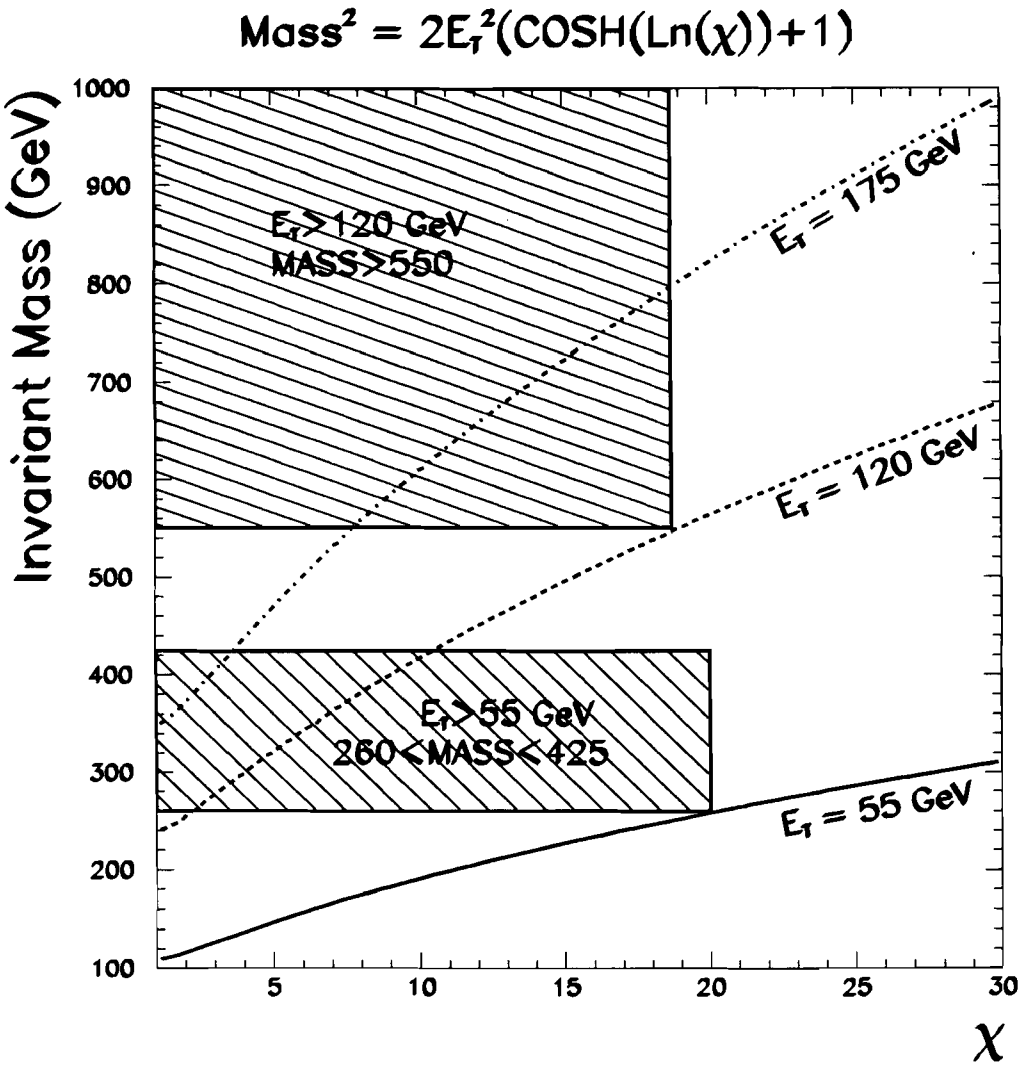

Figure 6.1: In the mass versus χ plane, the curves shown are contours of constant E_T which correspond to the off-line E_T thresholds used in this analysis. The simplest form of uniform acceptance in this plane is a rectangle. For a chosen mass region, the limit on χ corresponds to the intersection of the lower mass limit and the E_T contour. The two hatched regions shown are two of the mass bins chosen for this analysis.

6.2.2 Limits on $\eta_{\rm boost}$

The η range in which the leading two jets could be measured was restricted to $|\eta| < 3.0$ due to the finite size of the calorimeter and our current abilities to properly measure η dependent detector effects. A limit was placed on the $\eta_{\rm boost}$ of the dijet pair in order to restrict the measurement of the dijet angular distribution to an angular region where there is 100% acceptance. Recall that by transforming the measured η's of two leading jets in the lab frame to $\eta^\star$ in the center-of-mass frame, the shape of an angular distribution becomes independent of the boost of a dijet pair, so we can choose an arbitrary range in $\eta_{\rm boost}$.

The $\eta_{\rm boost}$ limit was calculated using the relationship between $\eta_{\rm boost}$, $\eta^\star$, and the maximum laboratory η allowed in this analysis, η_{max}. First, we converted the χ limit into a limit on $\eta^\star$, using the relation defined in Chapter 2:

$$\chi = e^{2|\eta^\star|} \tag{6.2}$$

In the η_1 versus η_2 plane, contours in $\eta_{\rm boost}$, and $\eta^\star$ appear as a grid of perpendicular lines, as shown in Figure 6.2. η_1 and η_2 are the η's of the leading jet and the second leading jet, respectively. Given the limit on $\eta^\star$, the limit on $\eta_{\rm boost}$ is simply the value that limits the distribution to a rectangle which resides completely within the limits placed on η_1 and η_2. Mathematically, this limit can be described by the following formula:

$$|\eta_{\rm boost}| + |\eta^\star| < |\eta_{\rm max}| \tag{6.3}$$

where $\eta_{\rm max} = 3.0$. The $\eta_{\rm boost}$ limit is kept at 1.5 for all mass bins for simplicity, although a larger $\eta_{\rm boost}$ cut is possible for some mass bins.

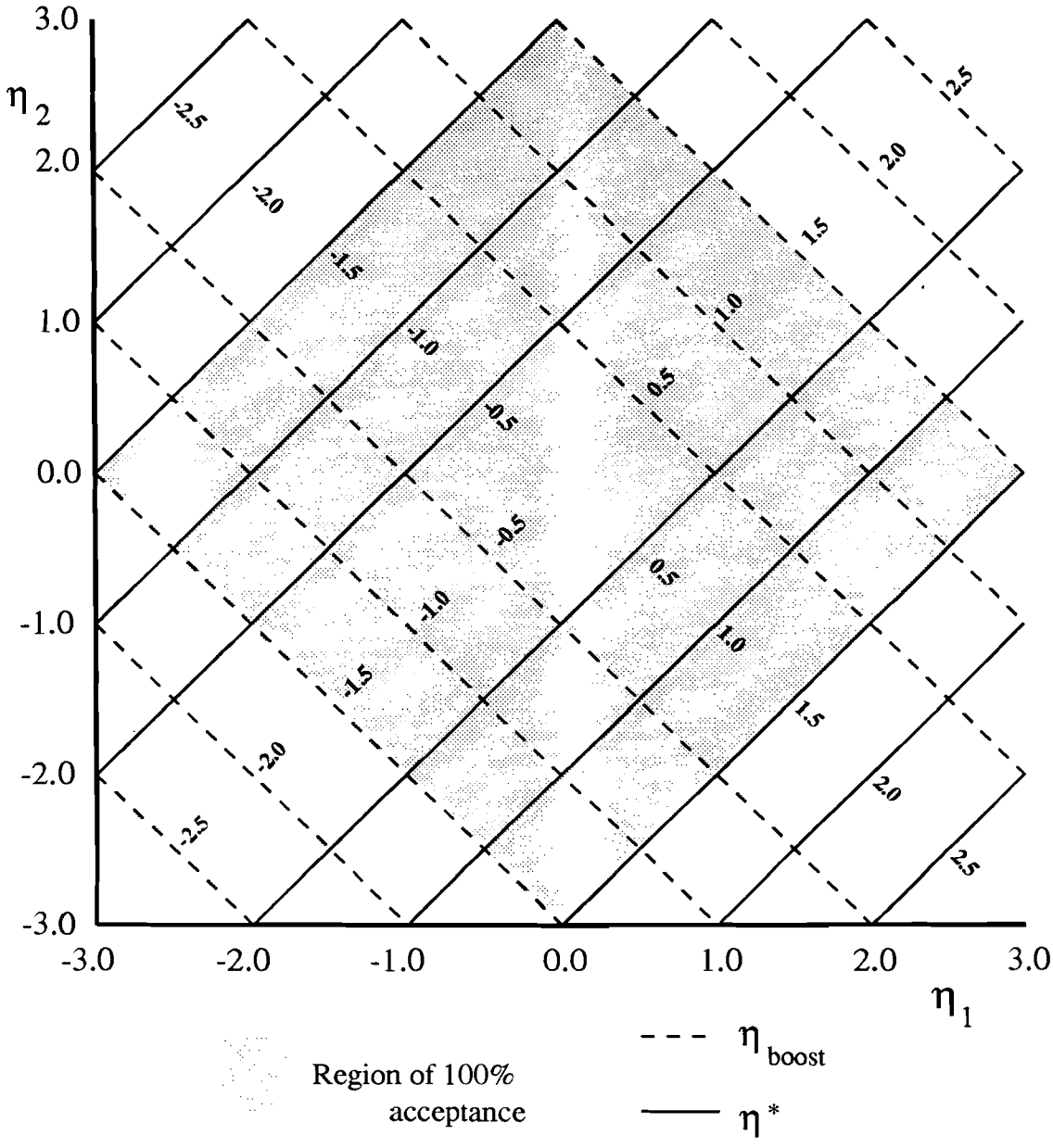

Figure 6.2: The η's of the two leading jets were required to be less than 3.0. For a maximum η^* of 1.5, the η_{boost} was chosen to be less than 1.5 to restrict the measurement of the dijet angular distribution to a region with 100% acceptance.

6.3 Systematic Errors

A systematic error is defined as an error introduced by an intrinsic inaccuracy in the experimental system. The purpose of this analysis is to compare the shapes of the experimental angular distributions of parton-parton scattering to those predicted by perturbative QCD. In determining the systematic error on the measured dijet angular distributions, only those experimental factors which alter the shapes of the dijet angular distributions are of interest. There are two main categories of experimental factors which contribute to the systematic error: biases due to event selection requirements and corrections, and inaccuracies in measuring the properties of jets. Most systematic errors due to spurious events and detector effects were removed through the event selection requirements and corrections. But, these requirements and corrections themselves may cause a bias in the angular distributions and must be taken into account in the systematic error. Some of the inaccuracies in measuring the properties of jets are due to the jet algorithm. The experimental factors associated with the jet algorithm which contribute to the systematic error are the jet splitting and merging, and the jet η bias. Additional experimental factors which contribute to the systematic error are those associated with measuring the E_T of a jet: the jet energy scale correction, the jet energy resolution, and the η-dependence of the energy scale. This section discusses how the systematic error on the shape of each distribution was determined. Table 6.2 shows, for each mass region, a complete list of each experimental factor which contributes to the systematic error, the contributed systematic error averaged over the number of bins in χ, and the maximum systematic error. Most systematic errors due to the event selection requirements and the inaccuracy of the measurements of the properties of a jet are minimal in comparison to the statistical error, which is approximately 5%. Some experimental factors, such as the error due to

jet splitting and merging, contribute as much as 9% to the systematic error in particular regions of χ. These may be fluctuations due to statistical error that were not removed by our method of determining the systematic error. The dominant systematic error is due to the residual η-dependence of the energy scale. The final systematic error is the sum in quadrature of the error of each contributing variable.

Table 6.2: Shown are the experimental factors which contribute to the systematic error for each mass region. The approximate error on the shape of the dijet angular distribution is shown as the maximum error and the error averaged over the number of bins in χ in the distribution. The numbers shown do not fully describe the systematic error. The error is only fully described by the shape of the systematic error curve as a function of χ.

Exp. Factor	$260 < M_{JJ} < 425$		$475 < M_{JJ} < 635$		$M_{JJ} > 550$		$M_{JJ} > 635$	
	Max	Avg	Max	Avg	Max	Avg	Max	Avg
Jet & Evt Quality	4%	1%	3%	1%	4%	2%	7%	3%
Quality Efficiency	2	1	2	1	3	1	4	2
Mult. Interactions	2	1	3	1	4	1	2	1
Jet Split & Merge	3	2	3	1	9	3	8	4
Jet Energy Scale	4	1	2	0	3	0	7	3
Jet Resolution	3	1	4	2	7	3	4	1
η bias	3	1	2	1	4	1	4	2
η Dep E Scale	4	1	6	2	9	5	10	4

6.3.1 Determination of the Systematic Error

In order to determine the systematic error, the influence of each experimental factor on the shape of the angular distribution was studied. A comparison of the shape of the nominal distribution to that of a test distribution with(or without) a requirement or correction based on an experimental factor was made by looking at the ratio of the two distributions (test over nominal). For instance, the effect on the shape of the angular distribution due to the jet quality requirements was

studied by looking at the ratio of the angular distribution without jet quality requirements over the nominal distribution, as shown in Figure 6.3. It is difficult to determine any effect on the shape from this ratio due to the large statistical errors. In order to determine any systematic change in shape, we fit the test and nominal distributions with a function: $F = A + B\chi + C/\chi + D/\chi^2 + E/\chi^3$. This function was chosen because the general form of the dijet angular distributions predicted by QCD contains factors of χ and $\frac{1}{\chi}$. The $\frac{1}{\chi^2}$ and $\frac{1}{\chi^3}$ terms were added to improve the fit. The systematic error in percent was extracted from the ratio of the two parameterized curves, shown in Figure 6.4, by assuming that the error is symmetric, and calculating the absolute value of one minus the ratio as a function of χ.

6.3.2 Systematic Errors Due to Event Selection and Corrections

This section discusses the contribution to the systematic errors of the jet and event quality requirements, the jet and event quality efficiency corrections, and multiple interactions.

- **Jet and event quality requirements:** The jet quality requirements are necessary for removing false energy deposits from the event sample. Even so, their effect on the shape of the angular distribution is , on average, 2%. The missing E_T requirement and the vertex requirement are also necessary to retain a clean event sample. Their effect on the angular distribution is, on average, 1%.

- **Jet and event quality efficiency corrections:** The jet and event quality efficiency corrections are approximately 92 - 97%. The effect on the shape of the angular distribution is, on average, 1%.

- **Multiple Interactions:** Recall that the Tevatron does not specifically col-

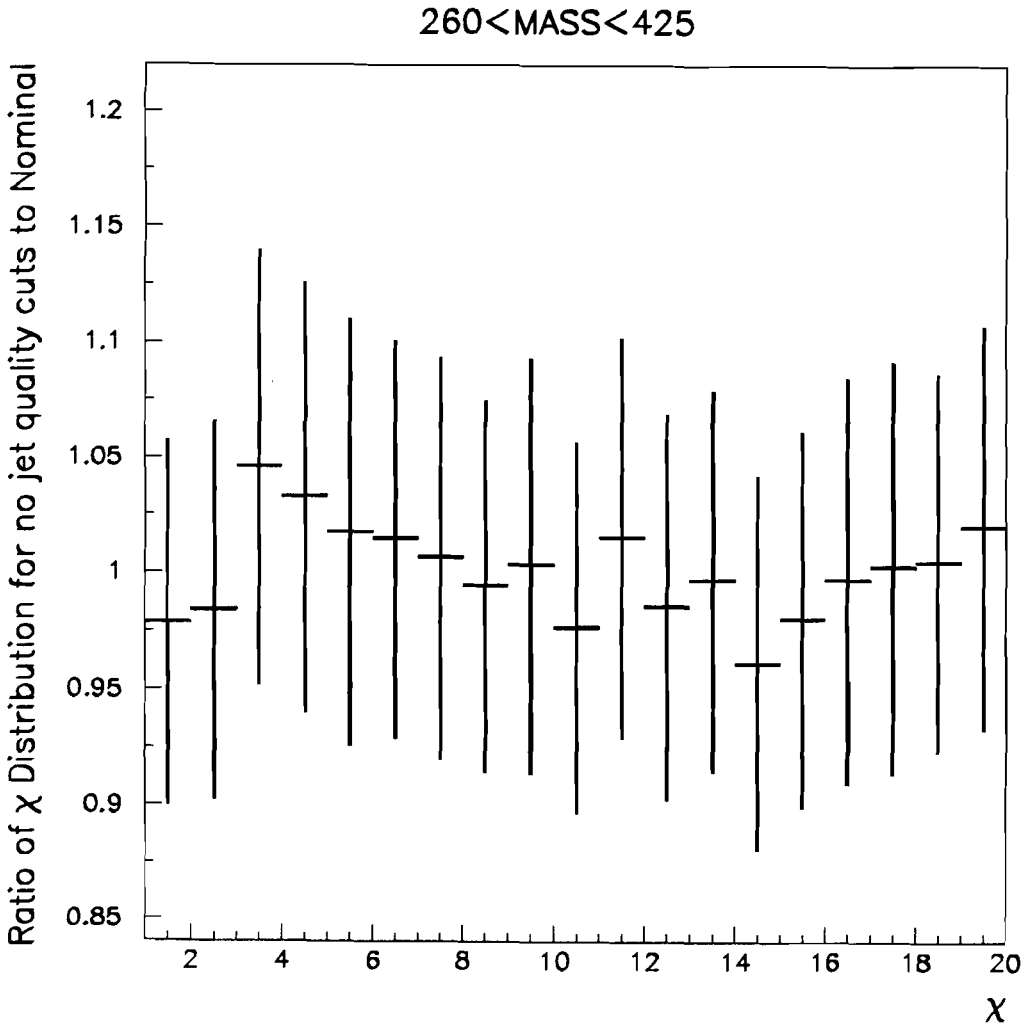

Figure 6.3: Because of large statistical errors, it is difficult to see any change in shape by looking at the ratio of two distributions. Shown here is the ratio of the angular distribution without jet quality requirements over the nominal distribution.

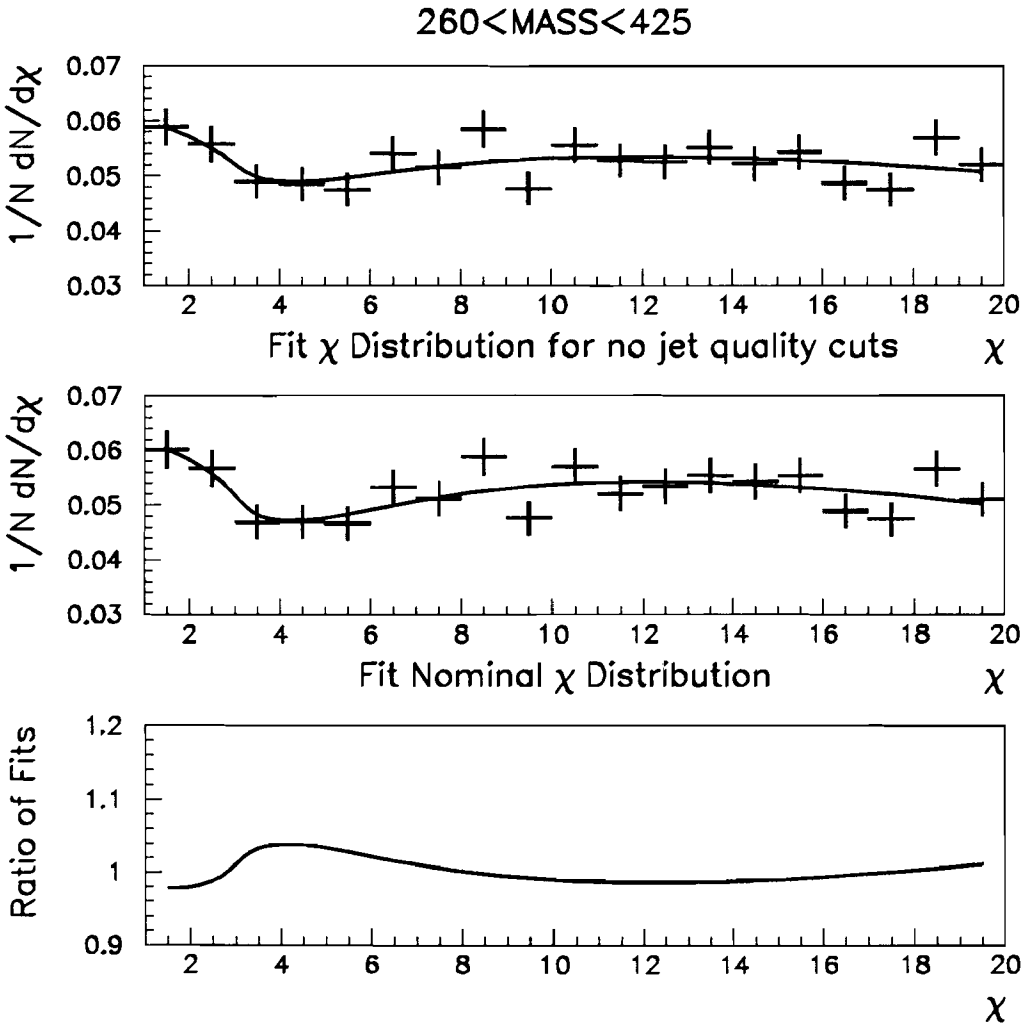

Figure 6.4: Taking the ratio of two parameterized curves allows us to see changes in the shape of the distribution due to removing jet quality requirements.

lide individual protons with individual antiprotons, but bunches of protons circling counterclockwise encounter bunches of antiprotons circling clockwise. These two bunches are collimated at the interaction point in order to facilitate collisions. Because of this, the number of interactions is not restricted to one. The probability of a second, or third, interaction increases as the luminosity increases. A second interaction is, with high probability, a minimum-bias interaction, which is characterized by two jets at very low E_T's (of a few GeV). Multiple interactions in an event can cause confusion in measuring the properties of a single interaction. Many analyses exclude events with multiple interactions in order to avoid this possible error. Events with multiple interactions are excluded by utilizing a multiple interaction tool which discriminates between single and multiple interactions. We chose not to place a requirement on the number of interactions in an event because the efficiency of the multiple interaction tool is not well understood, and may have some η dependence which would bias the angular distribution.

The errors introduced by a secondary interaction were studied in order to determine the effect of including events with multiple interactions. A secondary interaction adds approximately 0.6 GeV of E_T per unit of η, ϕ. Since the angular distributions are measured in regions in which the E_T's of the two leading jets are in excess of 50 GeV and are often above 100 GeV, the effect on the E_T's of the two leading jets due to this additional energy is negligible. It is possible that a second interaction may produce a vertex which is incorrectly reconstructed as the primary vertex for the leading two jets. This would cause an error in the measured η positions, as well as the measured E_T's of the jets. We studied the effect of switching from the primary vertex to the secondary vertex if the secondary vertex minimizes the H_T in the event. This had a negligible effect on the angular distribution.

It is also possible that the vertex produced by a second interaction is the only vertex reconstructed in the event. This would cause an error in the measured η

positions and E_T's of the jets. We studied the possibility of multiple interactions affecting the angular distribution in this manner by the following method. For 20% of events, we switched the vertex to a randomly chosen vertex. The new vertex was based on the measured vertex distribution, which is a gaussian distribution with a mean of approximately 0 and a width, $\sigma \approx 30$cm. We then recalculated the η positions and E_T's of the two leading jets in the event and measured the angular distribution. The percentage of events in which the vertex was switched to a new vertex was determined based on the approximate efficiency of vertex reconstruction for events with large E_T jets ($\epsilon_{vertex} \approx 70\%$), and the approximate percentage of multiple interactions in the data used for this analysis ($N_{MI} \approx 60\%$). The effect on the angular distribution is small and on average 1%.

Figure 6.5 shows the resulting ratio curves of the systematic studies of the errors due to the event selection requirements and corrections.

6.3.3 Systematic Errors Due to Accuracy of Jet Measurement

This section describes the contribution to the systematic error due to the splitting and merging attributes of the jet algorithm, the overall energy scale correction, the resolution, and the η bias.

- **Splitting and merging:** The jet algorithm used in this analysis allows for the splitting and merging of jets which overlap. This can cause a shift in the measured η of the jet, and therefore affect the angular distribution. The effect on the shape of the distribution due to removing those events in which either of the leading two jets were split or merged is, on average, 2%.

- **Overall energy scale:** The error on the overall energy scale correction described in Chapter 5 does not affect the shape of the distribution because a

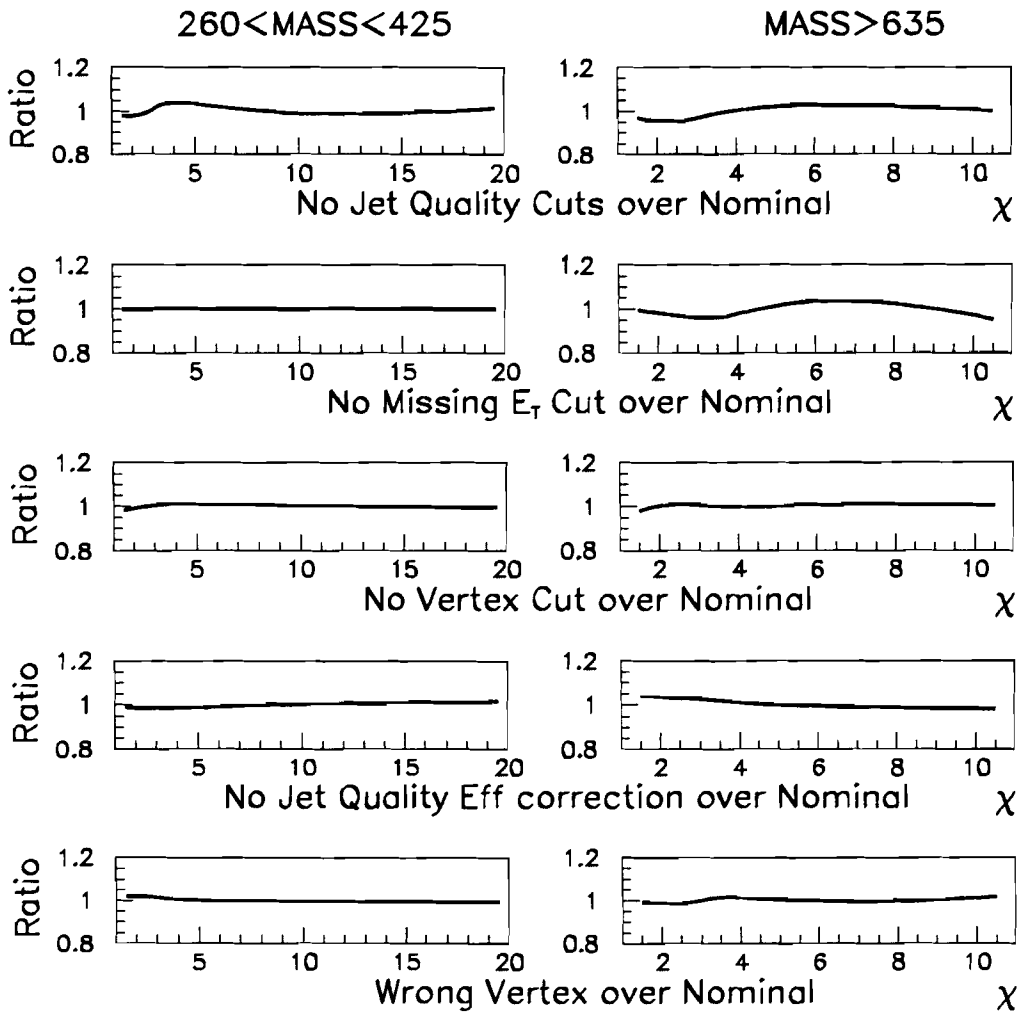

Figure 6.5: Ratios of parameterized curves showing effects of event selection requirements and corrections for two of the four mass ranges.

shift in the overall energy scale shifts the entire distribution in mass. The angular distribution changes very slowly with mass, so a small shift would not cause a significant change in the shape. The effect of the error of the overall energy scale correction on the shape of the angular distribution is, on average, 1%.

• **Jet resolution:** The resolution of the measurement of a jet's energy can also affect the angular distribution. The effect of resolution was determined by looking at the difference between the smeared and unsmeared theory calculations, using the resolutions described in Chapter 5. The effect of resolution on the shape of the angular distribution is, on average, 2%.

• η **bias:** An η bias due to our jet reconstruction algorithm was studied by comparing reconstructed Herwig jets to particle level jets. A correction based on this study [23] was applied to the data and the 'corrected' angular distribution was compared to the uncorrected distribution. The difference was, on average, 1%.

Figure 6.6 show the resulting ratios of the systematic studies for jet splitting and merging, the overall jet energy scale, the jet resolution, and the jet η bias.

6.3.4 Systematic Error Due to a Residual η Dependence of the Energy Scale

Measurements of the dijet angular distributions are dependent primarily on the η positions of the leading two jets, so the systematic variables which strongly affect the shapes of the dijet angular distributions are those which are η dependent. The final systematic variable studied was a residual η dependence of the energy scale factor. This section discusses how a residual η dependence of the energy scale could affect the shape of a dijet angular distribution, the determination of the η dependence, and the determination of the systematic error associated with the residual η dependence.

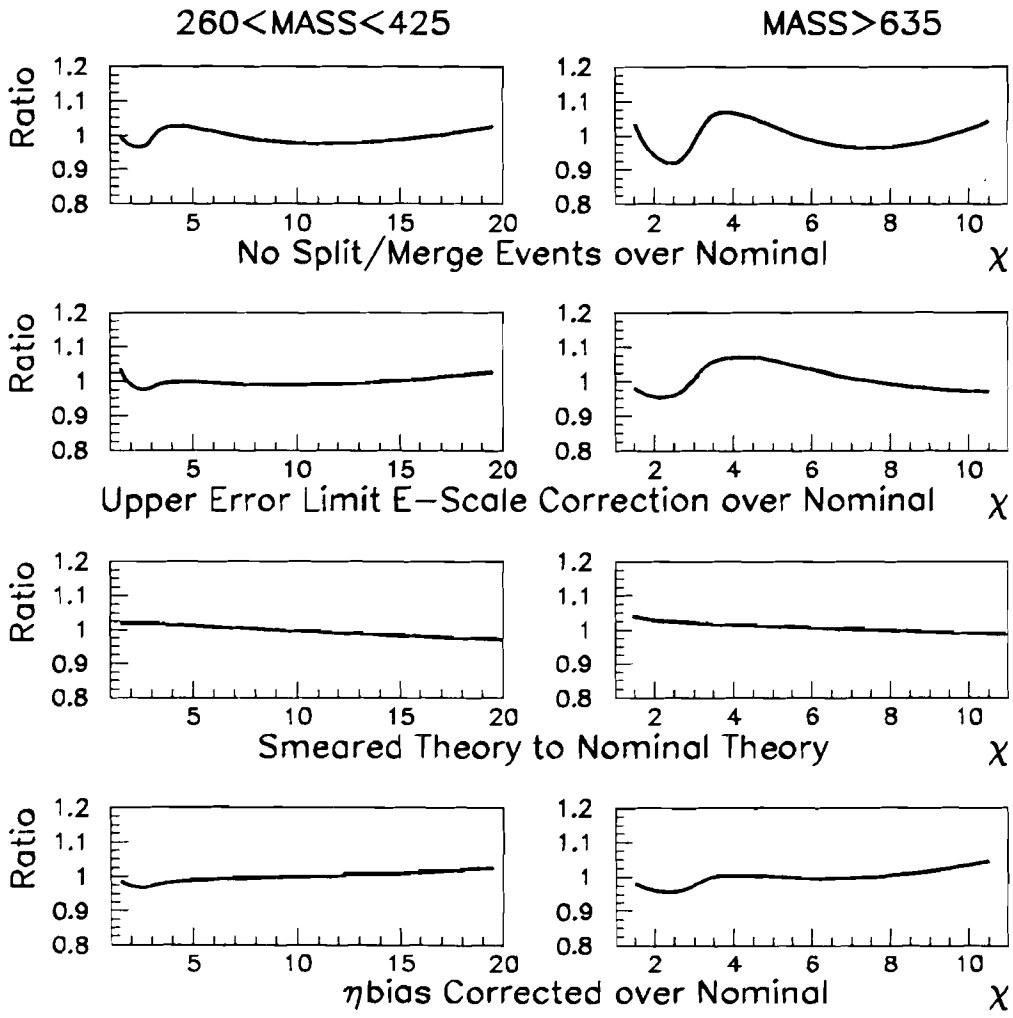

Figure 6.6: Ratios of parameterized curves showing effects of jet measurement accuracy.

The Systematic Effect of a Residual η Dependence of the Energy Scale

The energy scale factor affects the shape of an angular distribution through the choice of mass bin. Recall that the energy scale correction is the proportionality constant which converts the energy measured in the sampling calorimeter to the true energy. An error in the overall energy scale does not cause a significant error in the shape of the angular distribution because every region of χ is shifted the same amount in mass, and any difference in cross section is taken into account by the normalization of the distribution. A small shift in mass will not cause a significant change in the shape of the angular distribution. But, if there is a residual η dependence in the energy scale factor which is not accounted for in the energy scale correction, a significant error in the shape of an angular distribution would be introduced. As an example, consider two dijet events of the same mass. For the first dijet pair, both jets are in the central region ($|\eta| < 1$) and the pair has a χ of 2. For the second pair, both jets are in the forward region ($|\eta| > 1$) and the pair has a χ of 15. If the energy scale correction converts the energies of the jet pair in the central region to the true energies, then the measured mass of the pair will be the true mass. If the energy scale correction does not convert the energies of the jet pair in the forward region to the true energies, but to lower energies, then the measured mass of the pair will be lower than the true mass.

The cross section of dijet events drops rapidly with increasing dijet mass. The mass bin is selected according to the measured mass; thus, for events in the forward region with a higher true mass than was measured, $\frac{d\sigma}{d\chi}$ for the selected mass range will be too low. Therefore, fewer events will be measured in the χ region which corresponds to forward jets. For events in the central region with a correctly measured mass, $\frac{d\sigma}{d\chi}$ for the selected mass range will be the true cross section and the correct number of events will be measured in the χ region which corresponds

to central jets. A small error in the energy scale correction can cause a large shift in the dijet mass cross section, and hence a large error in an angular distribution measurement.

The Determination of the Residual η Dependence of the Energy Scale

In order to determine the residual η dependence of the energy scale, the principle of dijet balancing was used. As previously described in Chapter 5, the E_T's of the jets in a dijet event must vector sum to zero. This section describes the determination of the residual η dependence of the energy scale through measuring the dijet asymmetry, the photon-jet response factor, the E_T dependence of the response factor, the dijet response factor, and the resolution dependence of the dijet response factor.

•**Dijet asymmetry:** As a preliminary step, all E_T values were corrected using the standard DØ correction factors. Then, the asymmetry of the E_T's of a dijet pair was measured as a function of the η of a probe jet while the other jet remained central ($|\eta| < 0.5$). The asymmetry is defined as:

$$A_{JJ} = \frac{2(E_{Tcentral} - E_{Tprobe})}{(E_{Tcentral} + E_{Tprobe})} \tag{6.4}$$

Each event used to measure the asymmetry was required to have two and only two jets with an E_T greater than 8 GeV; the E_T of the leading jet was required to be greater than the corrected E_T limit in order to remove any trigger bias; and one jet in the event was required to have a central η ($|\eta| < 0.5$). The asymmetry measured as a function of the η of the probe jet showed a significant η dependence. It was thus determined that there was a residual η dependence in the energy scale.

•**The response factor for photon-jet events:** In order to measure the residual η dependence of the energy scale, the corrected calorimeter response was

measured in a similar manner to the R_{had} of the energy scale correction described in Chapter 5. The response was measured versus the η of the probe jet rather than the energy in order to measure the η dependence of the response relative to the response in the central η region. A photon-jet sample was used to measure the response, in which the photon was required to be central ($|\eta| < 0.5$) and have an E_T greater than the lowest E_T threshold used in this analysis, 55 GeV. The response was measured using the missing E_T projection fraction, MPF, which is defined by the following formula.

$$MPF = -1.0 \times \frac{\vec{\not{E}}_T \bullet \hat{n}_\gamma}{E_{T\gamma}} \tag{6.5}$$

For historical reasons, the response R_{had} was not measured to determine the residual η dependence of the energy scale. A 'response factor' R_η was measured. The response R_{had} is defined in Chapter 5 by the following formula.

$$R_{had} = 1 + \frac{\vec{\not{E}}_T \bullet \hat{n}_\gamma}{E_{T\gamma}} \tag{6.6}$$

The response correction to the E_T of a jet would be:

$$E_T = \frac{E_{Tmeasured}}{R_{had}} = \frac{E_{Tmeasured}}{1 + \frac{\vec{\not{E}}_T \bullet \hat{n}_\gamma}{E_{T\gamma}}} \tag{6.7}$$

For a small MPF, $\frac{\vec{\not{E}}_T \bullet \hat{n}_\gamma}{E_{T\gamma}} \ll 1$, the response correction can be approximated, through a Taylor expansion, as:

$$\frac{E_{Tmeasured}}{R_{had}} = \frac{E_{Tmeasured}}{1 + \frac{\vec{\not{E}}_T \bullet \hat{n}_\gamma}{E_{T\gamma}}} \approx E_{Tmeasured}(1 - \frac{\vec{\not{E}}_T \bullet \hat{n}_\gamma}{E_{T\gamma}}) = E_T R_\eta \tag{6.8}$$

We define the response factor as:

$$R_\eta = 1 - \frac{\vec{\not{E}}_T \bullet \hat{n}_\gamma}{E_{T\gamma}} \tag{6.9}$$

R_η was measured as a function of η using a sample of energy corrected photons and jets. A significant residual η dependence of the energy scale was found and a correction was determined to calculate the final E_T of a jet as a function of η. The correction is described by the following formula.

$$E_{T\,final} = E_{T measured} R_\eta \tag{6.10}$$

The photon-jet response factor is shown in Figure 6.7. When the photon jet response factor was applied as a correction to the jet data sample, the η dependence of the dijet asymmetry was removed for the data from the trigger which corresponded to the 55 GeV E_T threshold. But, an η dependence of the dijet asymmetry remained for the jet data samples corresponding to triggers with greater E_T thresholds. This was evidence that the response factor R_η was dependent on the E_T of the jets.

•**The E_T dependence of the response factor:** An E_T dependence of the response factor can be explained by the fact that as jet E_T increases the fraction of energy clustered in the center of the jet increases. So, for instance, if there is a defect in some portion of the calorimeter, the higher the jet E_T, the higher the fraction of the jet E_T affected by the defect, and the larger the overall effect. We were unable to confirm the E_T dependence of the response factor with a photon-jet sample because of the lack of photon data samples with E_T's above 100 GeV. To determine the E_T dependence we needed to measure the response factor with a dijet sample.

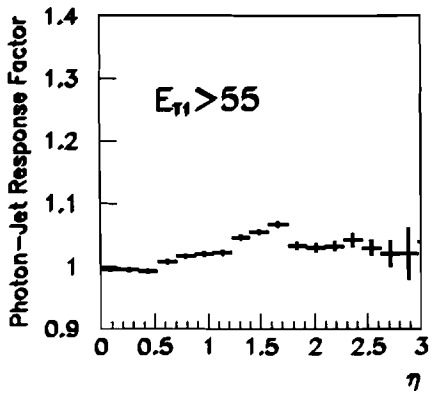

Figure 6.7: The photon-jet response factor versus η.

• **The response factor for dijet events:** To determine the E_T dependence of the response factor, R_η was measured using the dijet data samples for four E_T thresholds: 55, 90, 120, and 175 GeV. The requirements placed on the sample which was used to measure the response factor were: the event contained two and only two jets above 8 GeV; one of the jets was central ($|\eta| < 0.5$); and the leading jet was required to have an E_T greater than the corrected E_T threshold for its corresponding trigger. The response factor was measured as a function of η for each of four thresholds, and the result is shown in Figure 6.8

The response is commonly measured with photon-jet events, as opposed to dijet events, because photons have a better resolution and are better measured by the calorimeter. In order to check any differences between using a photon-jet sample and a dijet sample, the dijet response factor was compared to the photon-jet response factor for the 55 GeV threshold, and the results were the same for η's less than approximately 2, as shown in figure 6.9

•**The resolution dependence of the response factor:** When one looks at

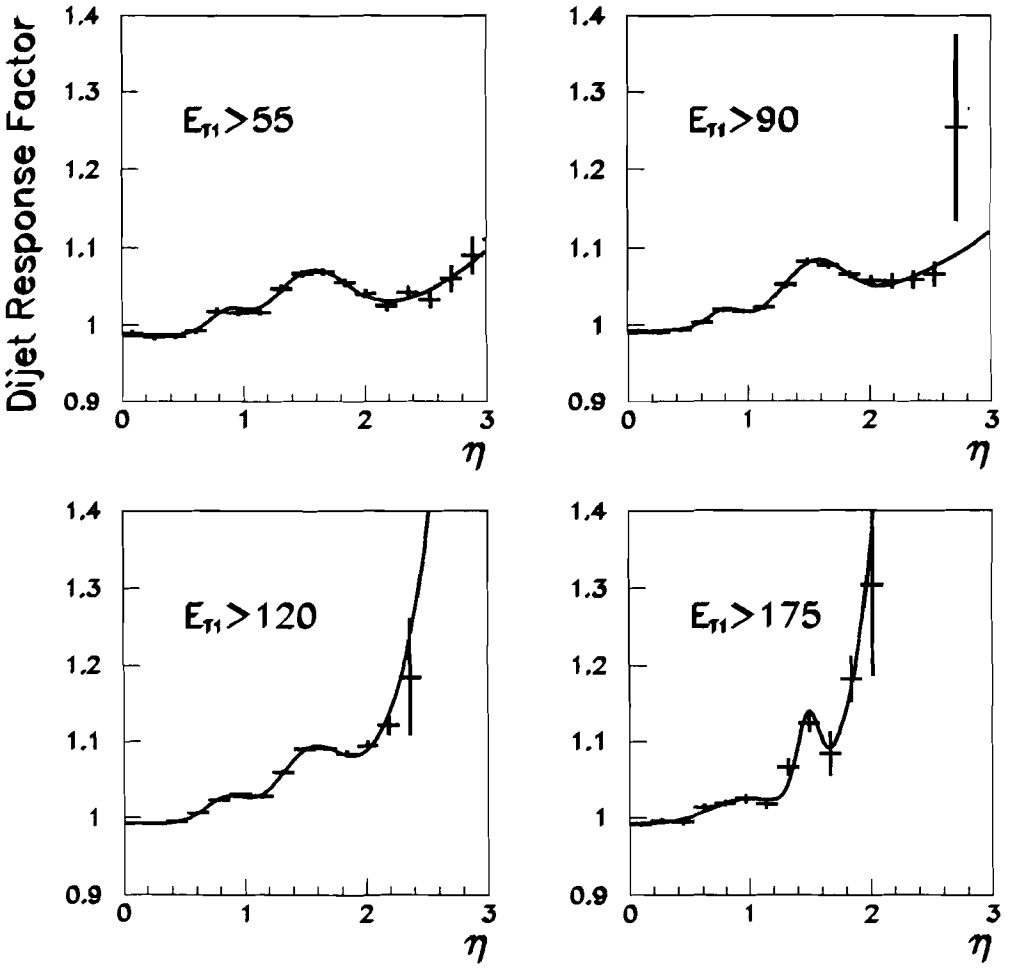

Figure 6.8: The dijet response factor versus η for four trigger samples.

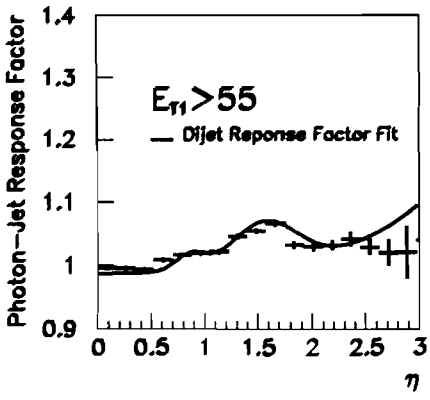

Figure 6.9: The response factor versus η for dijet(parameterized) and photon-jet(data points) samples.

the response factor measured beyond an η of approximately 2, the response factor appears to increase rapidly. This seems unphysical because the response of the central calorimeter versus the response in the end cap calorimeter has been studied and does not show such a large effect. The effect is due to resolution. The resolution of a jet is a function of the jet's energy. The resolution is primarily dependent on the sampling term, which can be approximated as $\sigma_E \approx 0.8\sqrt{E}$. As an example, if we require a jet with 120 GeV in E_T, for a jet at an η of 0, the $\sigma_E \approx 9$ GeV. This corresponds to a $\sigma_{E_T} \approx 9$ GeV. For a jet at an η of 2, a jet with 120 GeV in E_T has 450 GeV in energy. This corresponds to a $\sigma_E \approx 17$ GeV, which corresponds to $\sigma_{E_T} \approx 4$ GeV. As a function of E_T the resolution is wider in the central region than in the forward region. As the probe jet goes forward in η, the energy increases. As a jet goes forward, it rapidly approaches the kinematic limit imposed by the center-of-mass energy of the Tevatron. Eventually, the jet reaches an η at which the probability of a jet pair with the required E_T, say 120 GeV, is less likely to occur than a jet pair with 90 GeV in E_T in which a central jet fluctuated up to 120

GeV and passed our minimum E_T requirement. The increase in the response factor is due to this resolution effect. This was qualitatively confirmed by measuring the dijet asymmetry ($\frac{2\times(E_{T1}-E_{T2})}{(E_{T1}+E_{T2})}$) versus η using leading-order JETRAD, for smeared and unsmeared data, as shown in Figure 6.10.

Another concern was that the resolution was responsible for the E_T dependence of the response factor measurement. We looked at leading-order JETRAD with smearing for each of our different thresholds. At an η of 1.5, where the large η dependence of the response factor occurs, the effect of smearing on the monte carlo is the same regardless of the E_T threshold applied. So, the E_T dependence of the response factor measurement is unlikely to be from resolution effects. To deal with the resolution effect for jets around an η of 2 and above, we applied a mass cut to the data used to measure the response factor. The mass cut is the cut we use in our analysis which corresponds to the minimum E_T for each trigger. The mass cut removes these events in which one jet from a low E_T pair fluctuates to pass our minimum E_T cut, because it essentially requires that the product of the 2 E_T's be greater than a threshold. The response factor with an applied mass cut was measured and parameterized, as shown in Figure 6.11. This parameterization was compared to the parameterization of the response factor without a mass cut applied. In the regions below an η of 2, the two curves agree fairly well, as shown in Figure 6.12.

Determination of the Systematic Error

The parameterization for the response factor measurement with the applied mass cut was used to correct the data sample. Since the cause of the η dependence of the energy scale is not yet known, a conservative error is placed on the response factor correction as the difference between a correction for a trigger and the correction for

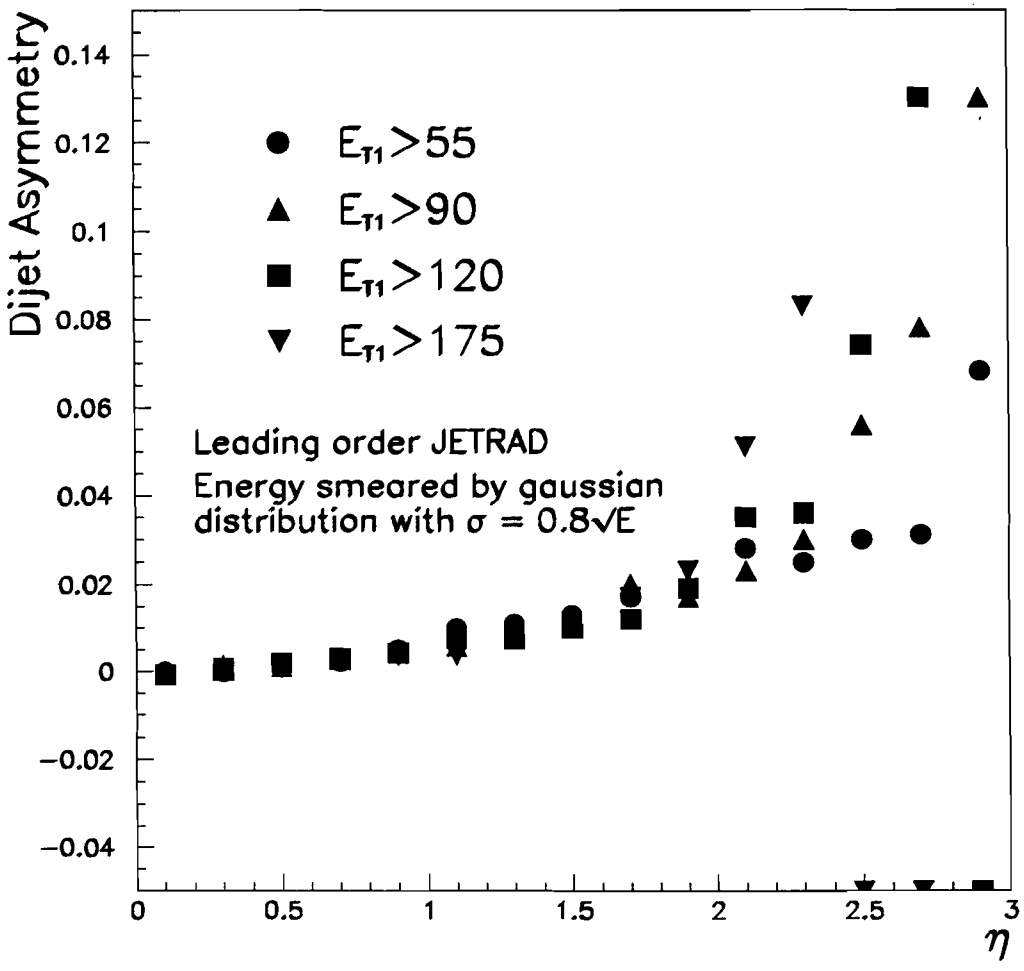

Figure 6.10: The effect of smearing on the dijet asymmetry for four triggers. Shown are the results of Monte Carlo studies.

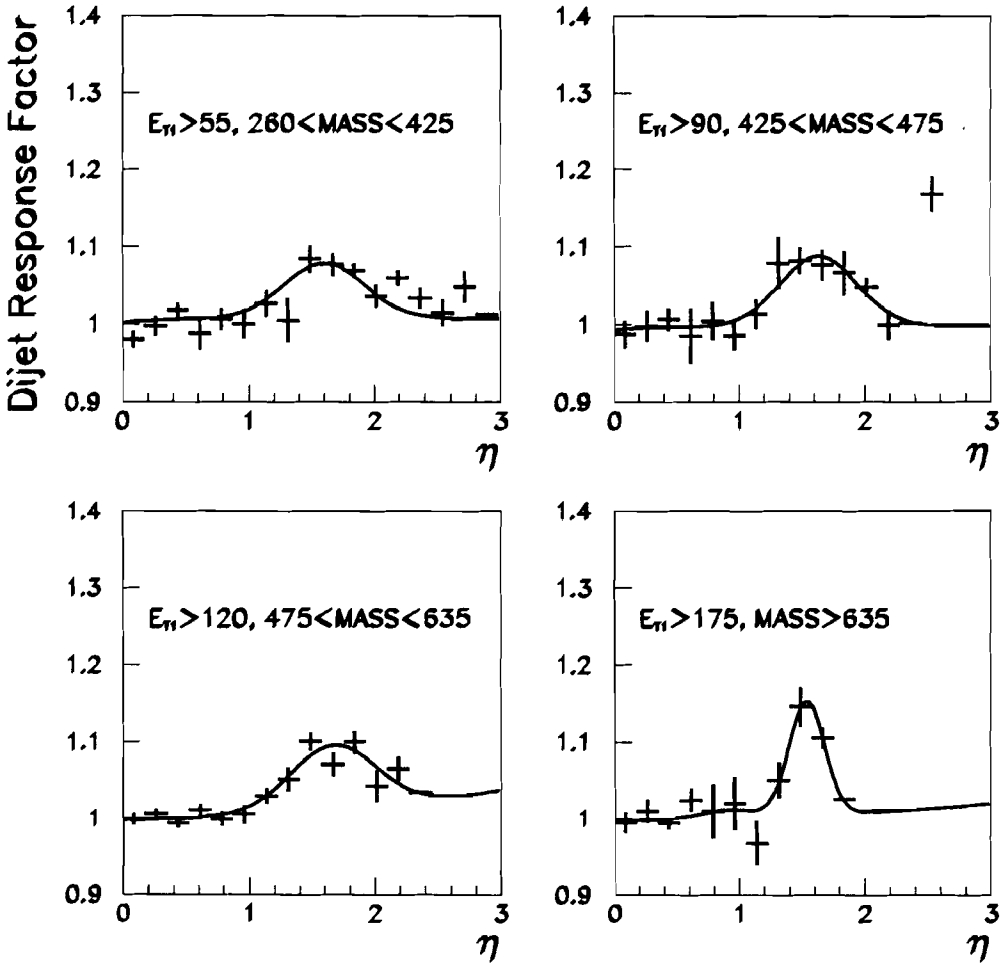

Figure 6.11: The dijet response factor versus η for four trigger samples with an applied mass cut.

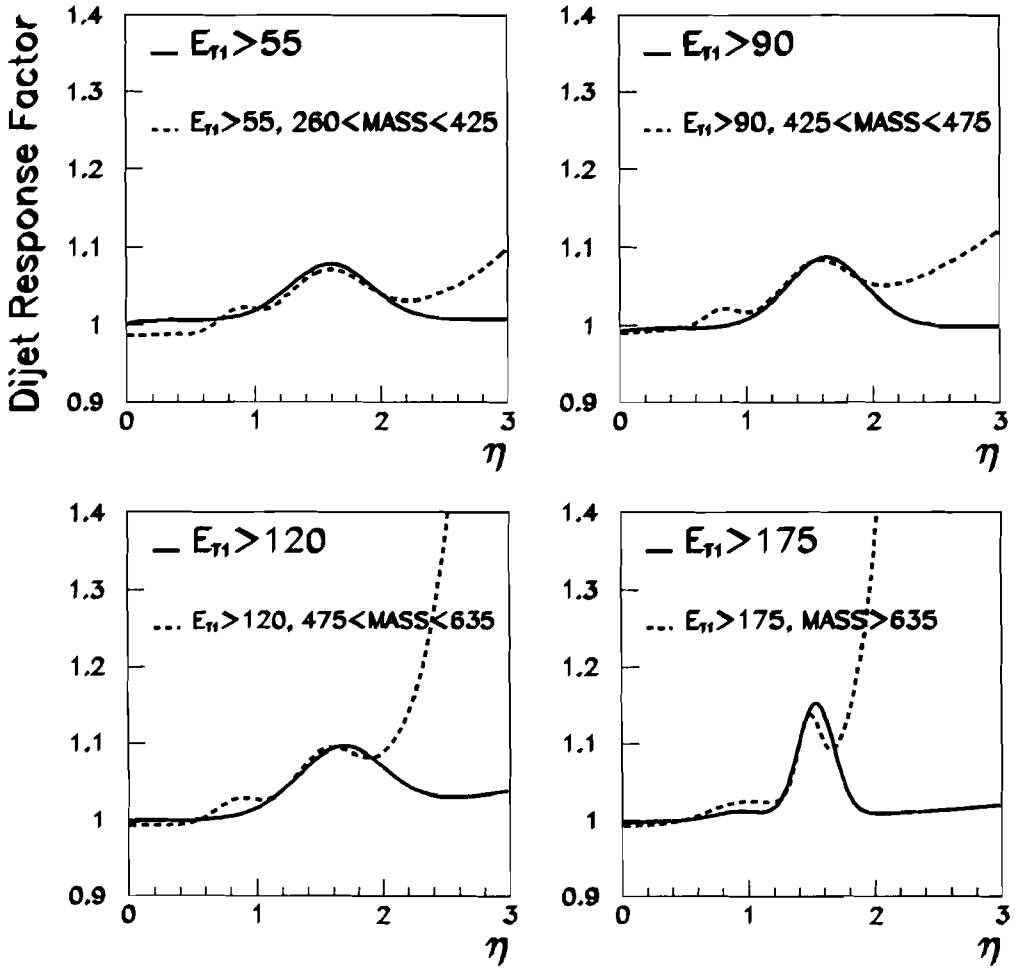

Figure 6.12: A comparison of the parameterized dijet response factor versus η with and without an applied mass cut.

the lowest trigger using the photon-jet data. The error on the angular distribution due to the response factor correction error is determined by the angular distribution measured with the photon-jet correction over the angular distribution measured with the nominal correction for that mass bin and is, on average, 3%. We also place a small error for the difference between the angular distribution corrected by the response factor measured without an applied mass cut, for $\eta < 2$, and the angular distribution corrected with the MPF measured with the mass cut which is, on average, 1%. Figure 6.13 show the resulting ratio of the angular distribution calculated by using the photon-jet response factor correction over the nominal distribution which uses the dijet response factor correction.

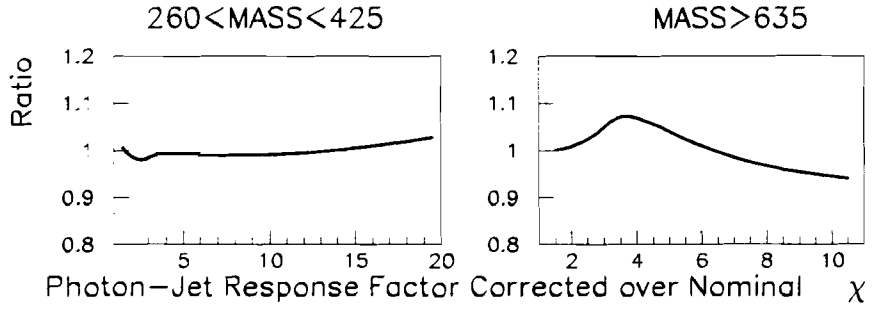

Figure 6.13: Ratios of parameterized curves showing effects of the photon-jet corrected angular distributions over nominal distributions.

6.4 Interpretations of a Shape Comparison

This analysis measures a normalized distribution $\frac{1}{N}\frac{dN}{d\chi}$ for a region in invariant mass and η_{boost}. To determine how well the shapes of two normalized distributions agree, one must take into account the comparison of each point in the distribution. Any disagreement between a measured and a theoretical point in the distribution

can not be interpreted solely as a departure in that particular region in χ, but must be considered as a possible shift in the full distribution. The error on the measured distribution comes from two sources: statistical error, and systematic error. The statistical error is caused by the fact that the measured distribution is extracted from a finite number of events. The statistical errors can explain small deviations in the measured distribution from a smooth curve. The systematic error can explain overall shifts in the distribution, as well as errors in individual regions in χ.

Consider an exaggerated example of systematic error, in which the angular distributions were not corrected for a residual η dependence of the energy scale. Figure 6.14 shows a comparison of a nominal angular distribution and an angular distribution which has not been corrected for a residual η dependence of the energy scale. The effect of this error is a decrease in the measured number of events for larger values of χ. The normalization constant $\frac{1}{N}$ is one over the sum of the total number of events in the distribution. For the uncorrected distribution, the normalization constant is larger than for the nominal distribution since the total number of events is smaller. When the uncorrected distribution is then normalized, the lower values of χ shift up in relation to the nominal distribution, while the larger values of χ appear to agree. Any systematic error will affect the distribution in this manner.

A systematic error band can be interpreted as the effective range that the shape of the distribution can shift, given that the final distribution is normalized. If an error was introduced, the points in the distribution would shift by a series of positive and negative values that would form a curve as a function of χ which would fully reside within the systematic error band centered about zero. For the distribution to remain normalized, the area between this curve and the centerline at zero must sum to zero, given that the area above the curve is defined as positive,

and the area below the curve is defined as negative. Using the previous exaggerated example, not correcting for a residual η dependence of the energy scale would result in a shift in the distribution described by a curve shown in Figure 6.15.

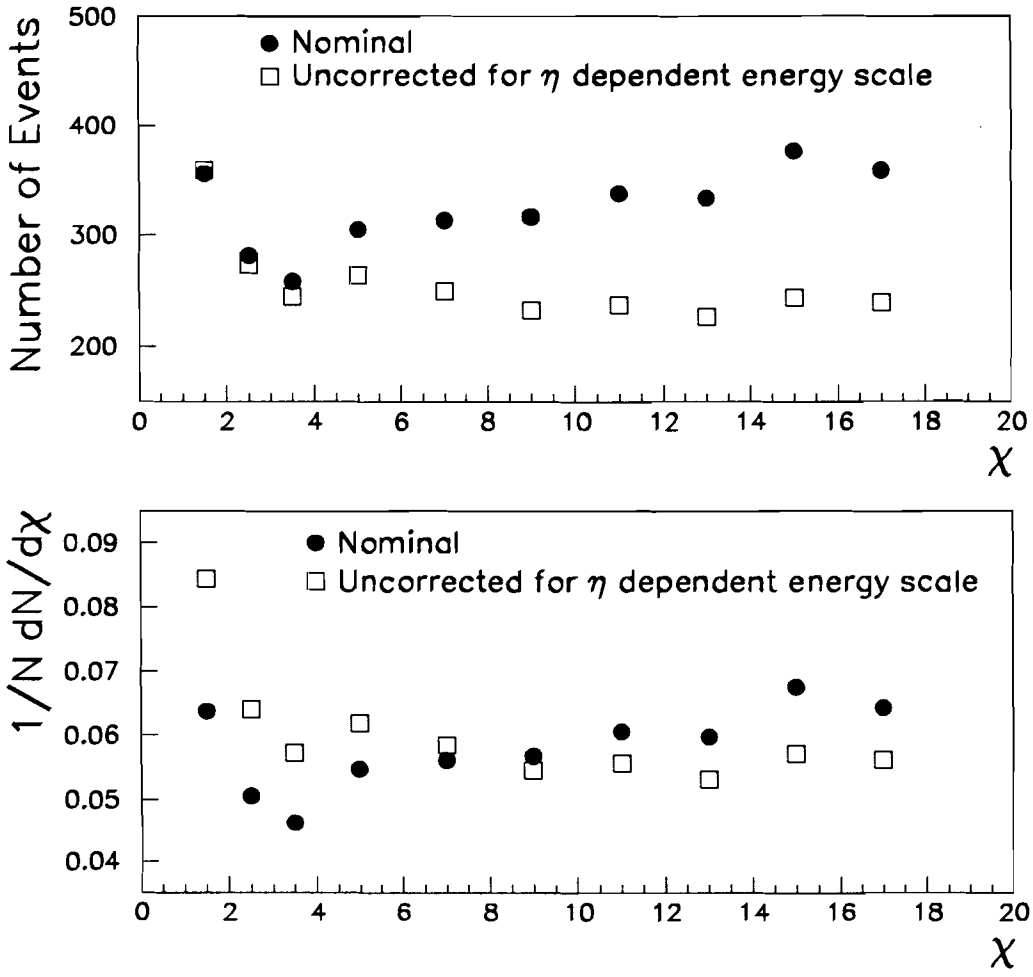

Figure 6.14: Shown is a comparison of a nominal angular distribution and an angular distribution which has not been corrected for a residual η dependence of the energy scale.

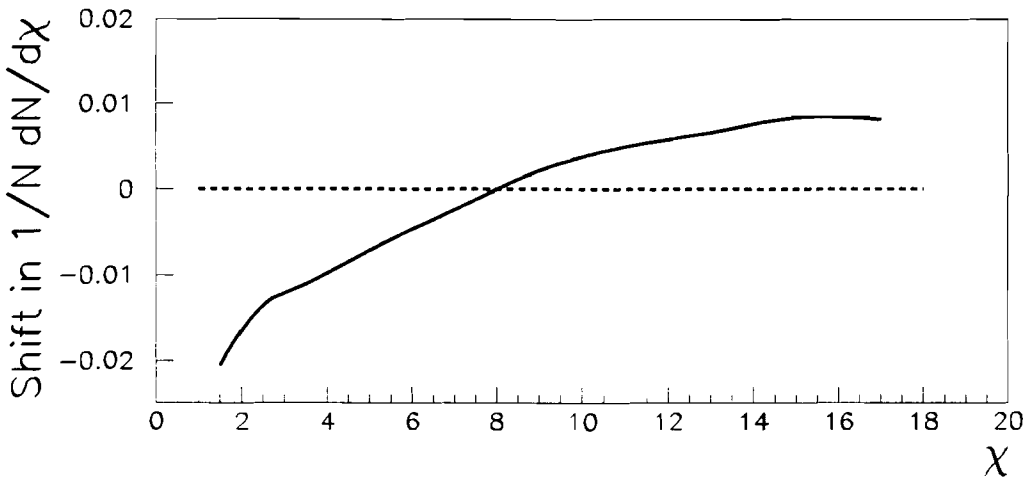

Figure 6.15: Shown is the shift in an angular distribution caused by a residual η dependence of the energy scale. In order for the distribution to remain normalized the area between the curve and the centerline is the same above and below zero.

Chapter 7

Results

The goal of this analysis is to compare the shapes of the observed dijet angular distributions to those predicted by perturbative QCD. Such a comparison is important because it measures how well predictions of perturbative QCD describe the distributions produced by interactions of partons. This chapter will discuss the comparison of the measurements of the dijet angular distributions to the leading-order and next-to-leading-order predictions of QCD.

7.1 Comparison to Theoretical Predictions

The dijet angular distributions were compared to predictions of perturbative QCD in four mass bins. The predictions were generated using JETRAD with the CTEQ3M parton distribution function. Renormalization scales were set to E_T and $\frac{E_T}{2}$ of the leading jet in an event. The E_T's and η's of jets in the generated events were smeared by the resolutions described in Chapter 5 for comparison to the data. As discussed in Chapter 6, the effect of resolution on the shape of the dijet angular distribution is small.

The predicted shapes depend on the nature of higher-order corrections. The shapes predicted by leading-order QCD are significantly different than those predicted by next-to-leading-order QCD. A comparison of the observed dijet angular distribution in the mass range of $260 < M_{JJ} < 425$ GeV/c^2 to predictions of QCD for leading-order and next-to-leading-order terms generated with a renormalization scale of E_T are shown in Fig. 7.1. Comparisons for the mass ranges of $475 < M_{JJ} < 635$ GeV/c^2, $M_{JJ} > 550$ GeV/c^2, and $M_{JJ} > 635$ GeV/c^2 are shown in Figs. 7.2, 7.3, and 7.4 respectively. The predictions of perturbative QCD are consistent with the data in all four mass bins, however, overall, the data agree somewhat better with the next-to-leading-order predictions.

A measure of the dependence of the predictions of perturbative QCD on higher-order terms is given by the dependence of the theory on the choice of renormalization scale. The shapes of the next-to-leading-order predictions of the dijet angular distribution show a dependence on the choice of renormalization scale that is on the order of a few percent. A comparison of the dijet angular distribution in the mass range of $260 < M_{JJ} < 425$ GeV/c^2 with predictions of QCD for next-to-leading-order generated with a renormalization scale of $\mu = E_T$ and $\mu = \frac{E_T}{2}$ is shown in Fig. 7.5. Comparisons for the mass ranges of $475 < M_{JJ} < 635$ GeV/c^2, $M_{JJ} > 550$ GeV/c^2, and $M_{JJ} > 635$ GeV/c^2 are shown in Figs. 7.6, 7.7, and 7.8, respectively. Within systematic uncertainty, the predictions of QCD for both renormalization scales agree with the data.

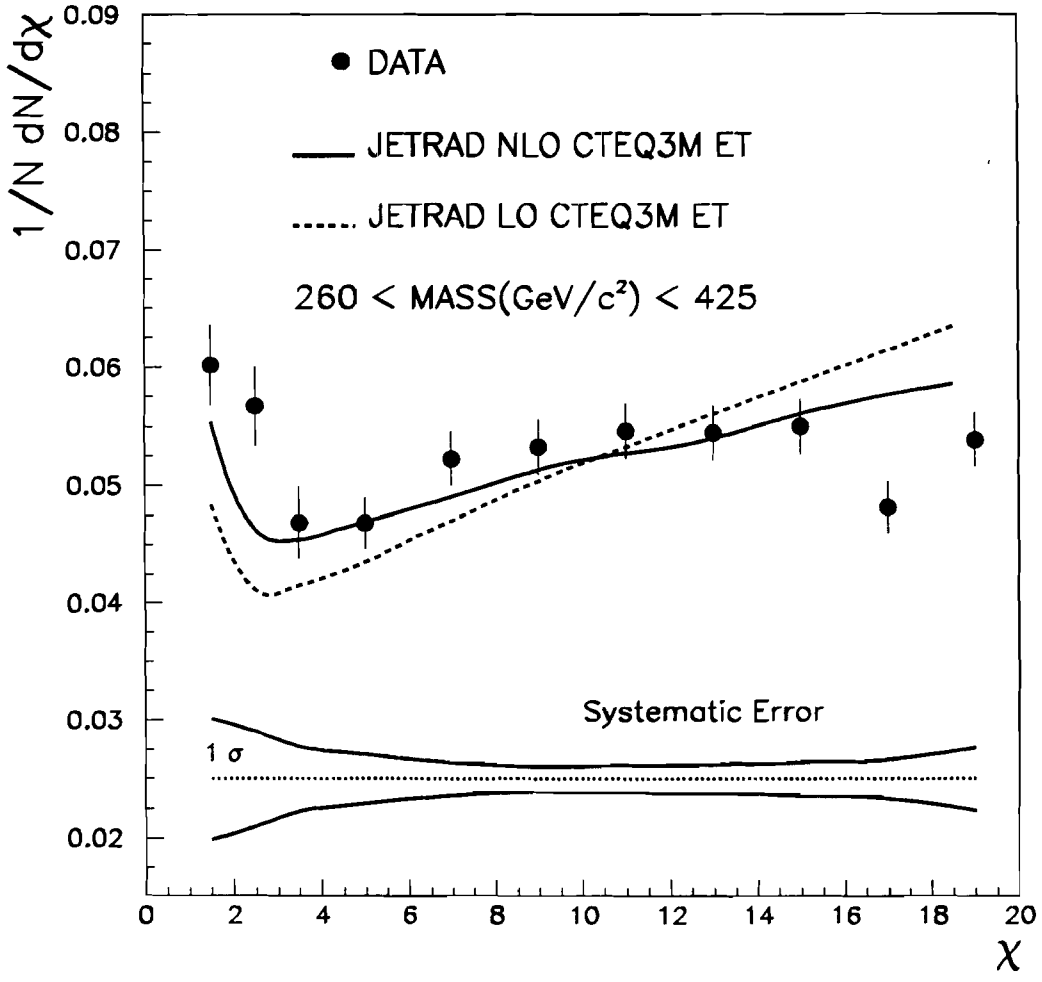

Figure 7.1: Shown is a comparison of the leading-order and next-to-leading-order predictions of QCD to measured data in a mass range of $260 < M_{JJ} < 425$ GeV/c^2. The renormalization scale used was the E_T of the leading jet in the event. The systematic error band is shown at the bottom. Small oscillations are due to statistical uncertainty.

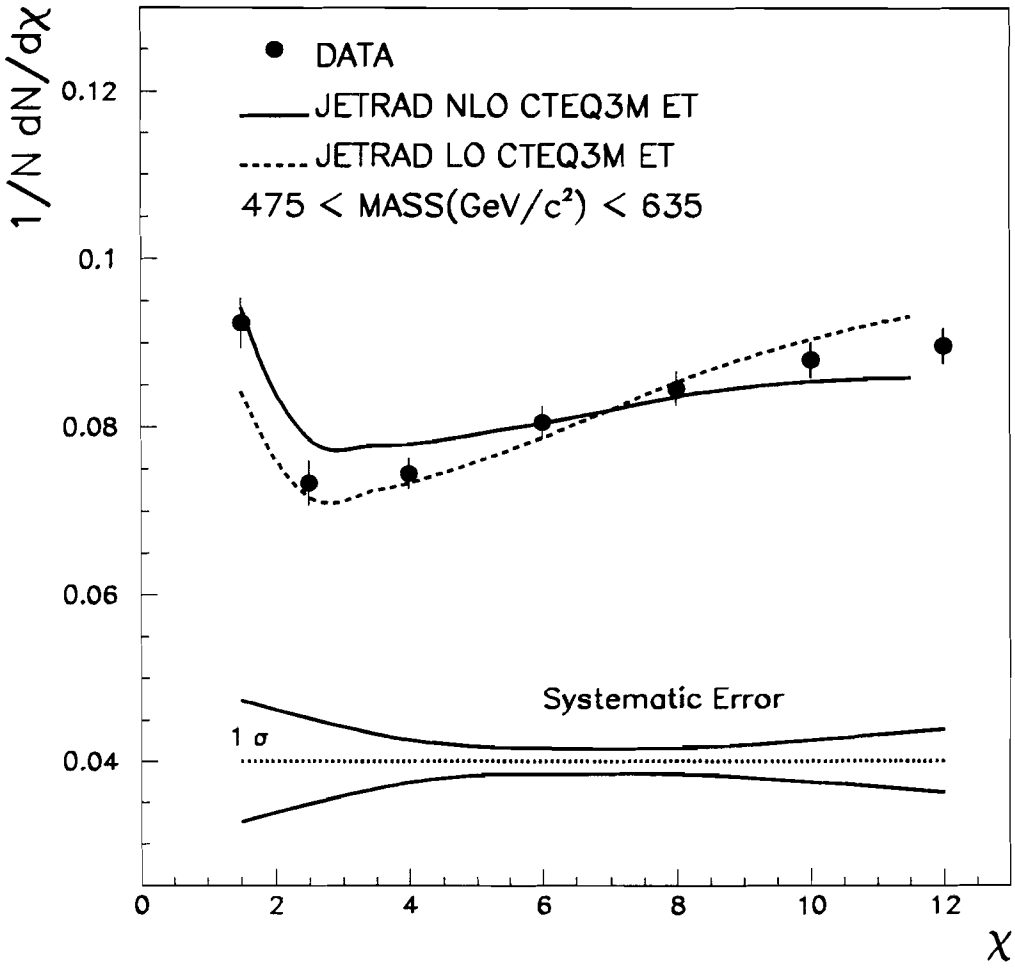

Figure 7.2: Shown is a comparison of the leading-order and next-to-leading-order predictions of QCD to measured data in a mass range of $475 < M_{JJ} < 635$ GeV/c^2. The renormalization scale used was the E_T of the leading jet in the event. The systematic error band is shown at the bottom. Small oscillations are due to statistical uncertainty.

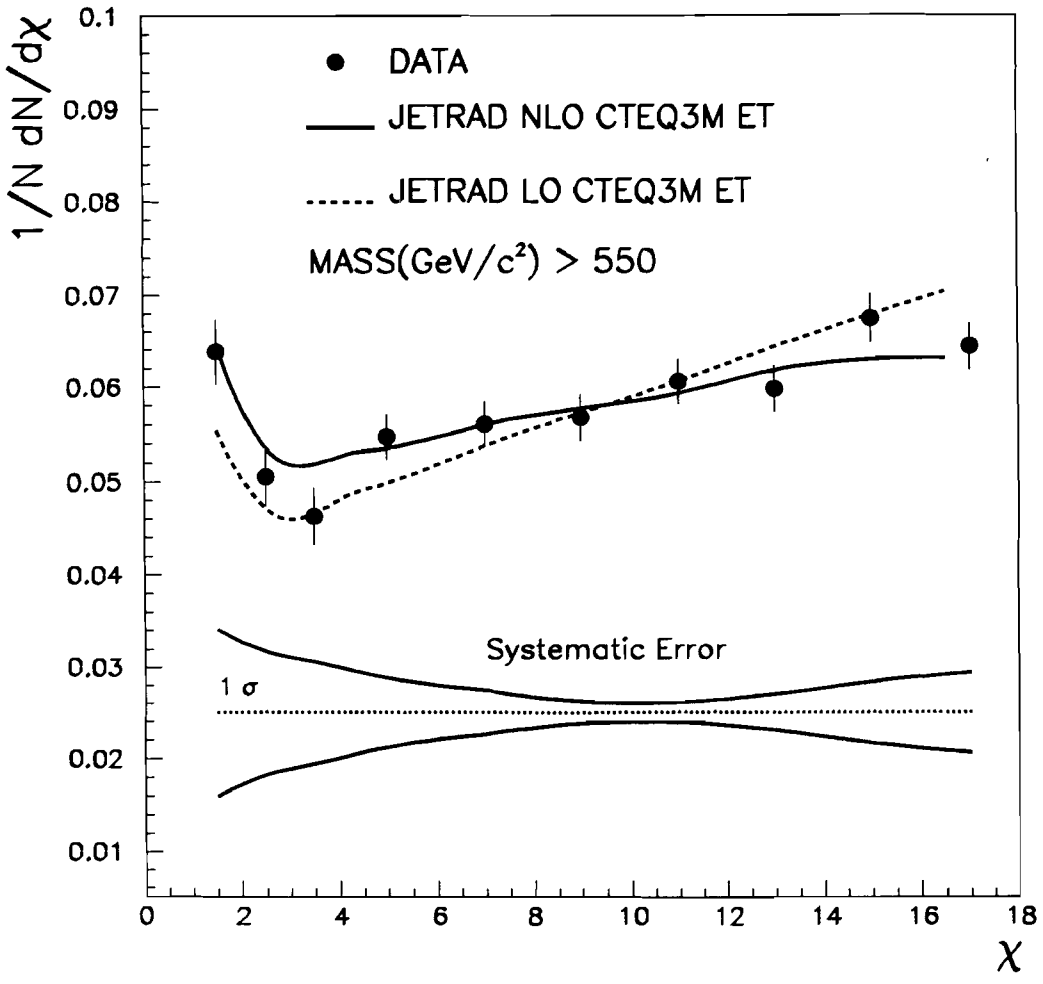

Figure 7.3: Shown is a comparison of the leading-order and next-to-leading-order predictions of QCD to measured data in a mass range of $M_{JJ} > 550$ GeV/c^2. The renormalization scale used was the E_T of the leading jet in the event. The systematic error band is shown at the bottom. Small oscillations are due to statistical uncertainty.

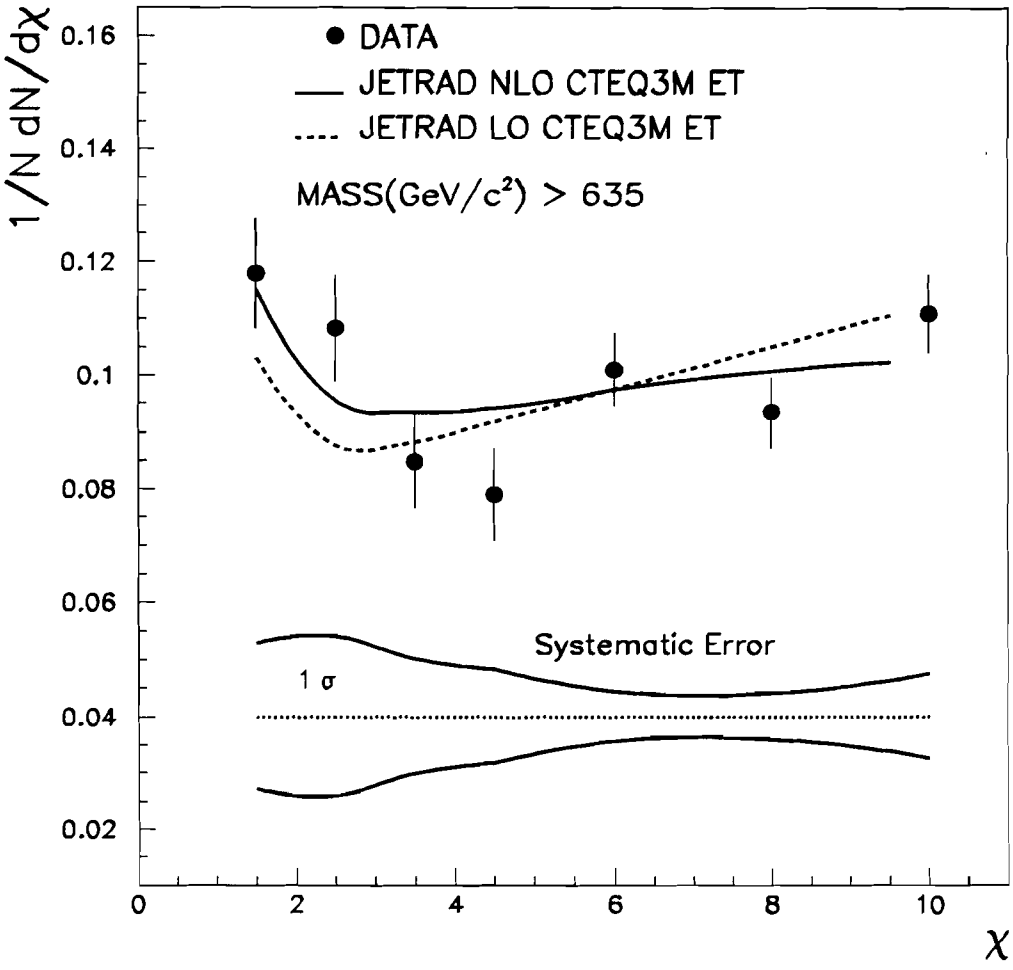

Figure 7.4: Shown is a comparison of the leading-order and next-to-leading-order predictions of QCD to measured data in a mass range of $M_{JJ} > 635$ GeV/c^2. The renormalization scale used was the E_T of the leading jet in the event. The systematic error band is shown at the bottom. Small oscillations are due to statistical uncertainty.

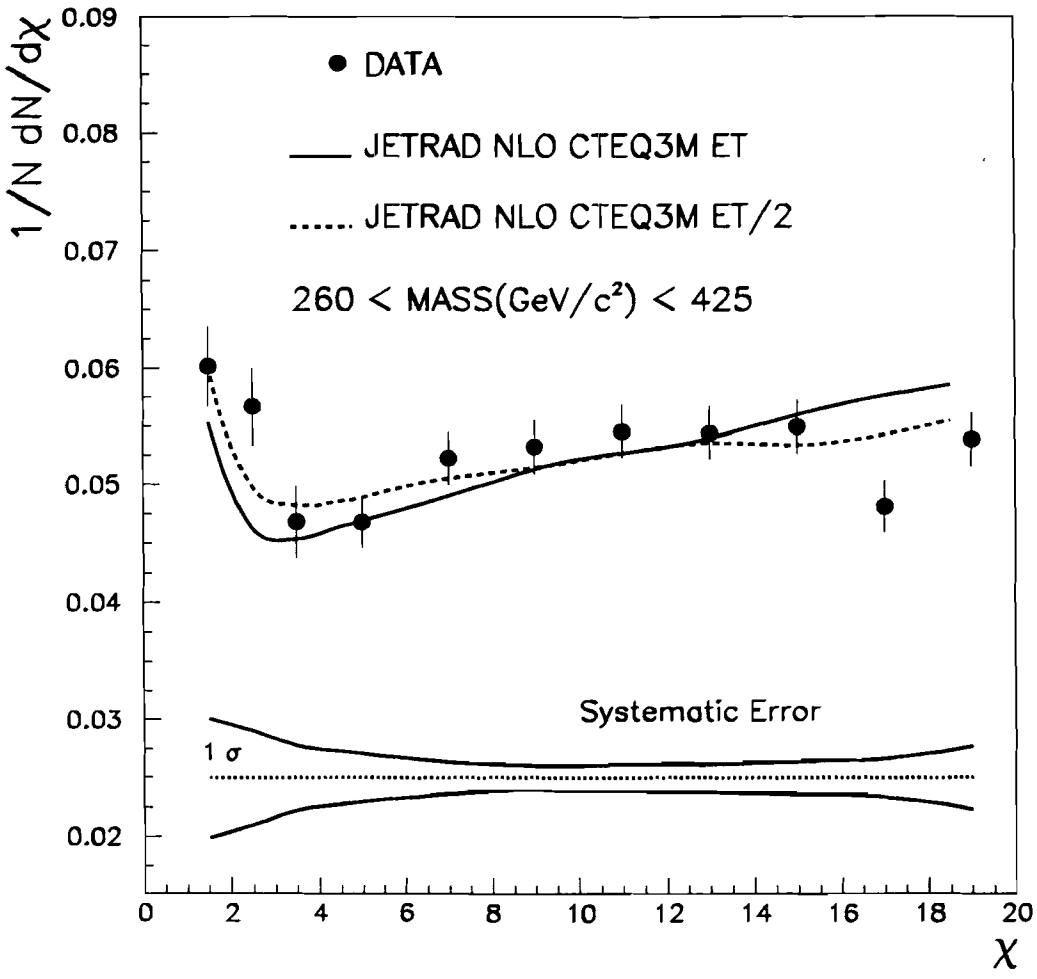

Figure 7.5: Shown is a comparison of the next-to-leading-order predictions of QCD generated with renormalization scales of the E_T and the $\frac{E_T}{2}$ of the leading jet in an event to measured data in a mass range of $260 < M_{JJ} < 425$ GeV/c^2. The systematic error band is shown at the bottom. Small oscillations are due to statistical uncertainty.

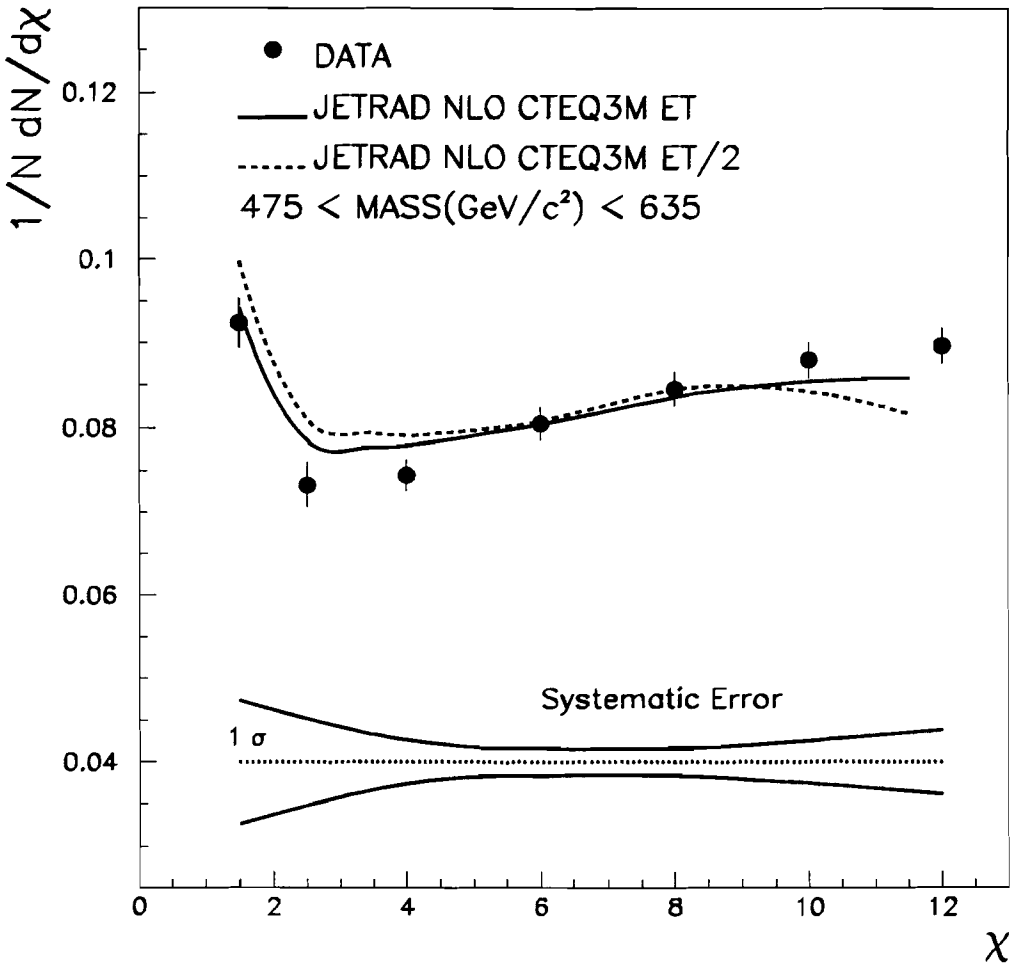

Figure 7.6: Shown is a comparison of the next-to-leading-order predictions of QCD generated with renormalization scales of the E_T and the $\frac{E_T}{2}$ of the leading jet in an event to measured data in a mass range of $475 < M_{JJ} < 635$ GeV/c^2. The systematic error band is shown at the bottom. Small oscillations are due to statistical uncertainty.

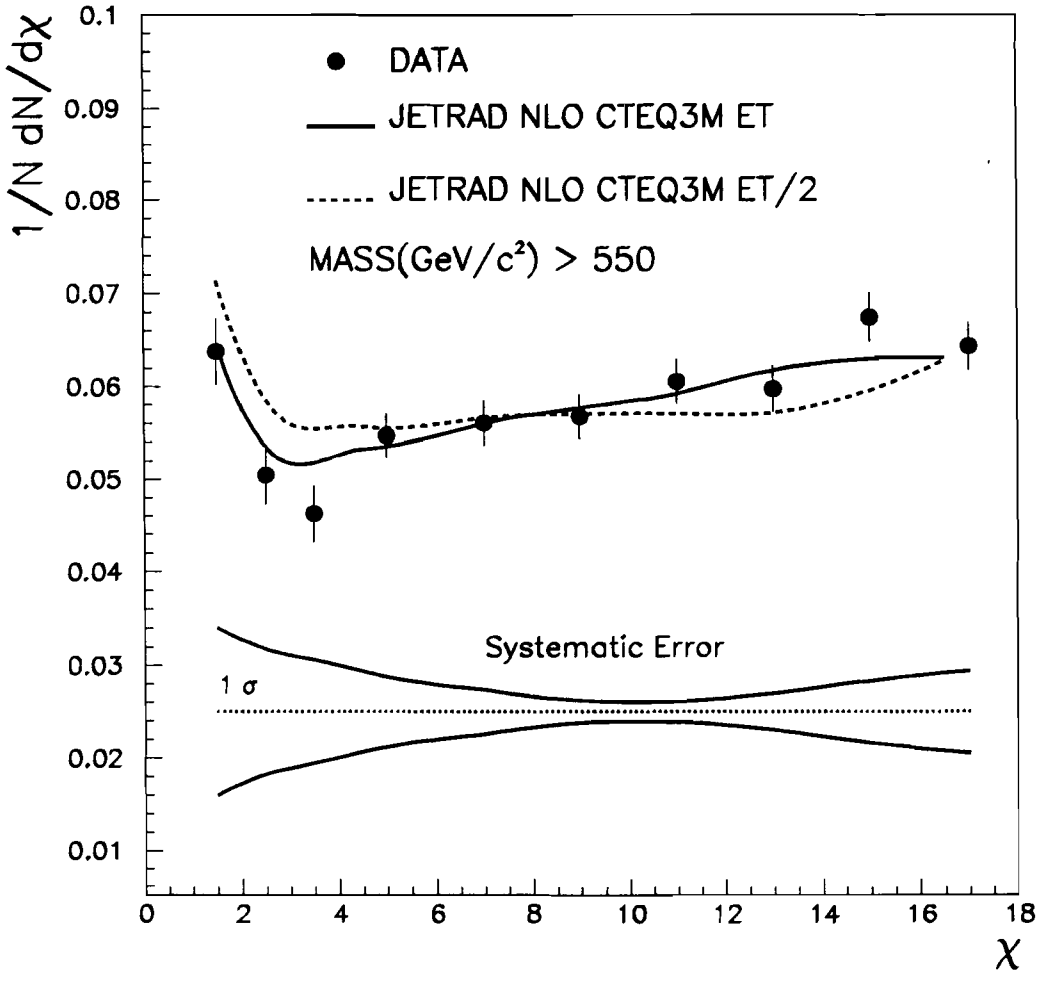

Figure 7.7: Shown is a comparison of the next-to-leading-order predictions of QCD generated with renormalization scales of the E_T and the $\frac{E_T}{2}$ of the leading jet in an event to measured data in a mass range of $M_{JJ} > 550$ GeV/c^2. The systematic error band is shown at the bottom. Small oscillations are due to statistical uncertainty.

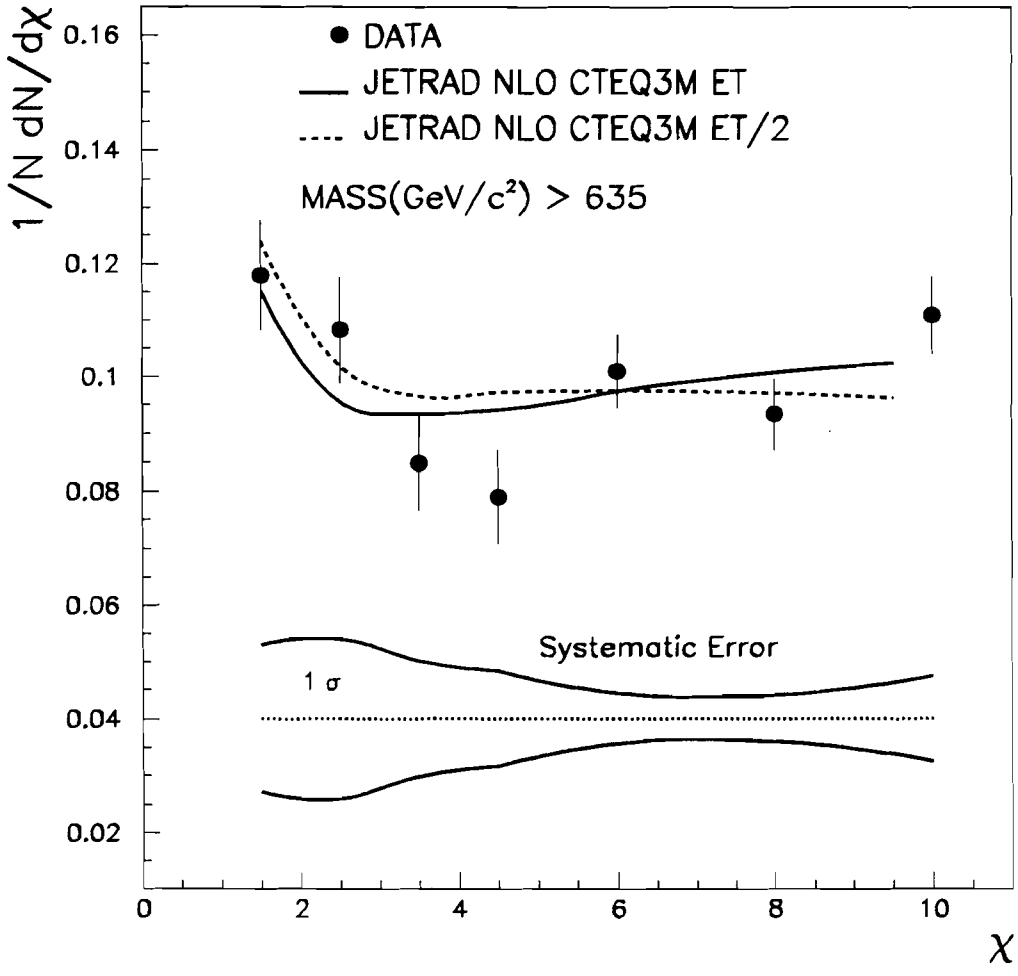

Figure 7.8: Shown is a comparison of the next-to-leading-order predictions of QCD generated with renormalization scales of the E_T and the $\frac{E_T}{2}$ of the leading jet in an event to measured data in a mass range of $M_{JJ} > 635$ GeV/c^2. The systematic error band is shown at the bottom. Small oscillations are due to statistical uncertainty.

Chapter 8

Quark Compositeness

Any observed departure from the predictions of QCD may indicate that quarks are composite states of more fundamental particles. In the mass region of $M_{JJ} > 550$ GeV/c^2, the shape of the dijet angular distribution is sensitive to quark compositeness at energy scales of $\Lambda_c \approx 1.0$ TeV. In this chapter, we will present a comparison of the measured dijet angular distributions to next-to-leading-order predictions of QCD that have an added term for quark compositeness, as described in Eq. 2.17 (refer to Chapter 2), and we will discuss the limit we obtain on the minimum value of Λ_c sustained by the data.

8.1 Comparison to Predictions of QCD Including Quark Compositeness

A comparison of the measured dijet angular distributions to the predictions of next-to-leading-order QCD with an added term for quark compositeness in the mass region of $M_{JJ} > 550$ GeV/c^2 is shown in Figure 8.1. The predictions were generated as described in Chapter 2 for values of Λ_c from ∞ to 1.0 TeV. The next-

to-leading-order predictions of QCD with a composite energy scale of $\Lambda_c = \infty$ show the best agreement with the data. We do not observe any significant discrepancies from the expectations of QCD.

8.2 Calculation of a Limit on Λ_c

We can use the data to place a limit on the energy scale Λ_c. We calculate a 95% CL lower limit as a function of Λ_c based on the probability that the angular distribution predicted by QCD (with an added contact term) is consistent with the measured angular distribution. The lower limit on Λ_c at a 95% confidence level is the value of Λ_c required to contain 95% of the integral of the probability density.

There are difficulties associated with calculating a limit based purely on the shape of the measured dijet angular distribution because of correlations of uncertainties between the points as a result of normalization. In order to minimize these difficulties, we chose to compare a ratio of the number of events observed in the region $1 \leq \chi < 6$, to the number of events found in the region $6 \leq \chi < 18$, which removes point-to-point correlations due to normalization. This ratio was calculated for the mass region $M_{JJ} > 550$ GeV/c^2 and had the value of $R_{data} = 0.37$. The uncertainty on the measured ratio was determined by adding the statistical and systematic errors in quadrature. The systematic error was determined by comparing the calculated ratio for the nominal distribution to the calculated ratio for the distribution associated with the error on the η dependence of the energy scale, the dominant error. Using the difference between the two ratios as the systematic error, the total error was estimated as $\Delta R_{data} = 0.03$.

The ratio R_{theory} was calculated for a series of theoretical predictions as a function of Λ_c. The statistical uncertainty of the ratio of the theoretical predictions is small and was ignored. There are uncertainties associated with the theoretical

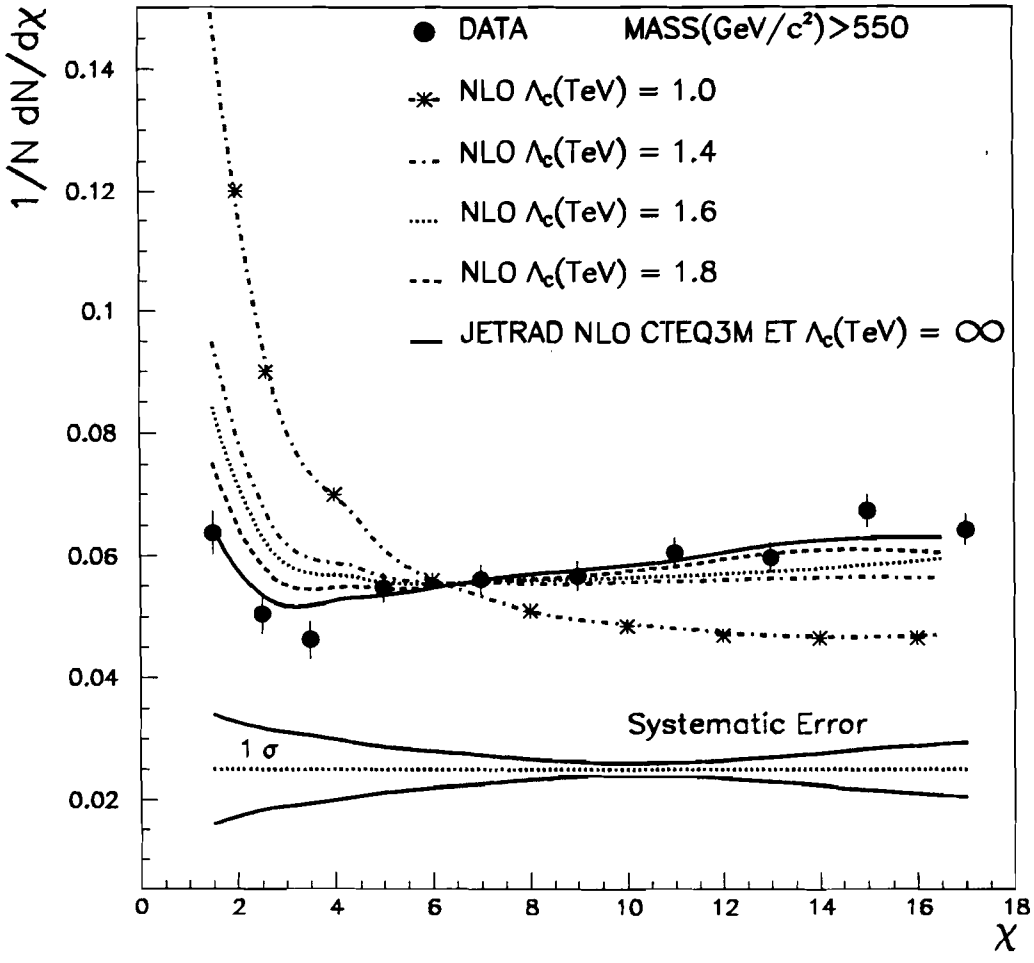

Figure 8.1: Shown is a comparison of data with the next-to-leading-order predictions of QCD with an added term for quark compositeness at energy scales Λ_c, in a mass range of $M_{JJ} > 550$ GeV/c^2. The systematic error band is shown at the bottom. Small oscillations are due to statistical uncertainty.

predictions due to the dependence of the distribution on the renormalization scale. In order to avoid the complications associated with including these uncertainties in the calculation of a limit, the predictions associated with each renormalization scale were treated as separate theoretical models. Since the next-to-leading-order QCD predictions generated with a renormalization scale of $\mu = E_T$ best modeled the data, R_{theory} was calculated from this set of predictions. The ratios corresponding to these theoretical predictions as a function of Λ_c is shown in Table 8.1

The limit on Λ_c was calculated in the following manner. Given a particular data set, the probability of a particular theoretical prediction can be determined using a Bayesian technique for setting confidence intervals [27]. Defining $P(A|BI)$ as the probability of event A given event B and I, where I has all relevant prior information in the problem, Bayes' Theorem states that

$$P(A|BI) = \frac{P(B|AI)P(A|I)}{P(B|I)} \tag{8.1}$$

The denominator $P(B|I)$ is determined by a normalization:

$$\sum_{allA} P(A|BI) = 1 \tag{8.2}$$

For continuous parameters, the normalization is the integral over the relevant parameters. $P(B|AI)$ is referred to as the likelihood. $P(A|I)$ is referred to as the prior probability. $P(A|BI)$ is referred to as the posterior probability.

The value of the theoretical ratio depends on the value of Λ_c, and so we will therefore determine the limit as a function of Λ_c. As discussed in Chapter 2, the effect of the added contact term for quark compositeness on the dijet angular distribution is approximately proportional to $\frac{1}{\Lambda_c^2}$. We will therefore determine the limit as a function of a more natural parameter γ which is defined as $\gamma = \frac{1}{\Lambda_c^2}$.

Table 8.1: The ratio of $\frac{N(1\leq\chi<6)}{N(6\leq\chi<18)}$ for the theoretical predictions of QCD generated with a renormalization scale of E_T with an added term for quark compositeness at various energy scales, Λ_c.

Λ_c (TeV)	R_{theory}
∞	0.385
10	0.386
5.0	0.388
3.0	0.389
2.5	0.397
2.4	0.399
2.3	0.402
2.2	0.401
2.1	0.404
2.0	0.413
1.95	0.414
1.9	0.415
1.85	0.418
1.8	0.423
1.75	0.426
1.7	0.433
1.65	0.439
1.6	0.460
1.55	0.453
1.5	0.480
1.4	0.501
1.0	0.757

The posterior probability we wish to determine is of the form:

$$P(\gamma|R_{data}I) = \frac{P(R_{data}|\gamma I)P(\gamma|I)}{\int_0^\infty P(R_{data}|\gamma I)P(\gamma|I)d\gamma} \tag{8.3}$$

The limit on γ, which translates to a limit on Λ_c, is determined in a series of steps. We first define the likelihood function and the prior probability. We then integrate the product of the likelihood function and the prior probability over a range in γ from 0 to ∞ in order to determine the normalization. Finally, the limit on γ is the value for which the integral of the normalized posterior probability from 0 (which corresponds to a $\Lambda_c = \infty$, or no compositeness) to γ is 0.95.

• **Definition of the likelihood function:** We assumed that, given the distribution of γ is a gaussian with a standard deviation equal to the error on R_{data}, $\Delta R_{data} = \sigma = 0.03$, the likelihood of measuring R_{data} can be written as:

$$P(R_{data}|\gamma I) = \frac{1}{\sqrt{2\pi}\sigma} e^{-\frac{1}{2}\left(\frac{R_{data}-f(\gamma)}{\sigma}\right)^2} \tag{8.4}$$

where $R_{data} = 0.37$, $\sigma = 0.03$, and $f(\gamma)$ is defined by R_{theory} and is a function of γ. $f(\gamma)$ was determined by linearly interpolating between the R_{theory} values as shown in Table 8.1.

• **Definition of the prior probability:** The prior probability represents all prior knowledge of the distribution of the energy scale for quark compositeness in terms of γ. Since we have no knowledge of this probability other than the fact that γ is physically constrained to be between 0 and ∞, and that values of Λ_c lower than 1.0 TeV have been excluded, we define the prior probability as a 'flat prior', as a constant in the range of γ from 0 to 1.0 and zero elsewhere. This means that, a priori, any value of γ less than 1.0 is equally likely.

• **The normalization:** The normalization Z was determined by integrating

$$Z = \int_0^\infty \frac{1}{\sqrt{2\pi}\sigma} e^{-\frac{1}{2}\left(\frac{R_{data}-f(\gamma)}{\sigma}\right)^2} d\gamma. \tag{8.5}$$

• **Determination of the limit on Λ_c:** The limit on γ at a 95% confidence level was determined as that value for which the following was true:

$$\frac{\int_0^\gamma \frac{1}{\sqrt{2\pi}\sigma} e^{-\frac{1}{2}\left(\frac{R_{data}-f(\gamma)}{\sigma}\right)^2} d\gamma}{Z} = 0.95 \tag{8.6}$$

The limit for γ ($\gamma < 0.31$) was converted to a limit on Λ_c, which, at the 95% confidence level, is $\Lambda_c > 1.8$ TeV.

In order to obtain a more realistic limit on the value of Λ_c, we must take into account the dependence of the next-to-leading-order predictions on the renormalization scale. In order to avoid the complications of folding in the dependence of the limit on the renormalization scale, we chose to treat the theoretical predictions for each renormalization scale as a separate model and to calculate a limit on Λ_c for each. The difference between the two limits will provide an indication of the dependence of the result on the uncertainty in renormalization scale. The identical procedure as used for $\mu = E_T$ was used to calculate a limit on Λ_c for a renormalization scale of $\mu = \frac{E_T}{2}$. The ratios corresponding to the theoretical predictions generated for $\mu = \frac{E_T}{2}$ as a function of Λ_c is shown in Table 8.2

The limit on Λ_c at 95% confidence level for a renormalization scale of $\mu = \frac{E_T}{2}$ is found to be $\Lambda_c > 2.1$ TeV.

Table 8.2: The ratio of $\frac{N(1\leq\chi<6)}{N(6\leq\chi<18)}$ for theoretical predictions of QCD for a renormalization scale of $\frac{E_T}{2}$ with an added term for quark compositeness at various energy scales, Λ_c.

Λ_c (TeV)	R_{theory}
∞	0.423
10	0.424
5.0	0.425
3.0	0.427
2.5	0.436
2.4	0.438
2.3	0.441
2.2	0.441
2.1	0.443
2.0	0.453
1.95	0.454
1.9	0.456
1.85	0.459
1.8	0.465
1.75	0.468
1.7	0.476
1.65	0.483
1.6	0.505
1.55	0.498
1.5	0.528
1.4	0.552
1.0	0.835

Chapter 9

Conclusions

The dijet angular distribution provides a good test of the predictions of QCD because it allows us to measure the properties of parton-parton interactions without reliance on the details of parton distribution functions. We have measured the dijet angular distributions in four mass regions: $260 < M_{JJ} < 425$, $475 < M_{JJ} < 635$, $M_{JJ} > 550$, and $M_{JJ} > 635$ GeV/c^2. We found that the measured distributions are well modeled in all mass regions by the predictions of next-to-leading order QCD. We did not observe any departure from QCD that would indicate a need for an addition of a theory for quark compositeness.

The 1993-1996 collider run of the Tevatron provided the DØ experiment with a large amount of data in mass regions high enough to place a good constraint on the energy scale of quark composite interactions Λ_c. Using Bayesian techniques for finding confidence limits, we placed a limit of $\Lambda_c > 1.8$ TeV at the 95% confidence level.

For the future, the higher luminosities that will be attained in Run 2 of the Tevatron will provide more data in higher mass regions that will have a greater sensitivity to the energy scale of quark compositeness and allow us to place a more restrictive constraint on the minimum value of Λ_c.

Bibliography

[1] F. Abe *et al.*, "Inclusive Jet Cross Section in $p\bar{p}$ Collisions at $\sqrt{s} = 1.8$ TeV", *Physical Review Letters*, **77**, 438-443 (1996).

[2] G. Blazey, "Preliminary Measurement of the Inclusive Jet and Dijet Cross Section in $p\bar{p}$ Collisions at $\sqrt{s} = 1.8$ TeV", *31st Recontres de Moriond: March 1996, Les Arcs, France.* Fermilab Preprint FERMILAB-CONF-96-132-E, June 1996.

[3] V. Barger and R. Phillips, *Collider Physics*, Reading, Mass.: Addison Wesley, 1987, p. 155.

[4] F. Halzen, A. Martin, *Quarks and Leptons: An Introductory Course in Modern Particle Physics*, New York: John Wiley and Sons, 1984.

[5] D. Griffiths, *Introduction to Elementary Particles*, New York: John Wiley and Sons, 1987.

[6] J. Huth, M. Mangano, "QCD Tests in Proton-Antiproton Collisions", *Annual Review of Nuclear Particle Science*, **43**, 585-633 (1993).

[7] R. K. Ellis, W. J. Stirling, "QCD and Collider Physics", Fermilab Preprint FERMILAB-Conf-90/164-T, August 1990.

[8] H. L. Lai *et al.*, "Global QCD Analysis and the CTEQ Parton Distributions", *Physical Review D* **51**, 4763-4782 (1995).

[9] W. T. Giele, E. W. Glover, D. A. Kosower, *Physical Review Letters* **73**, 2019 (1994). The program JETRAD was written by these authors.

[10] B. Abbott *et al.*, "Fixed Cone Jet Definitions in DØ and R_{sep}", DØ Note # 2885, March 21 , 1996 (unpublished).

[11] E. Eichten *et al.*, "Supercollider Physics", *Review of Modern Physics*, **56**, 579-703 (1984).

[12] I. Hinchliffe, "The Papageno Partonic Monte-Carlo Program", LBL-34372, July, 1993.

[13] S. Abachi *et al.*, "The DØ Detector", *Nuclear Instruments and Methods*, **A338**, 185 (1994).

[14] M. Abolins *et al.*, "The Fast Trigger for the DØ Experiment", *Nuclear Instruments and Methods*, **A289**, 543 (1990).

[15] N. Hadley, "Cone Algorithm for Jet Finding", DØ Note # 904, November 29, 1989 (unpublished).

[16] J.E. Huth *et al.*,"Toward a Standardization of Jet Definitions", *Research Directions for the Decade, Proceedings of the 1990 Summer Study on High Energy Physics: Snowmass, Colorado, June 25 - July 13, 1990*, E. Berger, ed.,World Scientific.

[17] A. Aihara *et al.*, *Nuclear Instruments and Methods*, **A325**, 393 (1993).

[18] S. Abachi *et al.*, *Nuclear Instruments and Methods*, **A324**, 53 (1993).

[19] U. Heintz, "A Measurement of the Calorimeter Response Using π^0 Decays", DØ Note # 2268, August, 1994 (unpublished).

[20] I. Adam *et al.*, "Observation of J/ψ to ee decays at DØ and Calibration of the Central Calorimeter Electromagnetic Energy Scale", DØ Note # 2298, October, 1994 (unpublished).

[21] R. Kehoe, R. Astur, "Determination of the Hadronic Energy Scale of DØ Calorimetry", DØ Note # 2908, May 7, 1996 (unpublished).

[22] M. Bhattacharjee *et al.*, "Jet Energy Resolutions", DØ Note # 2887, May 22, 1996 (unpublished).

[23] D. Elvira, "Jet η Bias and Resolution", DØ Note # 2173, June 8, 1994 (unpublished).

[24] C. Kim, T. Heuring, S.Y. Jun, "Position Biases and Resolutions in Jet Measurements", DØ Note # 2477, February 15, 1995 (unpublished).

[25] D. Elvira *et al.*, "A Study of Standard Jet Cuts and their Efficiencies Using D0 Collider Data", DØ Note # 1763, July 21, 1993 (unpublished).

[26] M. Bhattacharjee, "Efficiencies of the Standard Jet Cuts for Cone Sizes:0.3,0.5,0.7", DØ Note # 2197, July 15, 1994 (unpublished).

[27] I. Bertram *et al.*, "A Recipe for the Construction of Confidence Limits", DØ Note # 2775A, December 18, 1995 (unpublished).